

**CZECH TECHNICAL UNIVERSITY IN
PRAGUE**

**FACULTY OF NUCLEAR SCIENCES
AND PHYSICAL ENGINEERING**

Department of Physics
Experimental Nuclear and Particle Physics



BACHELOR THESIS

**Collectivity of nuclear matter at
FAIR collider**

Vypracoval: Ondřej Hofman
Vedoucí práce: RNDr. Petr Chaloupka, Ph.D.
Rok: 2023

**ČESKÉ VYSOKÉ UČENÍ TECHNICKÉ
V PRAZE**

**FAKULTA JADERNÁ A FYZIKÁLNĚ
INŽENÝRSKÁ**

Katedra fyziky
Experimentální jaderná a částicová fyzika



BAKALÁŘSKÁ PRÁCE

**Kolektivní chování jaderné hmoty
na urychlovači FAIR**

Vypracoval: Ondřej Hofman
Vedoucí práce: RNDr. Petr Chaloupka, Ph.D.
Rok: 2023



Katedra: fyziky

Akademický rok: 2021/2022

ZADÁNÍ BAKALÁŘSKÉ PRÁCE

Student: Ondřej Hofman

Studijní program: Aplikace přírodních věd

Obor: Experimentální jaderná a částicová fyzika

Název práce: Kolektivní chování jaderné hmoty na urychlovači FAIR
(česky)

Název práce: Collectivity of nuclear matter at FAIR collider
(anglicky)

Pokyny pro vypracování:

- 1) Student se seznámí s ultra-relativistickými srážkami těžkých jader.
- 2) Student se seznámí s experimentem CBM na urychlovači FAIR.
- 3) Bude provedena rešerše současných výsledků týkajících se toku částic ve srážkách těžkých jader. Pozornost bude věnována zejména toku částic obsahujících podivný kvark.
- 4) Bude provedena rešerše teoretických modelů a předpovědí relevantních pro energie srážek na urychlovači FAIR
- 5) Student se blíže seznámí s detektorem Projectile Spectator Detector (PSD), který se bude používat pro měření roviny srážky na experimentu CBM.

Doporučená literatura:

- [1] T. Ablyazimov, et al.: Challenges in QCD matter physics - The scientific programme of the Compressed Baryonic Matter experiment at FAIR, Eur. Phys. J. A. 53 (2017) 60
- [2] B. Friman, et al.: The CBM Physics Book, ISBN: 978-3-642-13293-3
- [3] N. Herrmann, J. P. Wessels and T. Wienold: Collective flow in heavy ion collisions, Ann. Rev. Nucl. Part. Sci. 49 (1999) 581 (1999)
- [4] R. Stock: Relativistic Heavy Ion Physics, Springer, 2010

Jméno a pracoviště vedoucího bakalářské práce:

RNDr. Petr Chaloupka, Ph.D.

Katedra fyziky, Fakulta jaderná a fyzikálně inženýrská, ČVUT v Praze

Jméno a pracoviště konzultanta:

Mgr. Lukáš Chlad, Ph.D.


Katedra fyziky, Fakulta jaderná a fyzikálně inženýrská, ČVUT v Praze


Datum zadání bakalářské práce: 20.10.2021

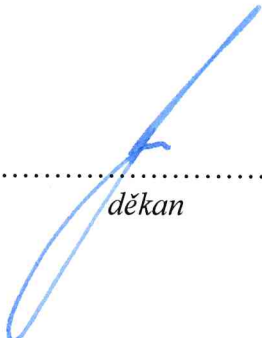
Termín odevzdání bakalářské práce: 07.07.2022

Doba platnosti zadání je dva roky od data zadání.


.....
garant oboru


.....
vedoucí katedry




.....
děkan

V Praze dne 20.10.2021



PROHLÁŠENÍ

Já, níže podepsaný

Jméno a příjmení studenta: Ondřej Hofman

Osobní číslo: 486353

Název studijního programu (oboru): Aplikace přírodních věd

prohlašuji, že jsem bakalářskou práci s názvem:

Kolektivní chování jaderné hmoty na urychlovači FAIR

vypracoval samostatně a uvedl veškeré použité informační zdroje v souladu s Metodickým pokynem o dodržování etických principů při přípravě vysokoškolských závěrečných prací.

V Praze dne 5.1.2023

.....
Hofman

podpis

Acknowledgments

I would like to thank my supervisor RNDr. Petr Chaloupka, Ph.D. for his help and guidance and my family and friends for their patience and support.

Ondřej Hofman

Název práce:

Kolektivní chování jaderné hmoty na urychlovači FAIR

Autor: Ondřej Hofman

Studijní program: Aplikace přírodních věd

Obor: Experimentální jaderná a částicová fyzika

Druh práce: Bakalářská práce

Vedoucí práce: RNDr. Petr Chaloupka, Ph.D.

Katedra fyziky, Fakulta jaderná a fyzikálně inženýrská, ČVUT v Praze

Konzultant: Mgr. Lukáš Chlad, Ph.D.

Katedra fyziky, Fakulta jaderná fyzikálně inženýrská, ČVUT v Praze

Abstrakt: Studium kolektivního chování jaderné hmoty je jedno ze zásadních studií částicové fyziky. Může poskytnout informace nejen o evoluci horké a husté hmoty, která vzniká při vysokoenergetických srážkách, ale i o produkci částic nebo o chování zmíněné hmoty. Pomocí anizotropního toku lze studovat různé vlastnosti hmoty, což může osvětlit mechanismy produkce částic nebo hydrodynamické chování jaderné hmoty. Tato měření budou provedena na experimentu CBM, který je součástí urychlovače FAIR, s vysoce intenzivními interakcemi. Klíčový detektor pro tyto studie je Projectile Spectator Detector (nebo jeho náhrada), který využívá specifické struktury, aby byly splněny požadavky experimentu. Tato práce poskytuje studii modelování specifické beam pipe uvnitř PSD společně s výhledem a plány budoucí práce na nástupci PSD.

Klíčová slova: CBM, PSD, kolektivita, anizotropní tok

Title:

Collectivity of nuclear matter at FAIR collider

Author: Ondřej Hofman

Study program: Applied Natural Sciences

Specialization: Experimental Nuclear and Particle Physics

Sort of project: Bachelor thesis

Supervisor: RNDr. Petr Chaloupka, Ph.D.

Department of Physics, Faculty of Nuclear Sciences and Physical Engineering, Czech Technical University in Prague

Consultant: Mgr. Lukáš Chlad, Ph.D.

Department of Physics, Faculty of Nuclear Sciences and Physical Engineering, Czech Technical University in Prague

Abstract:

The study of collectivity of nuclear matter is one of the crucial studies in particle physics. It can provide information not only about the evolution of hot and dense matter created after highly energetic collisions, but also about the production of particles or the behaviour of said matter. Using the anisotropic flow to study various properties of matter may shine a light upon particle production mechanisms or the hydrodynamical behaviour of nuclear matter. These measurements are to be done by the CBM experiment at FAIR with highly intensive interactions. A key detector for these studies is the Projectile Spectator Detector (or its replacement) with a specific structure in order to fulfil all requirements of the experiment. This thesis provides a study on modelling a specific beam pipe inside the PSD together with an outlook and plans for future work on the PSD replacement.

Key words: CBM, PSD, collectivity, anisotropic flow

Contents

List of Tables	xiii
List of Figures	xiii
1 Introduction to Particle Physics	1
1.1 Standard Model	1
1.1.1 Elementary Particles	1
1.1.2 Fundamental Interactions	3
1.2 Quantum Chromodynamics	3
1.3 Nuclear Matter Under Extreme Conditions	5
2 Heavy Ion Collisions	9
2.1 Collision Geometry	9
2.2 Evolution of the Collision	10
2.3 Kinematic Variables	11
2.4 Particle Production	12
2.5 Nuclear Modification Factor	16
2.6 Dilepton Production	19
2.7 Strangeness Enhancement	20
3 Collectivity in Heavy Ion Collisions	23
3.1 Radial Flow	23
3.2 Anisotropic Flow	25
3.2.1 Elliptic flow	26
3.2.2 Higher-order Flow Coefficients	33
3.2.3 Flow in Small Systems	35
3.2.4 Non-flow Effects	38
3.2.5 Experimental Methods	38
4 CBM Experiment at FAIR	43
4.1 The Facility for Antiproton and Ion Research	43
4.2 The APPA Experiment	45
4.3 The CBM Experiment	45
4.4 Projectile Spectator Detector	48
4.4.1 PSD Structure and Geometry	49
4.4.2 Centrality Determination	50
4.4.3 Reaction Plane Reconstruction	51
4.5 Effects of PSD Beamhole	54
4.6 Current situation	55
4.7 New Forward Detector for CBM	56
5 CBM Beam Pipe Simulations	59
5.1 Bellow Modeling	60

List of Tables

1.1	Basic characteristics of fundamental interactions, relative strength is given with respect to the strong interaction.	3
-----	---	---

List of Figures

1.1	Elementary particles of the standard model [1].	2
1.2	Running of the QCD and QED coupling constants [5].	4
1.3	Formation of quark-gluon plasma [8].	5
1.4	The QCD potential at zero (solid line) and non-zero temperatures [9].	6
1.5	The phase diagram of nuclear matter [11].	7
2.1	Classification of collisions into central, peripheral and ultra-peripheral [12].	9
2.2	Participants and spectators in a nucleus-nucleus collision [13].	10
2.3	Space-time evolution of a collision with and without reaching of QGP phase [15].	11
2.4	Left: Particle yield ratios from RHIC fitted with statistical model calculations [20] Right: Phenomenological phase diagram of strongly interacting matter constructed from chemical freeze-out points for central collisions at different energies [19].	14
2.5	The evolution of kinetic transport models [24].	16
2.6	The p_T distributions of primary charged particles at mid-rapidity ($ \eta < 0.8$) in central (0 - 5%) and peripheral (70 - 80%) Pb+Pb collisions at $\sqrt{s_{NN}} = 2.76$ TeV. The scaled pp references are shown as the two curves, the upper for 0 - 5% centrality and the lower for 70 - 80% [25].	17
2.7	R_{AA} in central (0 - 5%) and peripheral (70 - 80%) Pb-Pb collisions at $\sqrt{s_{NN}} = 2.76$ TeV. The results indicate strong suppression in central collisions for $p_T > 6.5$ GeV/c. [25].	18
2.8	Left: Comparison of R_{AA} in central Pb+Pb collisions at LHC to measurements at $\sqrt{s_{NN}} = 200$ GeV by the PHENIX and STAR experiments at RHIC [25]. Right: R_{AA} in p+Pb and Pb+Pb collision at LHC for hadrons as well as photons and W^\pm and Z bosons [26].	18

2.9	(a) e^+e^- invariant mass spectrum from $s_{NN} = 200$ GeV Au+Au minimum bias (0 - 80%) collisions compared to a hadronic cocktail simulation. (b) Ratios to cocktail for data and model calculations [27].	20
2.10	(a,b) Enhancements in the rapidity range $ y < 0.5$ as a function of the mean number of participants $\langle N_{part} \rangle$, showing LHC (ALICE, full symbols), RHIC and SPS (open symbols) data. (c) Hyperon-to-pion ratios as a function of $\langle N_{part} \rangle$, for A-A and pp collisions at LHC and RHIC energies. The lines mark the thermal model predictions. Figure from [29].	21
3.1	Invariant yields in Pb+Pb and p+p collisions of π^\pm, K^\pm, p [30].	24
3.2	The extracted kinetic freeze-out temperature T_{kin} versus the average radial flow velocity $\langle \beta_T \rangle$ from a simultaneous Blast-wave fit to the K_S^0 and Λ p_T spectra for p+p, p+Pb and Pb+Pb collisions [32].	24
3.3	Time evolution of the spatial eccentricity ε_x and the momentum anisotropy ε_p for Au+Au collisions at RHIC with $b = 7$ fm [33].	25
3.4	Left: The definitions of the Reaction Plane and the Participant Plane coordinate systems. Right: Diagrams of elliptic and directed flow [34].	26
3.5	A visualization of directed and elliptic flow and higher harmonic coefficients [35].	27
3.6	A comparison of ideal hydrodynamics calculations with first v_2 measurements [38].	27
3.7	The collision energy dependence of elliptic flow in the 20%-30% centrality class [39].	28
3.8	The collision centrality dependence of elliptic flow [39].	29
3.9	Elliptic flow v_2 divided by the spatial anisotropy of the participant zone ϵ as a function of charged particle density [40].	29
3.10	The p_T dependence of elliptic flow of protons and pions with hydrodynamic calculations for a hadron gas [34].	30
3.11	v_2 for $\sqrt{s_{NN}} = 200$ GeV Au+Au as a function of p_T [34].	31
3.12	The $(m_T - m_0)/n_q$ dependence of v_2/n_q for $\pi^\pm, K, p+\bar{p}, \phi, \Lambda+\bar{\Lambda},$ and $\Xi^-+\bar{\Xi}^+$ for Pb+Pb collisions for 30-40% centrality class at $\sqrt{s_{NN}} = 2.76$ TeV [39].	32
3.13	v_2 scaled by the number of constituent quarks as a function of scaled transverse kinetic energy $(m_T - m_0)/n_q$ for pions, kaons and protons from Au+Au collisions in 10-40% centrality at $\sqrt{s_{NN}} = 3, 27,$ and 54.4 GeV for positively charged particles (left panel) and negatively charged particles (right panel) [42].	32
3.14	Average prompt $D^0, D^+,$ and $D^*+ v_2$ in Pb-Pb collision at $\sqrt{s_{NN}} = 5.02$ TeV in the 30%-50% centrality class, compared to that of charged pions for $p_t < 15$ GeV/c, charged particles $p_t > 15$ GeV/c at mid-rapidity, and inclusive J/ψ mesons at forward rapidity [43].	33
3.15	Higher-order flow coefficients centrality dependence [44].	34
3.16	Higher-order flow coefficients p_T dependence in ultra central collisions [45].	35
3.17	Multiplicity dependence of v_2, v_3 and v_4 measured using the two-particle cumulant method with a $ \eta $ gap in small and large collision systems [58].	36

3.18	Flow coefficient measurements in smaller systems with hydrodynamic predictions [46].	37
3.19	The difference in the elliptic flow with non-flow effects (red) and without non-flow effects (magenta) [59].	38
3.20	The event plane resolution as a function of χ . The harmonic number of the correlation n is an integer k times the harmonic number m of the event plane [34].	40
3.21	Pseudorapidity dependence of elliptic flow for $\sqrt{s_{NN}} = 200$ GeV Au+Au from the event plane method (STAR), the LYZ method (STAR), and using an η gap (PHOBOS) [63].	41
4.1	The Facility for Antiproton and Ion Research [65].	43
4.2	The CBM detector layout with (left) the particle identification detector RICH, and (right) the muon identification detector MUCH [70].	46
4.3	The structure of the PSD and its segmentation into three concentric sections. [70].	49
4.4	Design of the PSD module and light readout from scintillator tiles in PSD module. Left-front view, right- top view (only half-length of the module is shown). Fibers from each consecutive 6 tiles are collected together and read out by a single MAPD [70].	50
4.5	CBM detector geometry used for the PSD performance study [70].	50
4.6	Left: The correlation between the energy deposited in the central PSD modules (E_{PSD}^1) and the track multiplicity M_{trk} . Right: The correlation between the energy deposited in the central modules of the PSD (PSD1) and track multiplicity with a cut $M_{\text{trk}}/M_{\text{trk}}^{\text{max}} > 0.6 - 0.8E_{\text{PSD}}/E_{\text{PSD}}^{1,\text{max}}$ [77].	51
4.7	Event averaged x component of the Q-vector, $\langle Q_x \rangle$, for different PSD subevents versus the energy of the corresponding PSD subevents before (solid symbols) and after (open symbols) the Q-vector recentering procedure is applied. The panels (from left to right) show results using (a) full PSD information, (b) PSD1, (c) PSD2, and (d) PSD3 subevents. Different colors show results for $E_b = 2, 10, \text{ and } 35$ AGeV [70].	52
4.8	First order reaction plane resolution, $\sigma(\Psi_{1,\text{EP}} - \Psi_{\text{RP}})$, for semi-central (20 - 50%) Au+Au collisions. Left: Results for $E_b = 2, 4, 6, 10, 15, 25, \text{ and } 35$ AGeV as a function of the PSD distance from the target in the range between 8 and 15 m. Right: Effect of the magnetic field on the event plane resolution at the $E_b = 2$ AGeV. The PSD is located 8 m from the target [70].	53
4.9	First order reaction plane resolution (left), $\sigma(\Psi_{1,\text{EP}} - \Psi_{\text{RP}})$, and (right) resolution correction factor, $R_{1,\text{EP}} = \langle \cos(\Psi_{1,\text{EP}} - \Psi_{\text{RP}}) \rangle$, plotted as a function of the centrality estimated with the STS detector for Au+Au collisions at $E_b=2, 4, 6, 10, 15, 25, \text{ and } 35$ AGeV [70].	54
4.10	Proton v_2 versus p_T reconstructed with the PSD event plane for one million Au+Au collisions generated with the UrQMD model [70].	54
4.11	Relative statistical errors for v_2 of Ω^- (Λ and proton) in mid-central Au+Au collisions ($b = 6 - 8$ fm) projected for 10^{11} (10^{10}) minimum bias Au+Au collisions [70].	55

4.12	The layout of the PSD modules in the plane transverse to the beam direction with the diamond-shaped hole [78].	55
4.13	Resolution correction factors for PSD with larger central beam hole for subevents calculated with (a) 3-subevent and (b) mixed-harmonic methods. The lines show the true values obtained using the reaction plane angle from the event generator [78].	56
4.14	Event plane resolution as a function of collision centrality from Au+Au collisions at $\sqrt{s_{NN}} = 3$ (a), 27 and 54.4 GeV (b). In the case of the 3 GeV collisions, Ψ_1 is used to determine the event plane resolutions for the first and second harmonic coefficients shown as R_{11} and R_{12} in the left panel. In the 27 and 54.4 GeV collisions, Ψ_2 is used to evaluate the second-order event plane resolution, see right panel [79].	57
5.1	Deflection of Au beams with kinetic energies between 2 and 8 AGeV by the magnetic field with an integral of 1 Tm [81].	60
5.2	CBM beam pipe model made with Autodesk Inventor.	60
5.3	Tilting joint assembly model made with Autodesk Inventor.	61
5.4	Left: Top view of the bellow with model parameters. Right: A 2D sketch of the bellow with the segmentation into five sections.	61
5.5	The middle segment's length values for different driving angles fitted with a fifth-degree polynomial.	62
5.6	The CBM beam pipe model made with ROOT.	62
5.7	Tilting joint assembly model made with ROOT.	63
5.8	Top view of the bellow for 0 degrees (left), 0.7 degrees (center), and 1.5 degrees (right).	63
5.9	Top view of the ROOT bellow model for 0 degrees (left), 0.7 degrees (center), and 1.5 degrees (right).	63
5.10	The secondary particle generation simulations.	63

Chapter 1

Introduction to Particle Physics

1.1 Standard Model

The Standard Model is the most comprehensive theory of particle physics currently known. It classifies all known elementary particles and describes three of the four fundamental interactions (strong, weak and electromagnetic).

It is a mathematically self-consistent theoretical framework based on quantum field theory and fundamental symmetries that is able to describe a wide range of physics phenomena. Since its conception, the Standard Model has been extensively experimentally tested for more than half a century. Despite its excellent success, it is known that it is not a complete theory as it does not include other phenomena such as gravity and the explanation of dark matter.

In this section, a brief description of the basic constituents of the Standard Model is given and phenomena which are important for this thesis are discussed.

1.1.1 Elementary Particles

According to the Standard Model, elementary particles are particles considered to have no substructure. They can be divided into two groups based on their spin. Fermions, which have half-integer spin, and bosons, which have integer spin.

Quarks and Leptons

Quarks and leptons are both types of fermions meaning that they obey the Pauli exclusion principle and are governed by the Fermi-Dirac statistics. They can be classified according to how they interact with matter. Quarks carry a color charge, therefore, they are the only fermions interacting via strong interaction, leptons on the other hand carry an electric charge and thus interact via electromagnetic interaction. Furthermore, quarks also carry an electric charge but unlike any other particles, the values are only fractions of the elementary electron charge ($\frac{2}{3}$ or $-\frac{1}{3}$). Another way of dividing these fermions would be into doublets which then form three generations, each with a quark doublet and a lepton doublet. The first generation

Standard Model of Elementary Particles

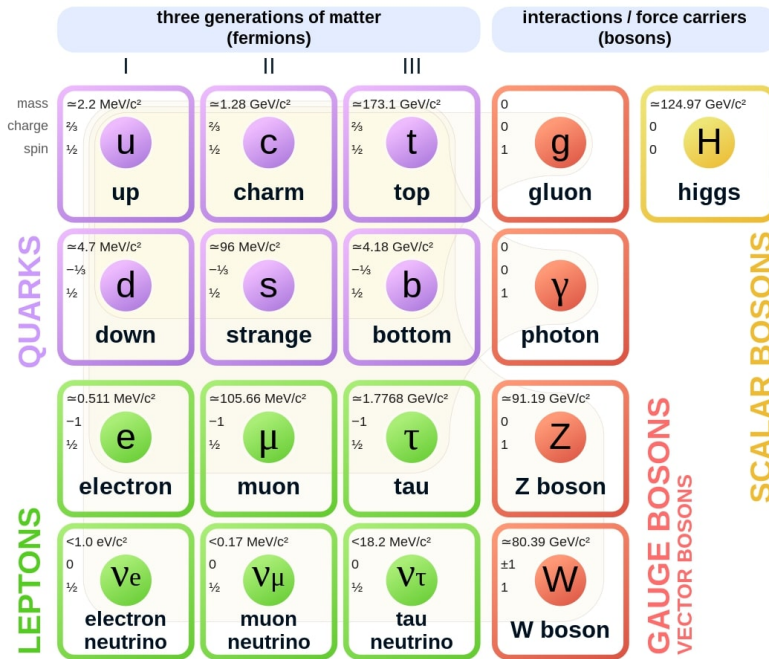


Figure 1.1: Elementary particles of the standard model [1].

consists of the up quark (u) and the down quark (d), the electron (e) and the electron neutrino (ν_e). The second generation is formed by the charm quark (c), the strange quark (s), the muon (μ) and the muon neutrino (ν_μ), and the third by the top quark (t), the bottom quark (b), the tau lepton (τ) and the tau neutrino (ν_τ). A confined state of quarks is called a hadron. Hadrons are always color-neutral and consist of either two quarks (mesons) or three quarks (baryons).

Gauge Bosons

In the Standard Model, gauge bosons are particles that mediate the interactions between particles. As bosons, they have integer spin, therefore they do not obey the Pauli exclusion principle and are described by the Bose-Einstein statistics. Gauge bosons are classified into three groups:

- photons (γ) mediate the electromagnetic interaction,
- gluons (g) mediate the strong interaction between quarks. They also carry a color charge so they can, unlike photons, interact between themselves,
- W^+ , W^- and Z^0 bosons mediate the weak interaction.

Apart from gauge bosons, another boson has been discovered, called the Higgs boson. Gluons and photons are massless while the W^\pm and Z^0 bosons have mass in the order of $100 \text{ GeV}/c$ [2]. The discovery of W^\pm and Z^0 bosons [3] as well as Higgs boson [4] were milestone achievements in the evolution of particle physics.

1.1.2 Fundamental Interactions

The standard model describes three of the four fundamental forces of nature, the strong interaction, the weak interaction and the electromagnetic interaction. These interactions are described as an exchange of a gauge boson between the affected particles.

Interaction	Mediator	Relative strength	Range [m]
Strong	Gluon	1	10^{-15}
Weak	W and Z bosons	10^{-6}	10^{-18}
Electromagnetic	Photon	10^{-2}	∞

Table 1.1: Basic characteristics of fundamental interactions, relative strength is given with respect to the strong interaction.

Strong interaction

The strong interaction binds together quarks to form a hadron but is also responsible for binding baryons, such as protons or neutrons, into atomic nuclei. It is mediated by massless gluons which carry a color-anticolor charge. The theory describing the strong interaction, called Quantum Chromodynamics (QCD), is further discussed in the following section.

Weak interaction

The weak interaction is responsible for a variety of particle decays, such as beta decay. It is mediated by the W^\pm and Z^0 bosons. Its characteristic short range and relative weakness is due to the large masses of mediators. W^\pm bosons have an electric charge and mediate interactions that change the particle type (or flavor) and charge. Also, the weak interaction is the only one in which neutrinos participate.

Electromagnetic interaction

The electromagnetic force is mediated by massless photons. It is the only long-range interaction within the Standard Model. On macroscopic scale, classical electrodynamics can describe such phenomena as electromagnetic waves. On a microscopic scale, the quantum nature of the interaction must be taken into account which is explained by Quantum Electrodynamics (QED). It affects all electrically charged particles. This results in a wide range of phenomena including atomic electron shell structure or chemical bonds.

1.2 Quantum Chromodynamics

Quantum Chromodynamics (QCD) is a theory describing the strong interaction which, similarly to the electromagnetic interaction, is mediated by a massless boson

and affects only particles with a certain charge. However, in QCD, the charge is referred to as color and appears in three forms - red, green and blue (and their corresponding anticolor). Each quark carries a color charge, while gluons always carry a color-anticolor charge and therefore they can exist in eight possible states. This also means that gluons can interact with each other unlike photons which do not carry any charge and thus cannot interact with each other. This fact has a significant impact on the coupling constants of strong and electromagnetic interaction, which determine their relative strength, respectively. Figure 1.2 offers a comparison of said coupling constants' dependence on transferred momentum, and consequently on the distance of the interacting particles. It shows that whereas the strength of the electromagnetic force rises with decreasing distance, the strength of the strong interaction decreases for short distances. This is an important property of the QCD which is called **asymptotic freedom**. It means that at short distance (at high transferred momenta) the quarks behave as almost free particles.

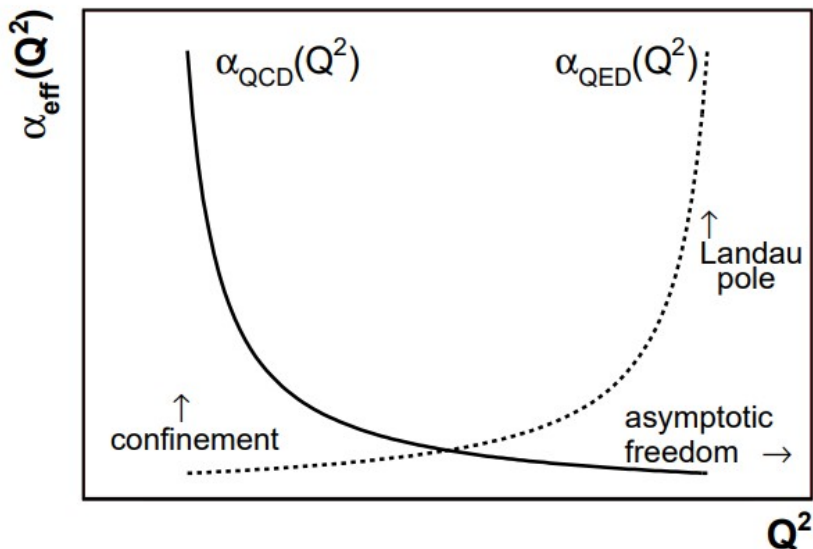


Figure 1.2: Running of the QCD and QED coupling constants [5].

Another crucial consequence of how QCD describes strong interaction is the so-called **color confinement**. This means that bare color-charged particles cannot be isolated and always must form a bound state with no overall color charge. To imagine such phenomena it is instructive to look at an effective potential V , known as the Cornell potential [6], between a quark and an antiquark in a bound state as a function of their distance r . It can be expressed as follows:

$$V(r) = -\frac{a}{r} + kr, \quad (1.1)$$

where a and k are constant parameters. With increasing distance r , the first (Coulombic) term vanishes but the second (elastic) term increases. Consequently, the connection between the quark and the antiquark can be described as an elastic string. When the quark-antiquark pair is being separated, the magnitude of its potential energy grows. When it eventually exceeds the mass of two quarks, another quark-antiquark pair is created from the vacuum. This again assures that one cannot observe free quarks but only bound states with no color charge.

1.3 Nuclear Matter Under Extreme Conditions

Under "normal" conditions (low temperature and density), quarks are bound in hadrons (baryons and mesons) and some of the baryons (mainly protons and neutrons) can bind into nuclei forming the matter as we know it from daily experience. However in the Universe, there were (and still possibly are) times and places where nuclear matter is subjected to extraordinarily extreme conditions, high temperatures and pressures. These can include cores of massive neutron stars or collisions of large stellar objects where we can expect the matter to be extremely heated and compressed. Even more extreme conditions are speculated to have existed at the beginning of the Universe shortly after the Big Bang. Studying nuclear matter under extreme conditions is one of the goals of modern nuclear physics.

Shortly after the discovery of the asymptotic freedom, it was predicted that at high enough density and/or temperature nuclear matter may, as a consequence of the QCD asymptotic freedom, undergo a transition into a deconfined phase [7] (as illustrated in Figure 1.3). In this phase, the quarks and gluons are also no longer confined inside of hadrons, but can propagate throughout the whole medium. Even though the whole medium has overall zero color charge, the quarks behave as single free particles carrying the color charge. This new state of matter is analogous to the plasma phase of ordinary atomic matter and was therefore named the **quark gluon plasma** (QGP). Moreover similarly to regular matter, for nuclear matter, there are also predictions of existence of numerous phase states which were not confirmed so far.

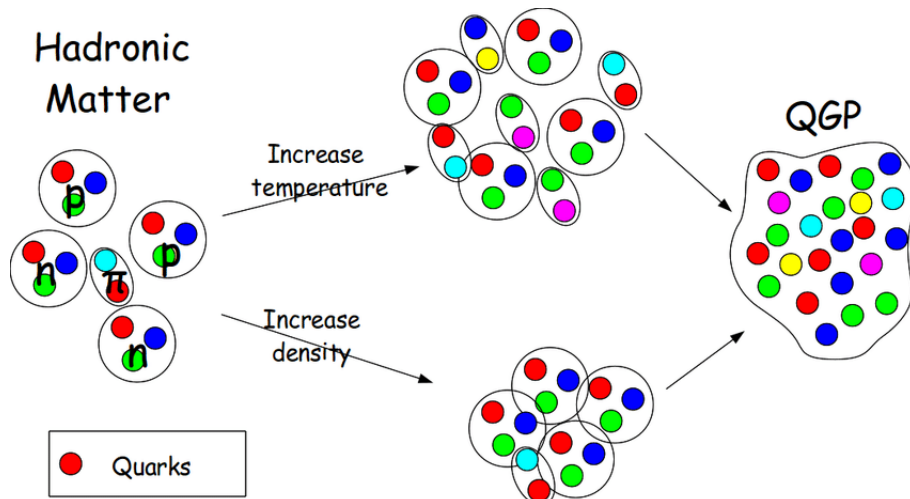


Figure 1.3: Formation of quark-gluon plasma [8].

The effect of the high temperature on the QCD confining potential can be demonstrated by QCD lattice calculations such as [9]. The Cornell potential (1.1) is a valid approximation for the strong force in a vacuum or at zero temperature. Figure 1.4 shows the Cornell potential (solid line) and the potential between heavy quarks at various non-zero temperatures obtained from lattice QCD calculations. Based on this figure, one can assess that at high temperatures the Cornell potential, which normally exceeds every limit, is effectively limited and therefore the quarks, if given enough energy, can effectively behave as free particles.

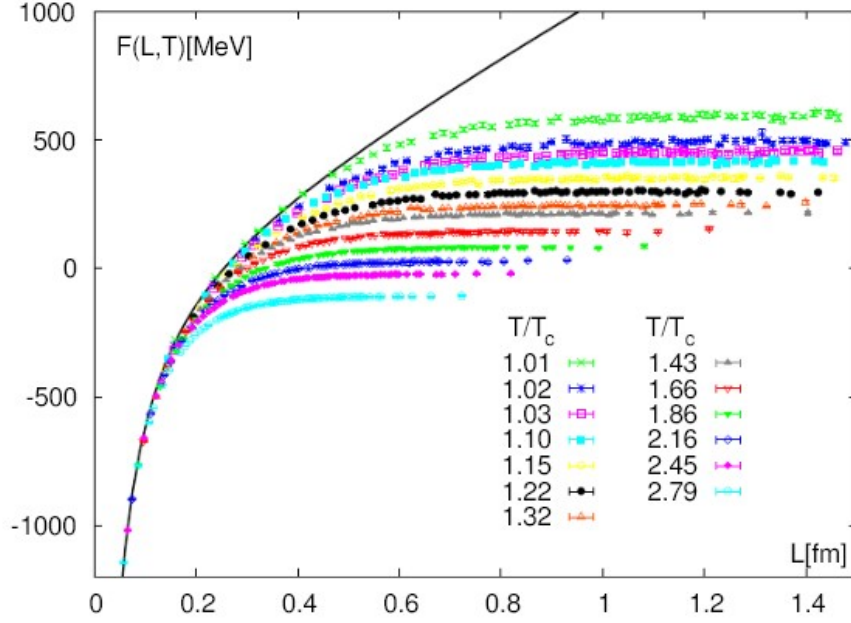


Figure 1.4: The QCD potential at zero (solid line) and non-zero temperatures [9].

Figure 1.5 shows the phase diagram of strongly interacting nuclear matter in terms of temperature T and baryon chemical potential μ_B which corresponds to baryon density. The solid curve represents the first-order phase transition from hadronic matter into QGP, which can thus be reached either by increasing the temperature or by increasing the baryon chemical potential. A particular point on this curve, called the critical point, has been of great interest to current research as it separates the first-order transition region and the so-called crossover region where the second-order transition occurs. It is the scan of QGP with T and μ_B that could provide crucial new information [10]. The figure also shows which regions of the phase diagram are of interest to different research facilities. The high-temperature, low-density region has been the focus of LHC and RHIC whereas future FAIR research will focus on exploring the phase diagram at higher baryon densities.

The QGP state at high baryon chemical potential and low temperatures is expected to exist in neutron stars. Meanwhile, the QGP state at high temperatures and low baryon chemical potential is predicted to have existed a few milliseconds after the Big Bang, before expanding and transitioning into hadrons through a process called hadronization.

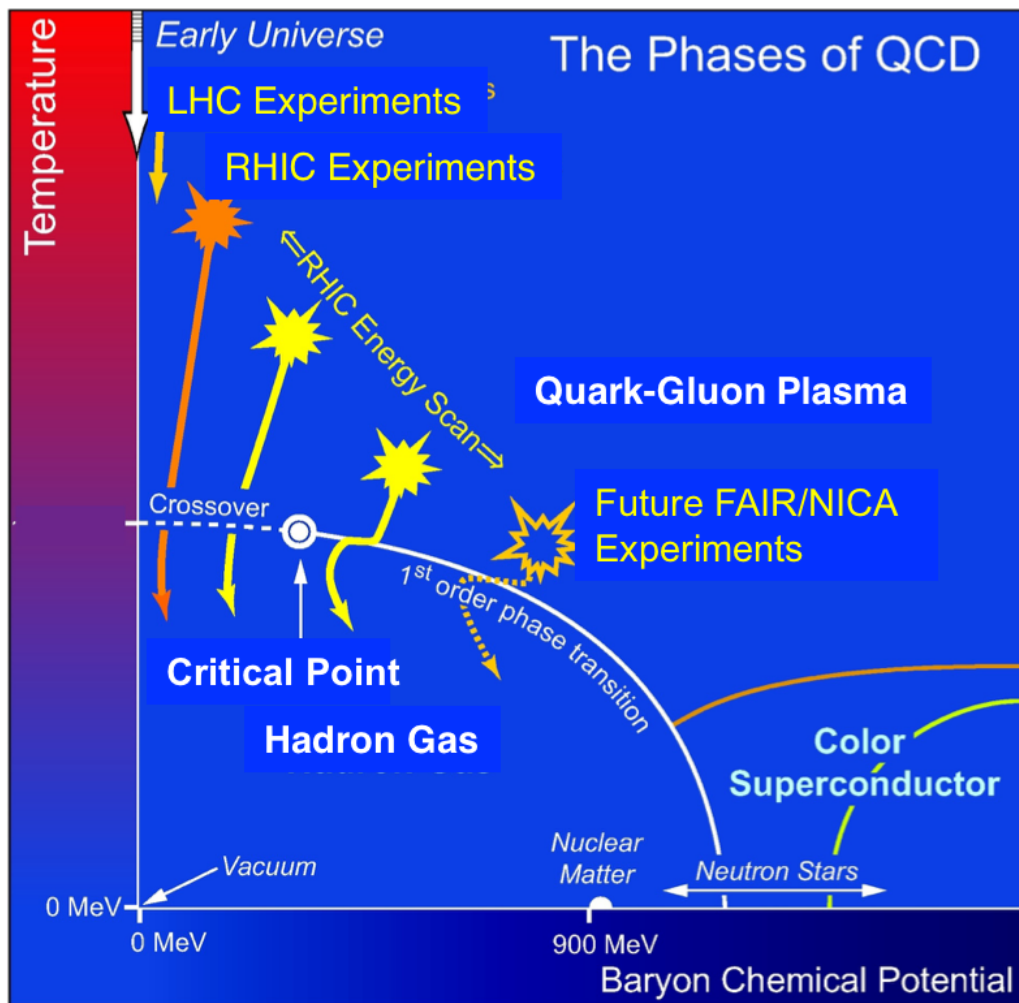


Figure 1.5: The phase diagram of nuclear matter [11].

Chapter 2

Heavy Ion Collisions

As it is impossible for nuclear matter in such extreme states mentioned before to form naturally on earth, the best way to examine them is by performing heavy ion experiments. This chapter focuses on introducing the properties of heavy ion collisions and the most common methods used for studying them.

2.1 Collision Geometry

In high-energy particle physics, collisions can be classified according to the size of the overlap region of the colliding nuclei. In order to achieve this, the impact parameter b is used. It is defined as the perpendicular distance of the centers of the nuclei. Figure 2.1 shows how collisions can be divided into central ($b \approx 0$), peripheral ($0 < b < 2R$) and ultra-peripheral ($b > 2R$). Along with centrality, the multiplicity is directly related to the impact parameter of the collision and it provides information about the number of created particles.

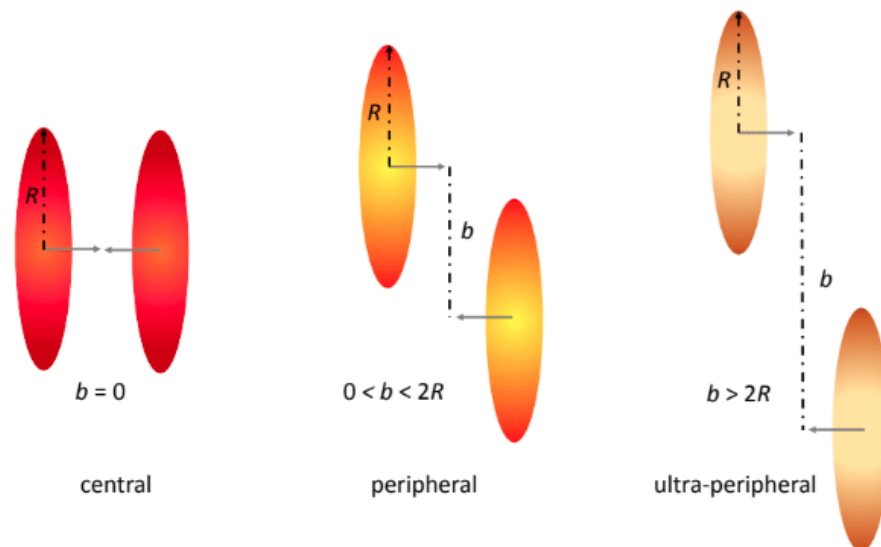


Figure 2.1: Classification of collisions into central, peripheral and ultra-peripheral [12].

This classification implies that not all of the nucleons participate directly in the collision. Nucleons located in the overlap region are called participants. The non-interacting nucleons are called spectators. Participants and spectators are illustrated in Figure 2.2.

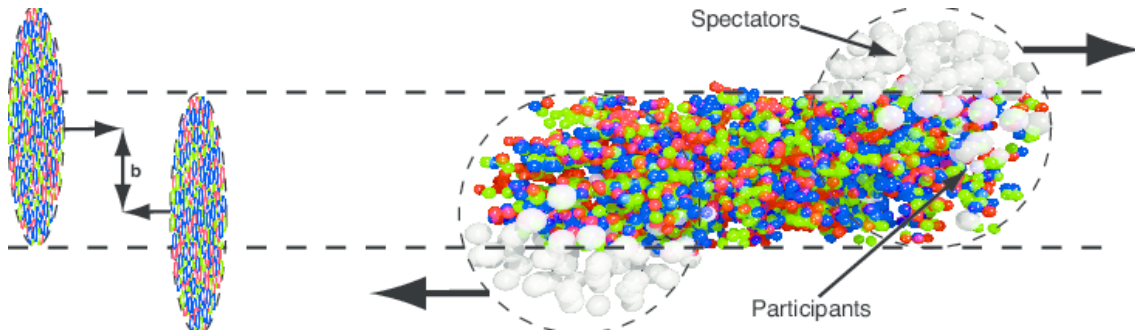


Figure 2.2: Participants and spectators in a nucleus-nucleus collision [13].

2.2 Evolution of the Collision

Although nucleus-nucleus collisions have been the focus of research for many years, it is still not exactly known how the collision occurs and how the system evolves after the collision. This section briefly describes the possible scenario of the evolution of heavy-ion collision.

Figure 2.3 illustrates the space-time evolution of the collision with and without reaching the QGP phase. The point $(z, t) = (0, 0)$ represents the space-time position of the collision. Then the system undergoes several stages that are divided with respect to the proper time $\tau = \sqrt{t^2 - z^2}$ [14].

At the moment of the collision, the system enters the pre-equilibrium phase where the nucleons located in the overlap region form the so-called fireball. Assuming that the energy density is high enough, deconfined partons (quarks and gluons) are produced in inelastic collisions and interact with one another.

At τ_0 thermal equilibrium is reached and, if the conditions are suitable, QGP is expected to exist at this stage. Due to the high energy and pressure inside the fireball, the system starts to expand rapidly. As a consequence of this expansion, the system cools down until the critical temperature T_c is reached at τ_c .

At this point, the QGP undergoes a phase transition into the hadronic matter of bound states. This phase transition can be either of first order or smooth crossover depending on the conditions (place in the phase diagram). During the subsequent stage of the hadronic gas the system continues to evolve and new particles are created in high energy collisions of hadrons. Once the temperature decreases to the point (T_{ch}, τ_{ch}) when inelastic collisions among hadrons cease, the particle abundance ratios are fixed. This point is called chemical freeze-out. The expansion and cool-down continue further and hadrons interact elastically with each other until the distance between hadrons exceeds the range of the strong interaction. At τ_{fo} elastic scattering is no longer possible, kinetic freeze-out occurs and the products of the collision move away from the collision region.

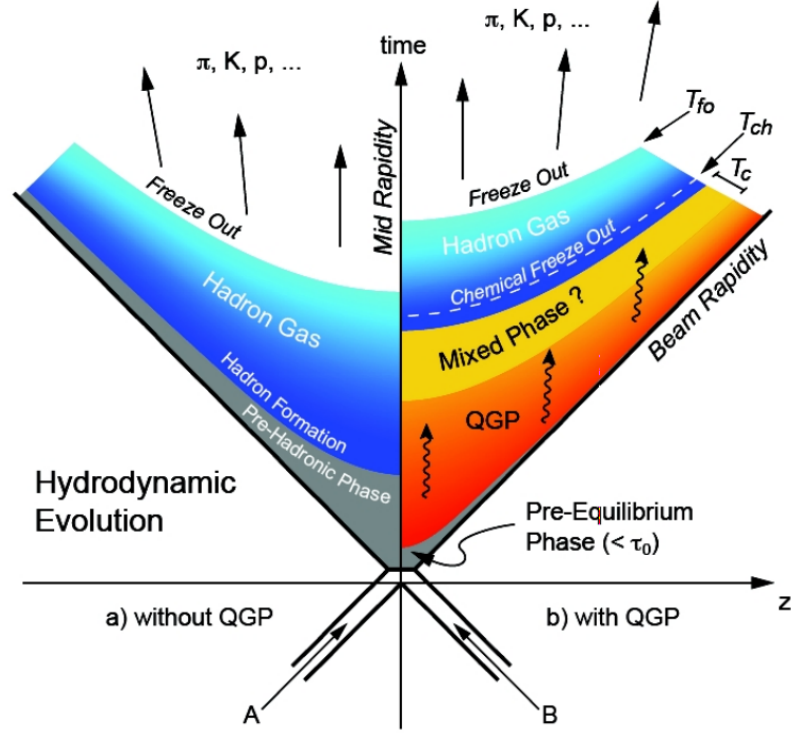


Figure 2.3: Space-time evolution of a collision with and without reaching of QGP phase [15].

2.3 Kinematic Variables

In order to study the properties of the particles created in nucleus-nucleus collisions, it is useful to define several variables. The variables listed hereinafter are used to describe the kinematics of relativistic particles.

Let $\vec{p} = (p_x, p_y, p_z)$ be the momentum of a particle where $p_z = p_L$ is the longitudinal momentum, i.e. the component along the beam axis. Components p_x and p_y are therefore perpendicular to the beam axis and are incorporated into the transverse momentum p_T as follows [16]:

$$p_T = \sqrt{p_x^2 + p_y^2}. \quad (2.1)$$

Transverse momentum is of great importance as it is only associated with particles produced in the collision, whereas longitudinal momentum can be influenced by the beam particles.

Another useful variable is rapidity y , which in non-relativistic limit corresponds to the velocity of a particle, and is defined as [16]:

$$y = \frac{1}{2} \ln \left(\frac{E + p_L}{E - p_L} \right), \quad (2.2)$$

where E is the energy of the particle. To determine the energy of a particle, it is necessary to know its mass and thus to identify the particle. To remove this need for particle identification, a new variable called pseudorapidity η is defined as [16]

$$\eta = -\ln \left[\tan \left(\frac{\theta}{2} \right) \right], \quad (2.3)$$

which depends only on the so-called polar angle θ , i.e. the angle between the particle momentum vector and the beam axis.

The transverse momentum p_T and pseudorapidity η along with azimuthal angle ϕ , which is defined as the angle between the x -axis and the projection of the momentum into the plane transverse to the beam axis, are the variables most commonly used to measure the momenta of particles in heavy ion collisions. A conversion between these variables and cartesian momenta (p_x, p_y, p_z) can be expressed as follows [16]

$$\begin{aligned} p_x &= p_T \cos \phi, \\ p_y &= p_T \sin \phi, \\ p_z &= p_T \sinh \eta. \end{aligned} \tag{2.4}$$

The last variable to be mentioned here is the center-of-mass energy \sqrt{s} which is defined as [17]

$$\sqrt{s} = \sqrt{(E_1 + E_2)^2 - (p_1 + p_2)^2}, \tag{2.5}$$

where E_1, E_2 and p_1, p_2 are energies and momenta of the colliding nuclei respectively. For this variable, a useful formula, which expresses the relation between energies in collider and fixed-target experiments, yields

$$\sqrt{s} = \sqrt{m_1^2 + m_2^2 + 2E_1^{lab}m_2} \stackrel{E_1^{lab} \gg m_1, m_2}{\approx} \sqrt{2E_1^{lab}m_2}, \tag{2.6}$$

where E_1^{lab} is the total energy (kinetic + rest mass) of the projectile in the rest frame and m_1, m_2 are rest masses of the projectile and the target respectively.

Also, $\sqrt{s_{NN}}$ is the center-of-mass energy per nucleon. For a collision of two symmetric nuclei with nucleon number A , the relation between these energies is [16]

$$\sqrt{s_{NN}} = \frac{\sqrt{s}}{A}. \tag{2.7}$$

2.4 Particle Production

As heavy ion collisions cannot be observed directly, due to their extremely short duration and small scale, the best way to study them is by examining the properties of the particles produced during these collisions. This section focuses on exploring the methods to describe the formation of these products and what they tell us about the processes happening during the collision.

There are several different theoretical approaches which can be used to describe heavy ion collisions and predict different final state observables. These models rely on different assumptions. This section gives a brief description first of thermal models that assume global thermodynamic equilibrium and predict abundances of produced particles.

Secondly, hydrodynamic models which assume local thermal equilibrium and simulate the collective behavior of the matter. These are used to predict abundances, spectra as well as various flow related observables. These will be discussed in more detail later in this chapter.

Lastly, there are transport models which do not require the condition of equilibrium, but are based on microscopic simulations following the kinetic theory. They are hence especially useful at lower collision energies where the thermal equilibrium is hard to reach.

Statistical Models

Statistical models offer a great way to describe a system in thermal equilibrium at the point of chemical freeze-out where inelastic collisions cease and particle ratios are fixed. Hence the main aim of a statistical model is to compare theoretical predictions with experimental data in order to explore certain parameters of the model, e. g. temperature or chemical potential, and determine the values of such parameters at which the chemical freeze-out occurs, thus allowing further understanding of the QCD phase diagram.

Statistical physics describes the partition function and consequently the density of the particles of species i :

$$n_i = \frac{g_i}{2\pi^2} \int_0^\infty \frac{p^2 dp}{\exp[(E_i(p) - \mu_i)/T] \pm 1}, \quad (2.8)$$

with particle density n_i , spin degeneracy g_i , $\hbar = c = 1$, momentum p , total energy E and chemical potential $\mu_i = \mu_B B_i - \mu_S S_i - \mu_{I_3} I_i^3$ [18]. The quantities B_i , S_i and I_i^3 are the baryon, strangeness and third component of the isospin quantum number of the particle species i . The temperature T and the baryochemical potential μ_B are independent parameters while the volume of the system V , the strangeness chemical potential μ_S and the isospin chemical potential μ_{I_3} are fixed by three conservation laws for baryon number, strangeness and charge respectively [18]:

$$V \sum_i n_i B_i = Z + N, \quad (2.9)$$

$$V \sum_i n_i S_i = 0, \quad (2.10)$$

$$V \sum_i n_i I_i^3 = \frac{Z - N}{2}, \quad (2.11)$$

where Z and N are the proton and neutron numbers of the colliding nuclei.

To extract model parameters, the experimental data are fitted with model calculations. The most common way to do this is to fit hadron yield ratios so that the number of model parameters is minimized. The usual way to achieve this is by minimizing the distribution of χ^2 . Additionally, the quadratic deviation δ^2 is used to obtain the estimate of the systematic error. These quantities are defined as follows [19]

$$\chi^2 = \sum_i \frac{(R_i^{exp} - R_i^{therm})^2}{\sigma^2}, \quad (2.12)$$

$$\delta^2 = \sum_i \frac{(R_i^{exp} - R_i^{therm})^2}{(R_i^{therm})^2}, \quad (2.13)$$

where R_i^{exp} is the measured value of the ratio of hadron yields, σ_i is its uncertainty and R_i^{therm} is the value from model calculations. An important correction must be taken into account and that is the feed-down from weak decays affecting mainly the yields of pions and protons/antiprotons.

Figure 2.4 (left) shows an example of the statistical model fitted to experimental data.

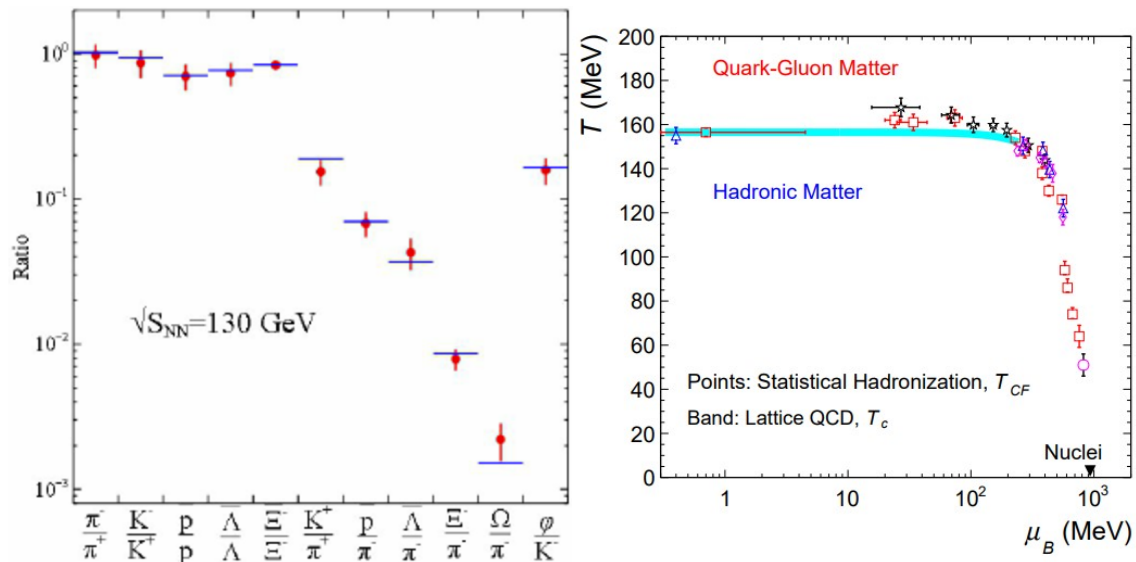


Figure 2.4: Left: Particle yield ratios from RHIC fitted with statistical model calculations [20] Right: Phenomenological phase diagram of strongly interacting matter constructed from chemical freeze-out points for central collisions at different energies [19].

As was mentioned before, these comparisons of experimental measurements with model calculations are performed to determine the values of temperature and baryochemical potential at the point of chemical freeze-out. Figure 2.4 (right) shows how this process is utilized to explore the phase diagram of nuclear matter.

Relativistic Hydrodynamic Models

Proposed initially by Landau, ideal hydrodynamics has recently been utilized to describe strongly interacting hadronic matter. The merits of this method include its generality and simplicity while also maintaining the ability to predict experimental observables quantitatively. It also offers the possibility to include various fluctuations in the initial conditions, equation of state or hadronization. However, similarly to statistical models, the presence of local thermal equilibrium is required. Another strength of these models is the possibility to compare the quark-gluon plasma phase and the experimental data from heavy ion collisions.

The evolution of an ideal fluid can be described by the following equations [21]:

$$\partial_\mu T^{\mu\nu} = 0, \quad \partial_\mu N^\mu = 0, \quad (2.14)$$

which can be interpreted as conservation of the energy-momentum tensor $T^{\mu\nu}$ and the particle number N^μ . These equations can be rewritten in the following form [21]:

$$T^{\mu\nu} = (\varepsilon + P)u^\mu u^\nu - P g^{\mu\nu}, \quad N^\mu = nu^\mu \quad (2.15)$$

with the energy density ε , pressure P , collective velocity four-vector u^μ , particle density n and $g^{\mu\nu} = \text{diag}(1, -1, -1, -1)$ is a metric tensor. However, the conservation laws only provide five equations of motion. In order to fully describe the hydrodynamic system (which has six degrees of freedom), the equation of state $P = P(\varepsilon, n)$, relating pressure with other thermodynamic variables, needs to be defined.

Transport Models

Transport models offer another way of calculating particle yields and study dynamics of heavy ion collisions. Their biggest advantage is that they can be implemented even without reaching thermal equilibrium. In principle, transport models treat a collision as a superposition of single NN collisions with products that are then ejected through space-time with the possibility of further interactions. There are two families of transport models, cascade models or Boltzmann-Uehling-Uhlenbeck (BUU) and Quantum Molecular Dynamics (QMD) type models.

In cascade models, the particles are assumed to be classical, point objects which obey the time evolution determined by the following equation [22]

$$\left(\frac{\partial}{\partial t} + \vec{\nabla}_p \epsilon \cdot \vec{\nabla}_r - \vec{\nabla}_r \epsilon \cdot \vec{\nabla}_p \right) f_a(\vec{r}, \vec{p}; t) = I_{coll}[f_a(\vec{r}, \vec{p}; t)], \quad (2.16)$$

where f_a is the one-body particle distribution function of particle species a , ϵ is the single particle energy and I_{coll} is the two-body collision integral which includes decay, scattering or quantum effects. The advantage of this approach is that the model treats the system as a one-body problem. However, it is also necessary to solve equation (2.16) for every relevant particle species separately.

Complex many-body systems like heavy ion collisions can be simulated using Quantum Molecular Dynamics. Contrary to BUU-like models, QMD models consider the many-body system as a product wave function of single-particle Gaussian distributions. As a result, calculations of heavy ion collisions on event-to-event basis are possible.

Recently, models that combine the qualities of the methods mentioned above have been put to use. One of these models is the SMASH (Simulating Many Accelerated Strongly-Interacting Hadrons) model [23]. In this model, methods of ideal hydrodynamics models are used to describe the thermal equilibrium phase of the evolution while the hadron gas phase reached after the chemical freeze-out is described by the UrQMD transport model.

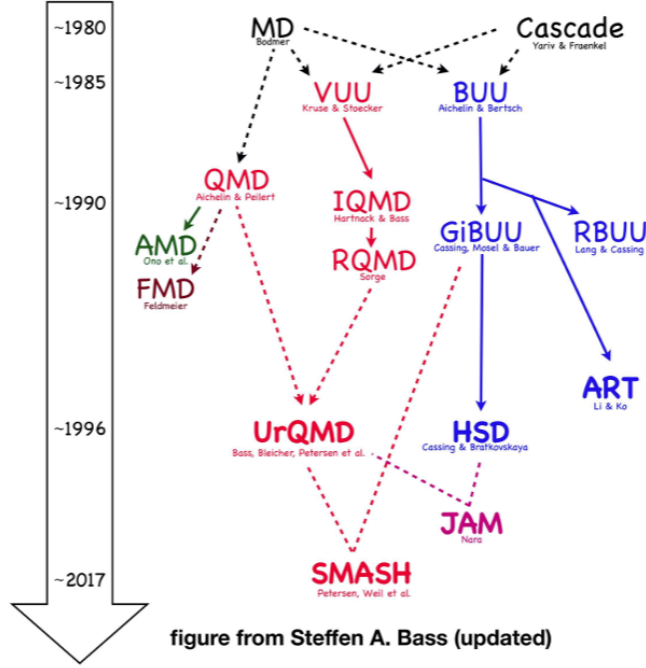


Figure 2.5: The evolution of kinetic transport models [24].

2.5 Nuclear Modification Factor

The yield of large p_T particles created in heavy ion collisions should scale with the quantity of basic binary collisions in the absence of medium effects (p+p collisions). However, this scale can be altered by the collision-produced medium. Nuclear modification factor R_{AB} is considered to be a useful observable which can measure this scaling. It can be defined as

$$R_{AB}(y, p_T) = \frac{1}{\langle T_{AB} \rangle} \frac{d^2 N_{AB}/dp_T dy}{d^2 N_{pp}/dp_T dy}. \quad (2.17)$$

It is the ratio of the number of particles produced in A+B collisions to the number of particles produced in p+p collisions scaled to the nuclear overlapping function which is defined $\langle T_{AB} \rangle = \langle N_{col} \rangle / \sigma_{NN}^{inel}$, ratio of average number of binary collisions divided by nucleon-nucleon inelastic cross section. For collisions of identical nuclei, $A = B$. If there are no effects of the medium, $R_{AB} = 1$, if $R_{AB} < 1$, it denotes the suppression effect and if $R_{AB} > 1$, it is the enhancement of the particle production. To determine the R_{AB} factor it is needed to measure the p+p reference. The comparison of p+p and Pb+Pb measurements from ALICE experiment [25] is shown in Figure 2.6.

The distributions in Figure 2.6 for peripheral collision show similar shapes for p+p and Pb+Pb collisions, whereas central collisions depict different p_T -dependence for p+p for intermediate and large p_T . The downward shift of the A+A distribution compared to the p+p collisions is caused by the absorption process causing suppression of particles at high- p_T . The shift to the left is caused by the energy loss of particles showing that more energetic particles are redistributed to lower energies in case of heavy-ion collisions.

The p_T distribution can be described by a power law that depends on the energy of colliding particles. The measurements from RHIC (with lower collision energy

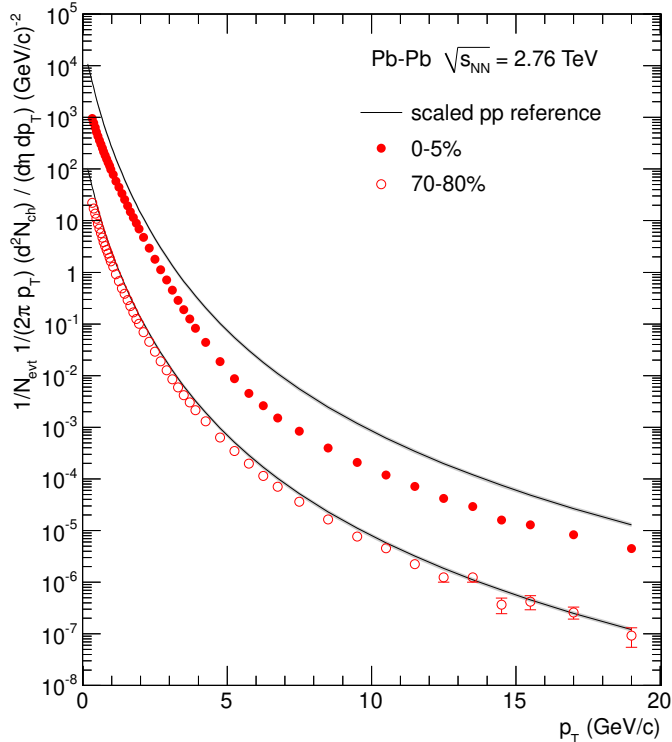


Figure 2.6: The p_T distributions of primary charged particles at mid-rapidity ($|\eta| < 0.8$) in central (0 - 5%) and peripheral (70 - 80%) Pb+Pb collisions at $\sqrt{s_{NN}} = 2.76$ TeV. The scaled pp references are shown as the two curves, the upper for 0 - 5% centrality and the lower for 70 - 80% [25].

than LHC), show a steeper decline in the p_T distribution. The steeper shape causes the distribution to end at lower p_T . It is also expected to observe more extensive suppression due to the spectral shape.

Figure 2.7 shows results for R_{AA} p_T -distribution for central and peripheral collisions. Central collisions show suppression of more than factor 5 in comparison with peripheral collisions and clear p_T dependence. The peak observed at intermediate p_T can be explained by a radial flow. At high p_T the particles are expected to have high enough energy to escape the medium without losing a large amount of energy, thus causing a rise in the distribution. At low p_T the distribution is not scaled with the number of collisions due to the effects of soft production. The peripheral collisions show no significant p_T dependence with no or small suppression of hadrons.

A comparison of measurements from experiments at RHIC and LHC is shown in Figure 2.8. The comparison shows a larger p_T range for LHC measurement, as expected due to the flatter p_T distribution described above. The R_{AA} is smaller at LHC than at RHIC for intermediate p_T suggesting greater energy loss at LHC and therefore a medium with large temperature and density.

On the other hand, Figure 2.8 (right) shows that particles which do not interact strongly with the medium (e.g. photons or W^\pm and Z bosons) have R_{AA} approximately 1 and thus do not lose energy in the medium.

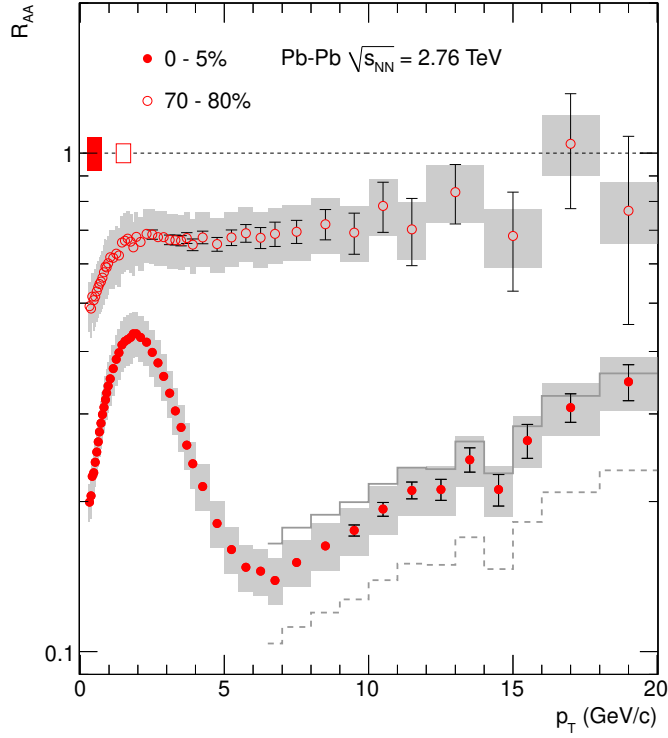


Figure 2.7: R_{AA} in central (0 - 5%) and peripheral (70 - 80%) Pb-Pb collisions at $\sqrt{s_{NN}} = 2.76$ TeV. The results indicate strong suppression in central collisions for $p_T > 6.5$ GeV/c. [25].

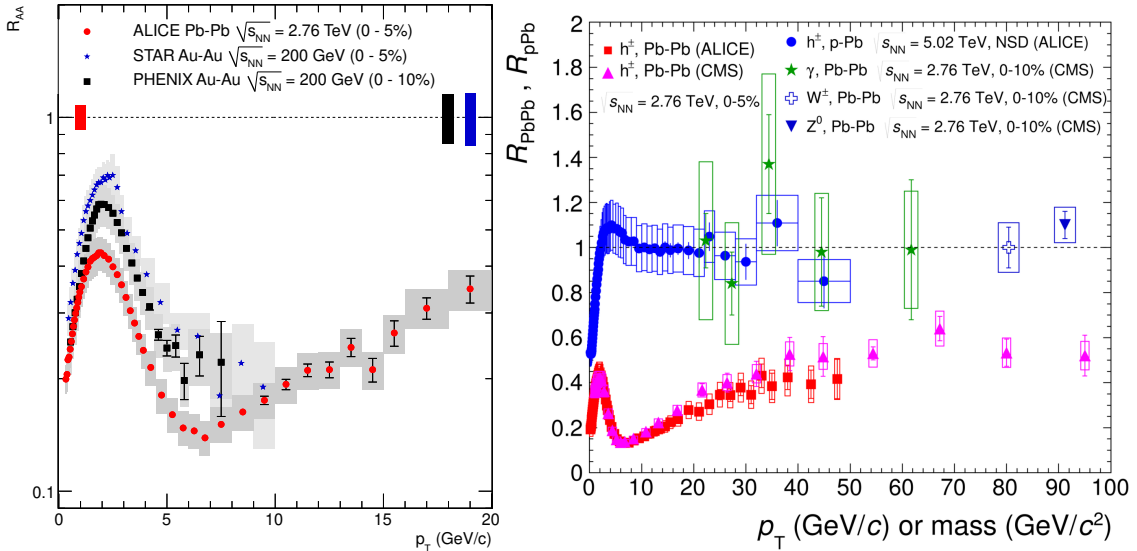


Figure 2.8: Left: Comparison of R_{AA} in central Pb+Pb collisions at LHC to measurements at $\sqrt{s_{NN}} = 200$ GeV by the PHENIX and STAR experiments at RHIC [25]. Right: R_{AA} in p+Pb and Pb+Pb collision at LHC for hadrons as well as photons and W^\pm and Z bosons [26].

2.6 Dilepton Production

A quark and an antiquark can interact in the quark-gluon plasma to create a virtual photon, which then decays into a lepton and its antiparticle. The created lepton-antilepton pair's system is known as a dilepton. The lepton and the antilepton must travel through the collision area and arrive at the detectors in order to be observed. Only through electromagnetic force can leptons interact with other particles. Since leptons interact weakly and are unlikely to experience more collisions once they are created, their free paths are predicted to be rather long. One may be able to ascertain the temperature of the plasma by extracting the dilepton spectrum from the quark-gluon plasma. Other dilepton sources must be eliminated in order to do this. Dileptons produced by the decay of heavy flavor hadrons might be one of these sources.

Dilepton pairs provide a great opportunity to study the medium created in collisions. They are referred to as electroweak probes, meaning they interact solely via electroweak force, thus not being affected by the strongly interacting medium. A great advantage of the dilepton pairs is that they can be created in any stage of the collision and thus their mass spectrum provides crucial information about the evolution of the collision. However, they suffer from large background.

The earliest created (in the initial stage) dileptons are created mostly by hard processes such as the Drell-Yan process where colliding nuclei emit a quark that annihilates with a sea quark from the other nucleus creating a virtual photon that further transforms into a dilepton pair. As these dileptons are created in the initial stage, they populate large invariant masses, $m_{ll} \sim 3$ GeV and their overall mass contribution is very small.

Dileptons coming from the pre-equilibrium stage are created by the semileptonic decay of heavy flavor hadrons and decays of quarkonia. These measurements are used to probe the p_T range of the collision and are sensitive to the production mechanism (initial correlation of heavy quarks).

To probe the temperature of the system, dileptons originating from decays of direct virtual thermal photons are used. These are observed in the expansion stage. In the hadronization phase, light flavor meson decays and Dalitz decays play a significant role in the contribution to the dilepton channel. Dalitz decays are the ones that dominate after thermal freeze-out while resonance decays dominate after the phase transition. Additional information can be inferred from measuring dileptons coming from light vector mesons. It is expected that simultaneously with the deconfinement from hadronic matter to QGP, chiral symmetry could be restored (symmetry between left and right-handed components of the wave function). This in turn would have an effect on the mass and widths of light vector mesons. Out of these, the ρ meson is the most important because it has a very short lifetime and large dilepton decay width. The observation of the ρ spectral function can provide information about the creation of hot hadronic matter due to its mass shift and/or broadening. An example of the dilepton spectrum is shown in Figure 2.9. The figure shows the comparison of a simulation of several hadron decays and dielectron invariant mass spectra from STAR. The bottom figure shows the ratios of measured data to hadronic cocktail simulations. The comparison shows good agreement of measured values and cocktail in $0.76 - 0.80$ GeV/ c^2 and $0.98 - 1.05$ GeV/ c^2 mass regions corresponding to ω and ϕ , respectively. Similarly, the cocktail successfully describes

dielectron yields in the higher mass region for the signal coming from decay leptons and charm pairs. However in the lower mass region, $0.20 - 0.76 \text{ GeV}/c^2$, there is a clear abundance over the simulated cocktail. The data fit reasonably well with models utilizing broadened ρ as opposed to models incorporating solely ρ from a vacuum, thus hinting at the presence of hot hadronic matter as discussed above.

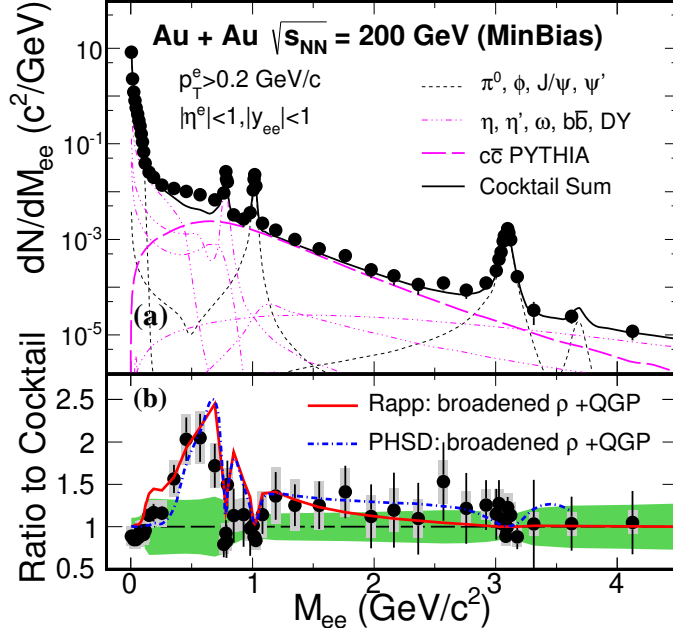


Figure 2.9: (a) e^+e^- invariant mass spectrum from $s_{NN} = 200 \text{ GeV}$ Au+Au minimum bias (0 - 80%) collisions compared to a hadronic cocktail simulation. (b) Ratios to cocktail for data and model calculations [27].

2.7 Strangeness Enhancement

The production of the strange quarks was expected to have a great significance in the high energy measurements and observation of QGP [28]. Unlike the up and down quarks, strange quarks are not present in the colliding nuclei and therefore all strange quarks and antiquarks which are detected must be created from the kinetic energy of the incoming nuclei. Thus in the collisions where the quark-gluon plasma phase is not reached the strange production is suppressed due to the large mass of s quark compared with u and d quark. Furthermore, due to the increased gluon density in heavy ion collisions (with the QGP), gluon fusion becomes a dominant production channel for the formation of $s\bar{s}$ pairs in the QGP. Also because of the high temperature of the QGP phase, the thermal production of $s\bar{s}$ pairs becomes possible. Therefore, the strangeness production could be enhanced compared with p+p collisions.

The strangeness enhancement is expected to be observed as a consequence of partonic processes that saturate the strange quarks in QGP within the lifetime of the created fireball. Afterwards, the hadronization process preserves the number of strange quarks resulting in larger strangeness production in A+A collisions with respect to p+p due to the strangeness conservation. The conservation shows a dependence on the volume of the system, which is larger for A+A collisions.

The measurements at the higher LHC energies[29] (Figure 2.10) confirm the strangeness enhancement. It was observed that the yield ratio decreases with the collision energy. This indicates a saturation of strange particles (per pion pair) in heavy ion collisions at the top SPS energy, whereas in p+p the amount increases. Yet the yield in A+A collisions is higher hinting at different strangeness production mechanisms in large collision systems.

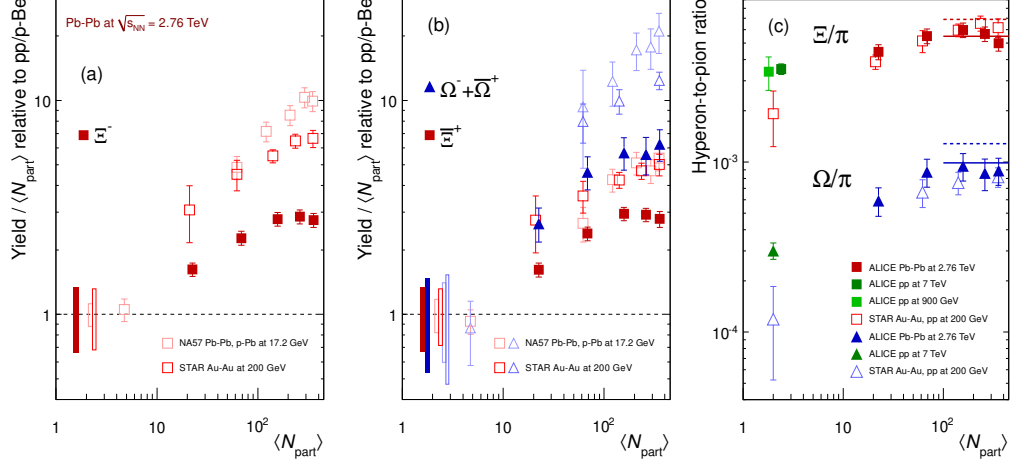


Figure 2.10: (a,b) Enhancements in the rapidity range $|y| < 0.5$ as a function of the mean number of participants $\langle N_{part} \rangle$, showing LHC (ALICE, full symbols), RHIC and SPS (open symbols) data. (c) Hyperon-to-pion ratios as a function of $\langle N_{part} \rangle$, for A-A and pp collisions at LHC and RHIC energies. The lines mark the thermal model predictions. Figure from [29].

Chapter 3

Collectivity in Heavy Ion Collisions

3.1 Radial Flow

The bulk matter created after a collision is very dense and hot and it can be, when conditions are suitable, described by the aforementioned hydrodynamical models. After the creation and quick realization of thermalization, the medium will expand due to initial pressure gradients leading to global hydrodynamic flow. The expansion and cool-down is ongoing until the system undergoes a transition to a hadron gas phase. The dynamics of the system created in heavy-ion collisions is accurately described by the hydrodynamic models for a large range of collision energies.

The transverse expansion (radial flow) causes a blueshift of the measured transverse momenta spectra of the particles when compared to p+p collisions. At low p_T , where bulk of the particles are produced, one can express (using non-relativistic kinematics) the observed $p_T \approx p_T^{th} + m \langle v_T \rangle$ as the sum of thermal contribution p_T^{th} (independent of the hadron mass) and a part coming from collective expansion - average flow velocity $\langle v_T \rangle$ times hadron mass.

This effect can be well observed in Figure 3.1 which shows a comparison of p_T spectra of π^\pm , K^\pm , p from the LHC of p+p and Pb-Pb collisions. Due to the collective flow, the heavy-ion collision spectra are flatter compared to the p+p case. Since the effect is mass dependent, for heavy hadrons such as protons, the radial flow even generates a so called “shoulder” in the spectrum at low p_T as can be clearly seen in Figure 3.1.

To extract the information about the created system at the point of kinetic freezeout so called Blast-wave model fits [31] of the hadron spectra are performed. These fits use parametrization of hadron spectra shapes which are deduced from combination of thermal models and radial flow. Two parameters which these fits allow extracting are the decoupling temperature T_{kin} and the average transverse velocity (radial flow) $\langle v_T \rangle$. The results for p+p, p+Pb and Pb+Pb systems are shown in Figure 3.2. These results are presented in several multiplicity intervals decreasing from right to left. The figure allows for a comparison of the three systems’ spectral shapes and shows larger average velocities for pp than for the denser Pb+Pb system.

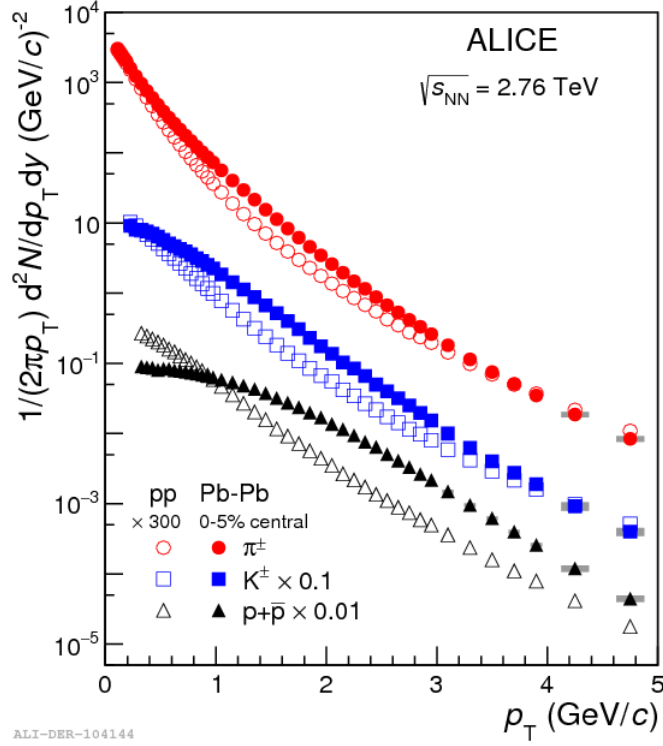


Figure 3.1: Invariant yields in Pb+Pb and p+p collisions of π^\pm, K^\pm, p [30].

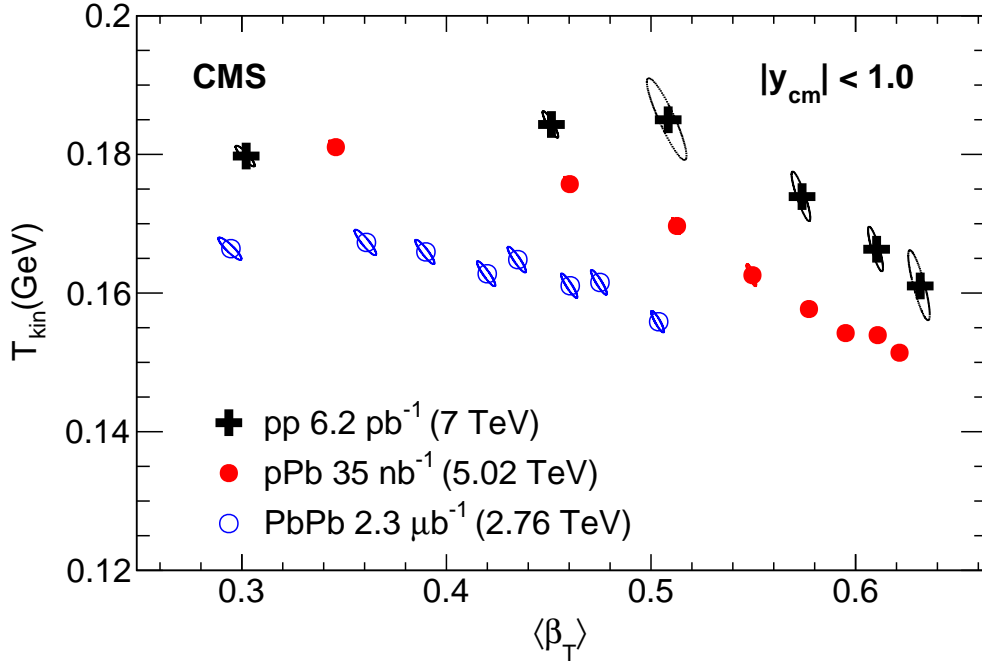


Figure 3.2: The extracted kinetic freeze-out temperature T_{kin} versus the average radial flow velocity $\langle\beta_T\rangle$ from a simultaneous Blast-wave fit to the K_S^0 and Λ p_T spectra for p+p, p+Pb and Pb+Pb collisions [32].

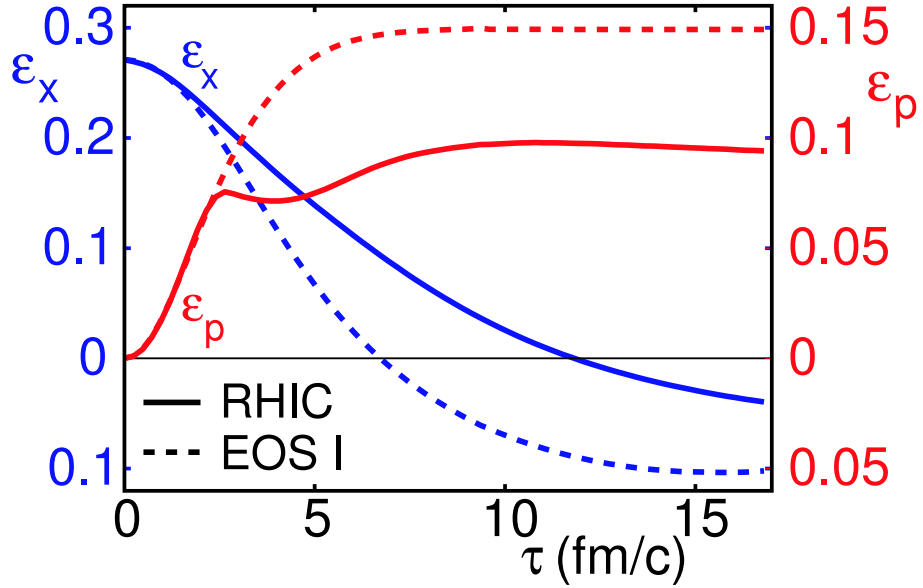


Figure 3.3: Time evolution of the spatial eccentricity ε_x and the momentum anisotropy ε_p for Au+Au collisions at RHIC with $b = 7$ fm [33].

3.2 Anisotropic Flow

The anisotropic flow is created during non-central collisions. During the evolution of the produced medium, the spatial anisotropy of the energy density transforms into pressure gradients which then drive the expansion of the system and cause anisotropy of the produced particles. Experimentally, the measurement of anisotropic flow is the most direct evidence of hydrodynamic behavior. Due to its sensitivity to the system properties in the earliest stages of the collision and the system evolution, it is a valuable observable to study properties of the QGP. This behavior can be supported by EoS calculations shown in Figure 3.3.

The figure shows momentum anisotropy ε_p and spatial anisotropy ε_x quantifying the deformation of the overlap zone. The solid line depicts results for EoS with RHIC initial conditions, whereas the dashed line depicts the EoS with high energy density in the initial stage with a massless ideal gas. These eccentricities are compared with respect to their time evolution. The spatial eccentricity goes to 0 with the time of the freeze-out showing that in the ideal case, the medium becomes in-plane-elongated, while for RHIC the ε_x disappears later. This affects the evolution of ε_p that for the ideal case reaches a maximum at the time of ε_x disappearance. The RHIC behavior is more complicated. In the early stages, the rise of ε_p stops demonstrating the radial expansion of the system which is increasing its isotropy. After the fireball exits the mixed phase and finishes the phase transition, the system reacts to the remaining ε_x and ε_p grows further. This evolution depicts hard QGP EoS for RHIC energies and shows how studies of system anisotropy may provide information about the evolution of the system.

To study anisotropic flow one may take a look at the azimuthal particle distribution which is expected to be anisotropic with respect to the reaction plane (illustrated in Figure 3.4 left). The reaction plane is determined by the vector of the impact parameter and the beam direction. The azimuth of the reaction plane is called the

reaction plane angle, which acts as a symmetry plane of the collision. As the reaction plane cannot be observed directly, one can use the following symmetry planes: the participant plane defined by the symmetry plane of participating nucleons or the event plane which can be estimated using anisotropic flow measurements. Instead of studying directly the azimuthal distribution it is more advantageous to look into its Fourier decomposition

$$E \frac{d^3 N}{d^3 p} = \frac{d^2 N}{2\pi p_T dp_T dy} \left(1 + \sum_{n=1}^{\infty} 2v_n \cos[n(\phi - \Psi_{RP})] \right), \quad (3.1)$$

where v_n are coefficients describing the event anisotropy [34]. The magnitude of v_n is dependent on the system size, energy, centrality and other event properties. The coefficients v_1 and v_2 are commonly referred to as the directed flow and the elliptic flow respectively (see Figure 3.4 right). Directed flow corresponds to the deflection of the particles transverse to the beam axis. Elliptic flow and higher harmonic coefficients are related to ellipticity, triangularity, etc., which are illustrated in Figure 3.5.

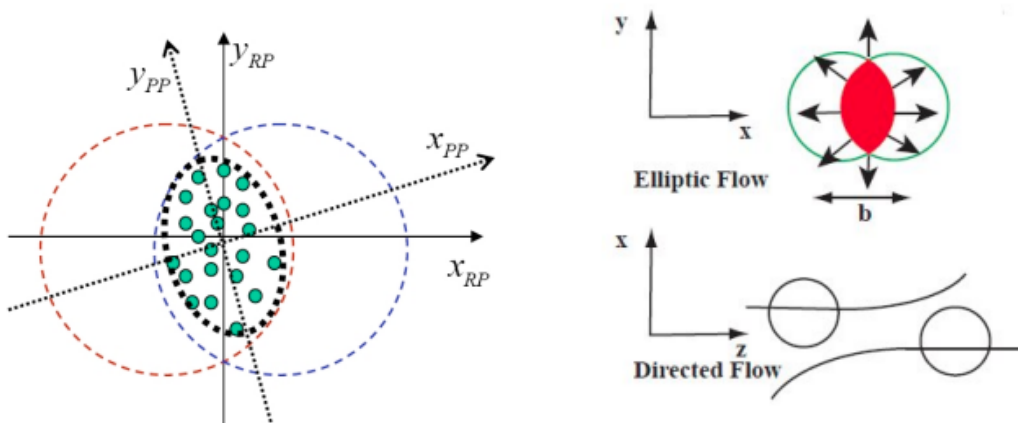


Figure 3.4: Left: The definitions of the Reaction Plane and the Participant Plane coordinate systems. Right: Diagrams of elliptic and directed flow [34].

3.2.1 Elliptic flow

The most interesting of the harmonic coefficients of the Fourier expansion (3.1) is the elliptic flow v_2 , as it can be related to collective expansion in nuclear collisions, according to hydrodynamic calculations [36]. Since the spatial anisotropy generally reduces with system expansion, elliptic flow is particularly susceptible to the early stages of the system evolution. Also, elliptic flow is sensitive to the degree of thermalization of the system at the early stages of the system evolution. AGS and SPS accelerators have been used to study elliptic flow in ultra-relativistic nuclear collisions, demonstrating that, at their energy range, elliptic flow is "in-plane" ($v_2 > 0$).

However, the first measurements showed very little agreement between ideal hydrodynamics predictions and experimental data. Figure 3.6 shows the comparison of the

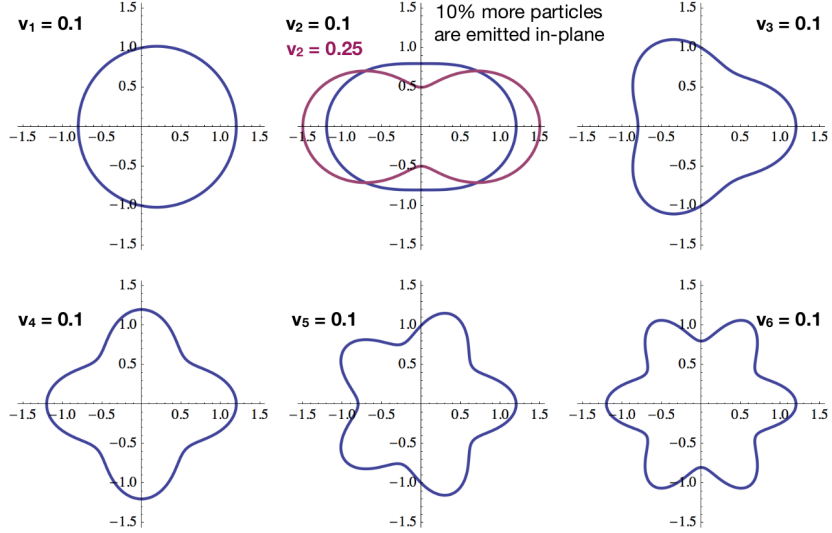


Figure 3.5: A visualization of directed and elliptic flow and higher harmonic coefficients [35].

p_T dependence of the elliptic flow with hydrodynamical calculations and measured data from NA49 experiment for Pb+Pb collisions at $\sqrt{s} = 17$ AGeV [37].

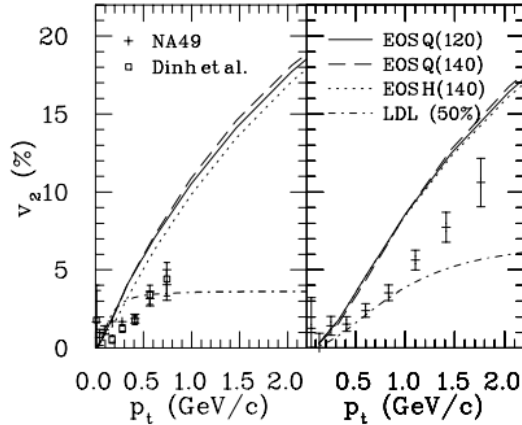


Figure 3.6: A comparison of ideal hydrodynamics calculations with first v_2 measurements [38].

With the advancement of accelerator technologies, researchers have been able to execute v_2 measurements for a variety of collision energies up to LHC energy domain. Figure 3.7 shows the collision energy dependence of the elliptic flow for 20%-30% centrality. A continuous increase in the magnitude of v_2 for this centrality region from RHIC to LHC energies is clear. The overall shape of the energy dependence can be explained by various multiple domains of characteristic dynamics of the colliding system. Very high values of v_2 for energies under 2 GeV are caused by a rotation of the collision system that leads to fragments being emitted in-plane. The steep decline into negative values for energies between 2 and 4 GeV is caused by the small velocity of the incoming nuclei and spectators. The presence of the spectator matter causes "squeeze-out" (inhibition of in-plane particle emission). For energy values higher than 4 GeV, the elliptic flow reaches positive values as the initial eccentricity leads to pressure gradients causing the elliptic flow. Comparing RHIC results to LHC

results, a 30% increase can be observed, as predicted by the ideal hydrodynamic models and models combining hydrodynamics and hadron cascade afterburner.

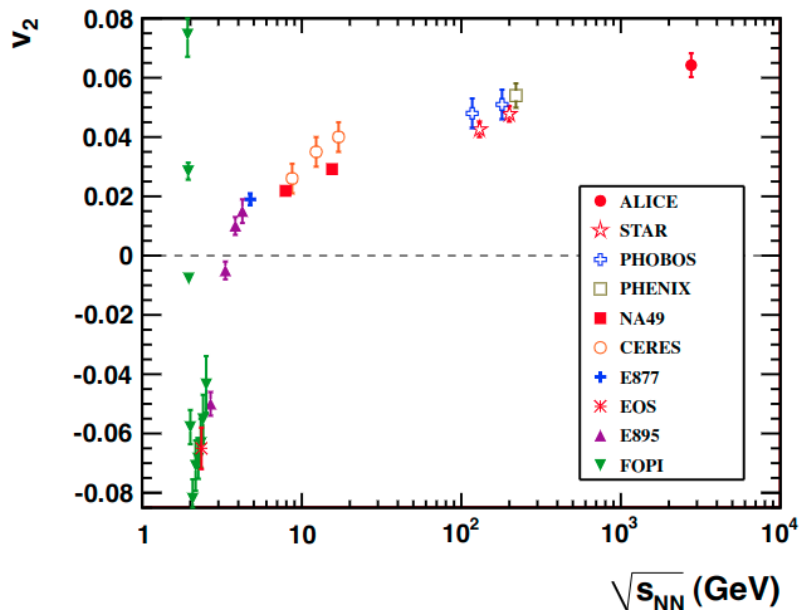


Figure 3.7: The collision energy dependence of elliptic flow in the 20%-30% centrality class [39].

Another collision property that affects the formation of the elliptic flow is the centrality of the collision. In Figure 3.8, an example of the dependence of the elliptic flow on centrality is presented. The results show strong centrality dependence with a rise of v_2 to maximum for event of 50% centrality (mid-peripheral events). This shows the initial spatial anisotropy effects of the medium on v_2 . The most central collisions have a circle-like overlap shape thus having low v_2 values, whereas, for peripheral collisions, a rise in v_2 due to the almond-like overlap shape can be observed. The small drop for very peripheral collisions is caused by the fact, that the system is not big enough and long-lived enough to transfer the initial shape to the final flow. The centrality dependence is essential for examining the thermodynamic equilibrium. Ideal hydrodynamics predictions suggest that at a given energy, the v_2 scales with the eccentricity of the almond-like overlap shape. In case the system does not reach thermal equilibrium the system does not behave as an ideal fluid and the scaling is broken.

Figure 3.9 shows elliptic flow divided by the spatial anisotropy of the participant zone (ϵ). The bands in the upper part display the hydrodynamic limits for various beam energy (blue for STAR). A relative measure of centrality is displayed on the horizontal axis (the most central collisions correspond to the rightmost point). As can be seen, the STAR data follow a smooth trend and at RHIC energies the most head-on collisions reach the hydrodynamic limit. The strong elliptic flow discovered in central Au+Au collisions at RHIC which agrees with ideal hydrodynamics established the concept of strongly coupled quark-gluon plasma, sQGP. It was soon realized that in order to fully describe data the hydrodynamics needs to account also for a viscosity of the produced matter (η). It was discovered that relatively small

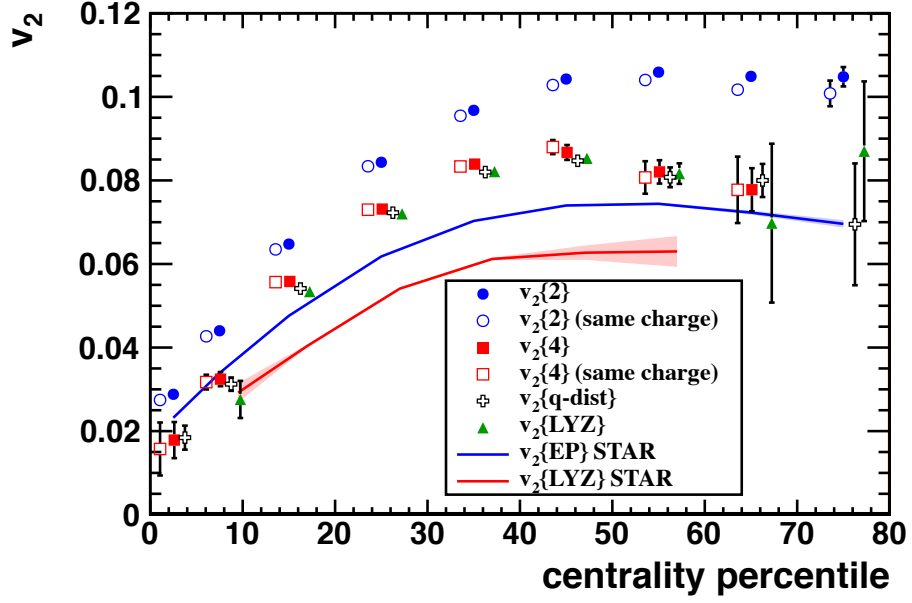


Figure 3.8: The collision centrality dependence of elliptic flow [39].

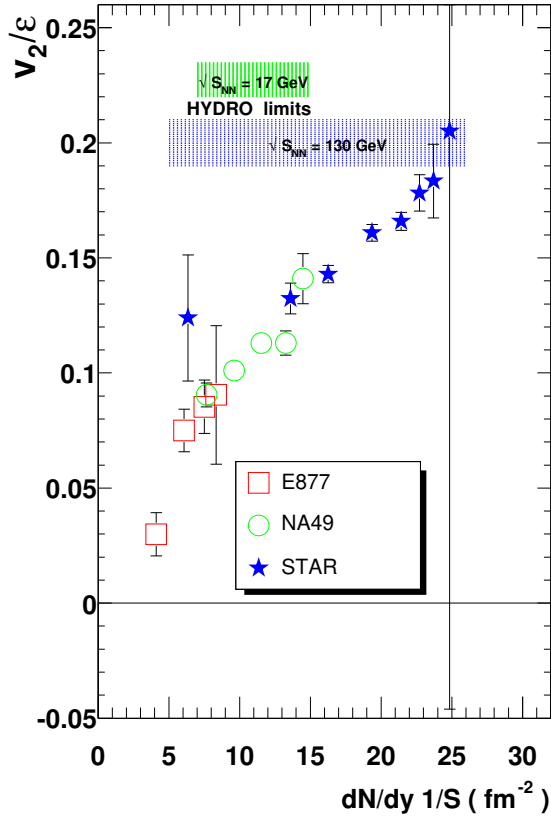


Figure 3.9: Elliptic flow v_2 divided by the spatial anisotropy of the participant zone ϵ as a function of charged particle density [40].

viscosity effects can result in a considerable drop in the resulting elliptic flow compared to the ideal hydrodynamics scenario, along with various indirect indicators that thermal equilibrium is not fully achieved in central Au+Au collisions. If other

effects responsible for an increase in elliptic flow were not identified, lower values of elliptic flow would dispute experimental measurements. Among these effects, the following have been described:

- Ideal hydro calculations, if adjusted to describe spectra, yield larger elliptic flow than thought previously. This means it is key to describe the spectra and elliptic flow simultaneously,
- In some models, the initial eccentricity can take notably larger values than in the optical Glauber model that is usually used to set initial conditions in hydro calculations (larger eccentricities inevitably lead to larger elliptic flow),
- The final values of elliptic flow may be increased by the gradients in the initial velocity.

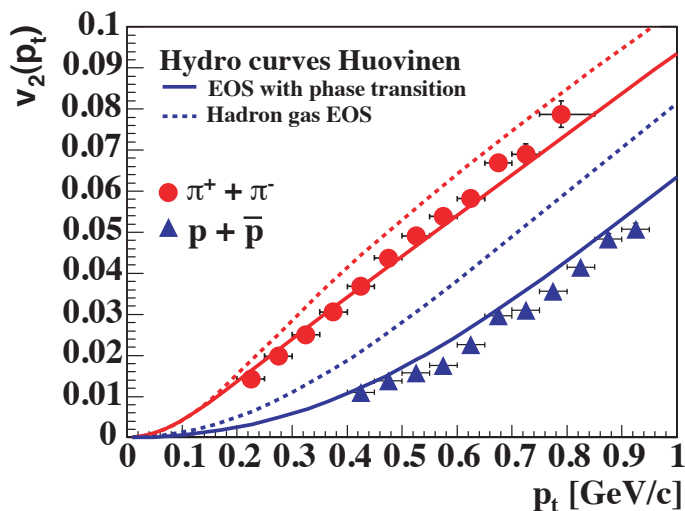


Figure 3.10: The p_T dependence of elliptic flow of protons and pions with hydrodynamic calculations for a hadron gas [34].

The study of elliptic flow with respect to p_T shows a clear dependence on the mass of the particle. Figure 3.10 shows a comparison of the p_T dependence of elliptic flow for protons and pions. From this figure, it is clear that the dependence of the elliptic flow on the mass of the particle with v_2 at a fixed p_T decreases with increasing mass. The solid lines show hydrodynamic predictions for the equation of state with a phase transition from QGP to hadron gas. These predictions better describe measured data for both types of particles. It is obvious that the effect of a phase transition is less significant for the protons than the pions, as the lighter particles are more affected by the temperature, and therefore less sensitive to the collective flow velocity and vice versa for the heavier protons. Measurements also show that the elliptic flow of the different mass particles at low p_T can be described quite well by a set of four freeze-out parameters: the temperature, the mean radial flow velocity, the azimuthal dependence of the radial flow velocity and the source deformation. The detected mass ordering holds up to large p_T , although less notable because the v_2 of the different particles start to approach one another.

At intermediate p_T , baryon-meson grouping was observed, showing that partons are those that flow and are just grouped together at the point of freeze-out, this is known as the coalescence model. The coalescence model is used to describe the unexpected particle type dependence and magnitude of v_2 at large p_T . This so called *constituent quarks (NCQ) scaling* has been observed both at RHIC top energies (Figure 3.11) and LHC (Figure 3.12). This observation is of remarkable importance as it indicates that the system was in a deconfined phase since the collectivity was achieved already on the quark level. A consequence of this phenomenon is the enhanced relative production of baryons in this transverse momentum region leading to the constituent quark scaling of elliptic flow $v_2(p_T) \approx n v_2(p_T/n)$, where n is the number of constituent quarks. A crucial test of constituent quark scaling was the ϕ meson that has the mass of a proton but contains only two quarks and scales with the other mesons, proving that the scaling is indeed dependent on the number of constituent quarks and not just an effect of mass of the particles.

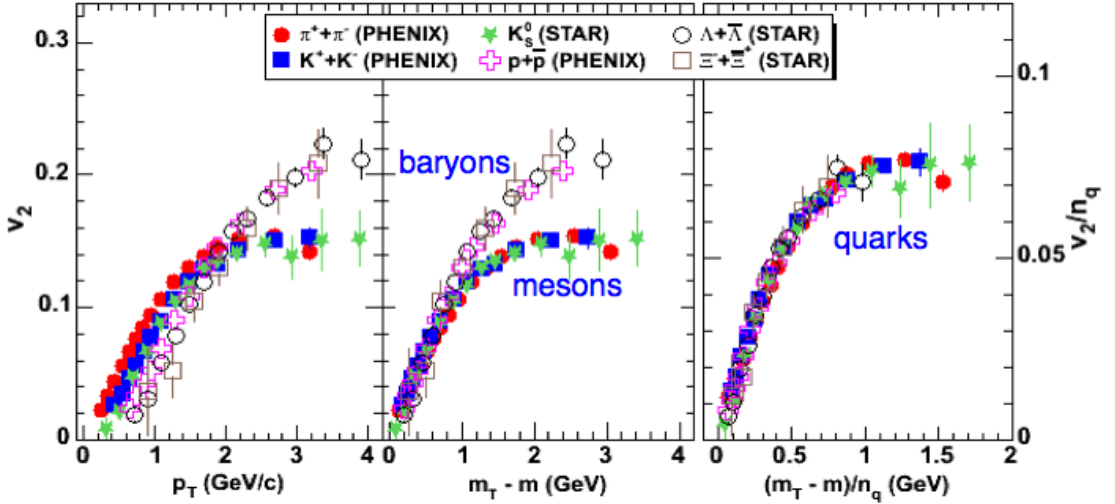


Figure 3.11: v_2 for $\sqrt{s_{NN}} = 200$ GeV Au+Au as a function of p_T [34].

Since NCQ scaling is taken as a signature of QGP creation at the top RHIC and LHC collision energies, it is of interest to search for a point where the NCQ scaling breaks down. The Beam Energy Scan project at RHIC [41] focused on lowering the collision energy in order to broaden the understanding of the phase transition to QGP. Figure 3.13 shows the scaled elliptic flow dependence on scaled transverse kinetic energy from collisions at $\sqrt{s_{NN}} = 3, 27, \text{ and } 54.4$ GeV. It is clear that at 3 GeV the NCQ scaling disappears. This could imply that the partonic interactions, that dominate in the QGP phase, are replaced by baryonic interactions, and therefore, the QGP phase is not reached. It makes this region of collision energies particularly interesting for further explorations.

The measurements of $v_2(p_T)$ also show other interesting phenomena such as the fact, that heavy quarks participate in the collective expansion, even though their mass is 200 times larger than the mass of light quarks.

The measurements of heavy quarks at the LHC in Figure 3.14 show that v_2 can provide information about the strength of the interaction of heavy quarks with the medium. The figure shows high values of v_2 for D meson which is almost on the

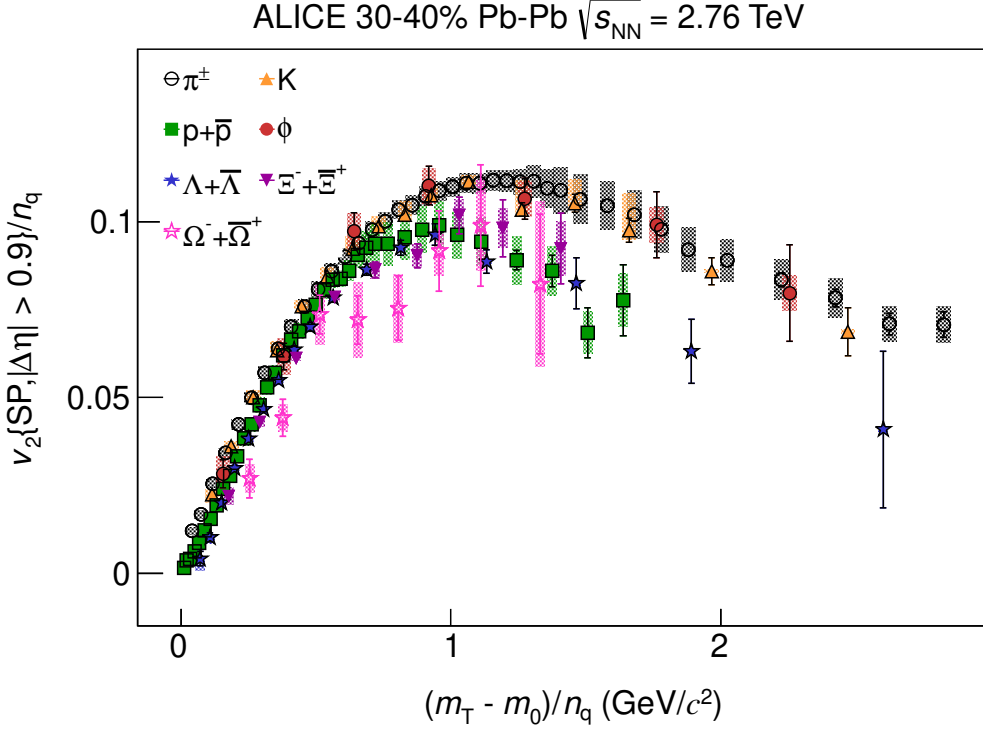


Figure 3.12: The $(m_T - m_0)/n_q$ dependence of v_2/n_q for π^\pm , K, $p+\bar{p}$, ϕ , $\Lambda+\bar{\Lambda}$, and $\Xi^-+\bar{\Xi}^+$ for Pb+Pb collisions for 30-40% centrality class at $\sqrt{s_{NN}} = 2.76$ TeV [39].

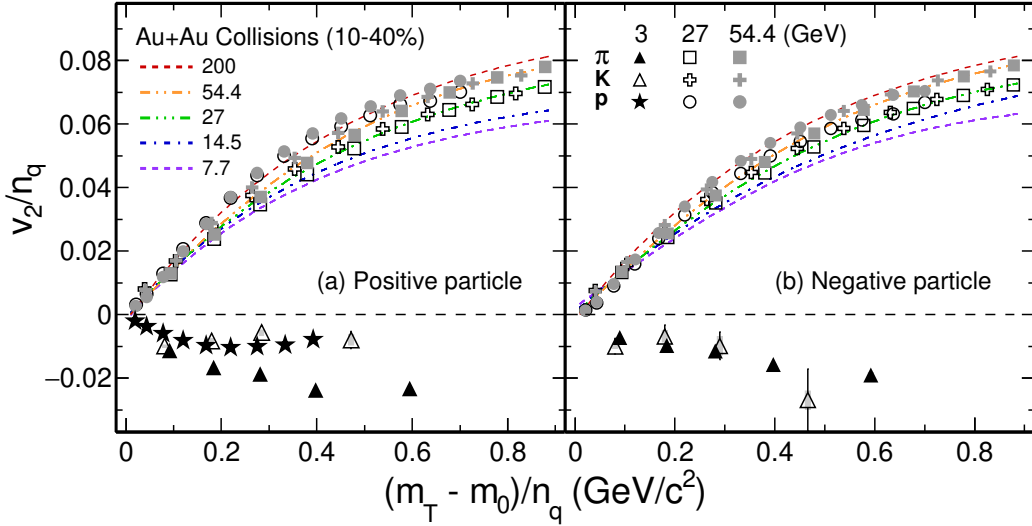


Figure 3.13: v_2 scaled by the number of constituent quarks as a function of scaled transverse kinetic energy $(m_T - m_0)/n_q$ for pions, kaons and protons from Au+Au collisions in 10-40% centrality at $\sqrt{s_{NN}} = 3, 27,$ and 54.4 GeV for positively charged particles (left panel) and negatively charged particles (right panel) [42].

level of light hadrons. This implies that the interaction between the deconfined medium and c quark is so strong that it makes even the heavy quark participate in the collective expansion (flow). On the other hand the value of $v_2 J/\psi$ is much smaller. This is caused by the fact, that the D meson is made by coupling via the

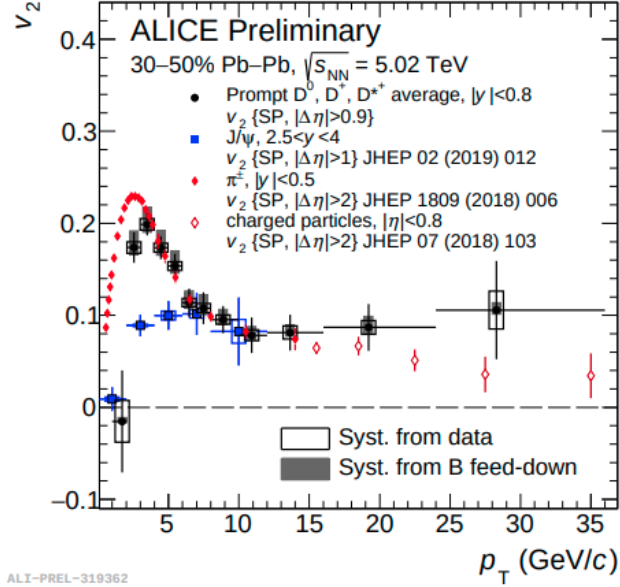


Figure 3.14: Average prompt D^0 , D^+ , and D^+ + v_2 in Pb-Pb collision at $\sqrt{s_{NN}} = 5.02$ TeV in the 30%-50% centrality class, compared to that of charged pions for $p_t < 15$ GeV/ c , charged particles $p_t > 15$ GeV/ c at mid-rapidity, and inclusive J/ψ mesons at forward rapidity [43].

coalescence of a charm and light quark both of which flow. The J/ψ is composed of two bound charm quarks and hence has zero color charge. The observed non-zero value of v_2 can be attributed to flow of non-directly produced fraction of J/ψ mesons. These non-direct particles come from coalescence (regeneration) of initially dissociated quarks and hence obtained flow on the quark level. However, this can happen only at LHC where number of c quarks created in single collision is high enough so that the coalescence is possible. At RHIC energies the possibility of J/ψ creation via coalescence is negligible and indeed the observed v_2 inclusive J/ψ mesons is consistent with non-flow.

3.2.2 Higher-order Flow Coefficients

For smooth matter distribution of the colliding nuclei, the odd flow coefficients are expected to be zero. Due to the fluctuations in the positions of the participating nucleons and in the matter distributions, the plane of symmetry fluctuates event-by-event around the reaction plane giving rise to the odd Fourier coefficients. The centrality dependence for the triangular (v_3) and the quadrangular (v_4) flow of charged particles have been measured.

Figure 3.15 shows results for anisotropic flow coefficients in different centrality classes together with the prediction from hydrodynamic calculations. For the most central collisions, the v_2, v_3, v_4 coefficients have similar magnitudes with significant growth for more peripheral collisions. Smaller centrality dependence for higher-order flow coefficients can also be observed. In the most central collision area, similar magnitudes due to the dominance of nucleon fluctuations in the overlap region can be observed, whereas in semi-peripheral collisions there is a dominance of the almond shape of the overlap region.

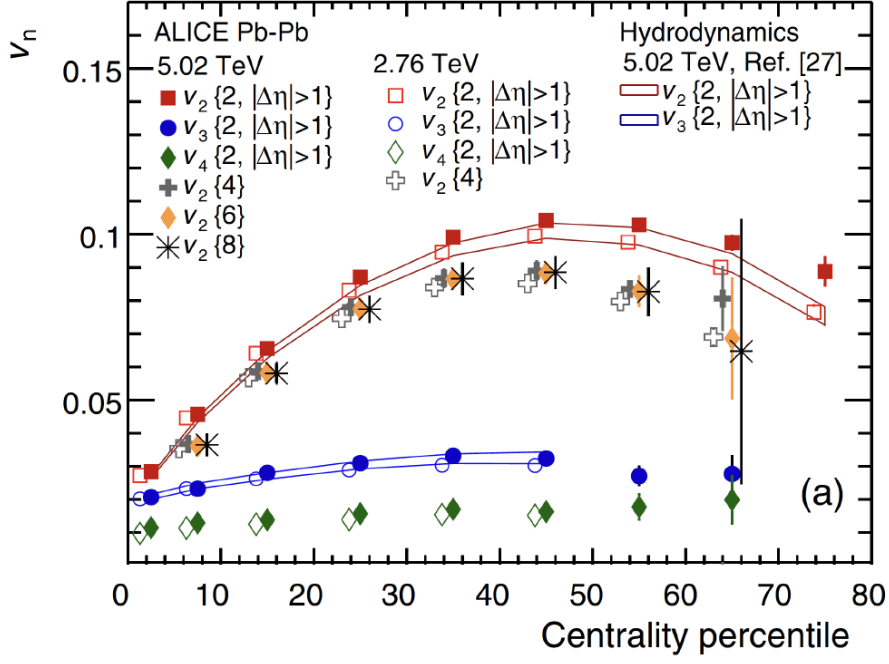


Figure 3.15: Higher-order flow coefficients centrality dependence [44].

From the point of event-event fluctuations it is therefore of interest to look at very central collisions. As shown in Figure 3.16 by the measurement of CMS collaboration [45] the results show a dominance of higher-order harmonics as the eccentricities are mostly driven by event-by-event participant fluctuations (see Figure 3.16).

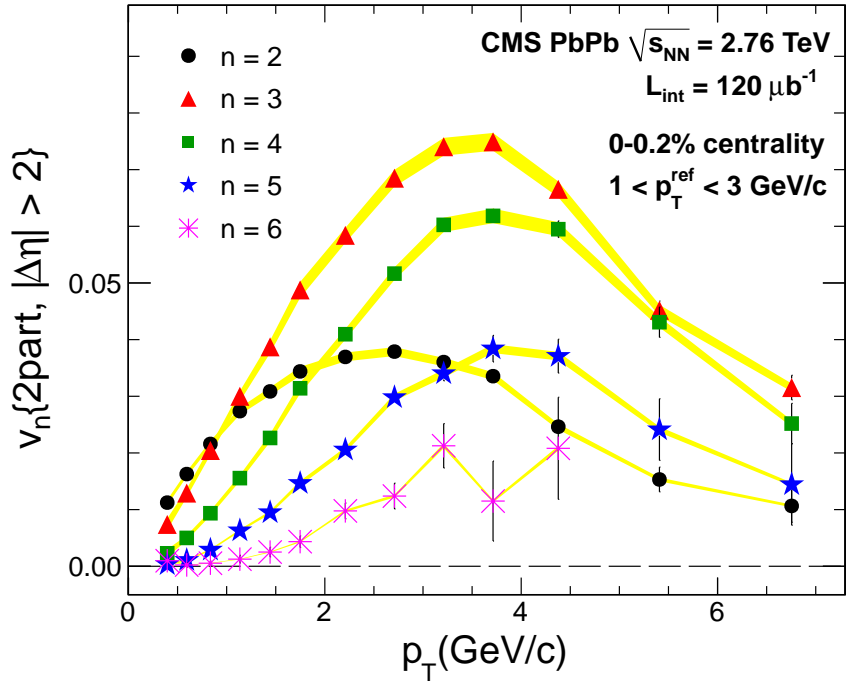


Figure 3.16: Higher-order flow coefficients p_T dependence in ultra central collisions [45].

3.2.3 Flow in Small Systems

The azimuthal anisotropies have also been observed at the RHIC [46, 47, 48, 49, 50, 51] and the LHC [52, 53, 54, 55, 56, 57] in small-sized systems such as p+A, d+A, and $^3\text{He}+A$ collisions. This topic is of great importance to current research and has such complexity that for the purposes of this thesis, it is discussed in a rather simplified manner. Many of the collective behavior characteristics seen in collisions of heavy nuclei and ascribed to the perfect liquid nature of QGP were seen in these smaller systems. According to numerical simulations, hydrodynamics is still relevant even for systems with sizes on the order of the inverse temperature [46]. It is unknown how sub-nucleonic fluctuations, which are insignificant for larger-sized systems, affect the initial geometry in small-sized systems, where they may be caused by an unevenly distributed gluon field inside the nucleon. Models indicate that sub-nucleonic fluctuations have a significant impact on the system's dependence on eccentricity. This implies that measurements of the system dependence of $v_{2,3}(p_T)$ can shed light on the structure of the nucleon and offer a unique limit on the role of such fluctuation in small-scale systems. Due to the brief lifetime of the generated medium, the anisotropy may also result from non-hydrodynamic modes and/or large hydrodynamic gradient expansion correction. In central He+Au, d+Au, and p+Au collisions, measurements of the elliptic and triangular azimuthal anisotropies reveal the effect of sub-nucleonic fluctuations in the small-sized systems.

To discuss a concrete example, in Figure 3.18 the latest results from STAR on flow in small systems [46] are compared to two hydrodynamic model simulations, SONIC and IP-Glasma+MUSIC. The SONIC model uses initial eccentricity from the nucleon Glauber model without sub-nucleonic fluctuations, and it exhibits reasonable agreement with the most recent measurements for $v_2(p_T)$ in He+Au and d+Au and for $v_3(p_T)$ in He+Au, but it significantly underestimates $v_3(p_T)$ in d+Au

and p+Au. The substantially lower eccentricity values used in the calculations may be the cause for the underprediction. The IP-Glasma+MUSIC model contains sub-nucleonic fluctuating initial states, three-dimensional hydrodynamic evolution, and a model for evolution in the hadronic phase. After being tuned to explain the data for large-sized systems, it automatically extrapolates to small-sized systems. These estimates, in contrast to the SONIC model, overestimate the $v_2(p_T)$ but exhibit strong agreement with the $v_3(p_T)$ data for all three systems. An overestimation of the system-dependent eccentricity ε_2 values used in the calculations may be the cause of this overprediction. Both models are unable to describe $v_2(p_T)$ and $v_3(p_T)$ simultaneously. The observations reveal that, in contrast to d+Au and He+Au collisions, where the size of v_3 is system-independent, the magnitude of v_2 in p+Au collisions is smaller. The data support the idea that sub-nucleonic eccentricity variations have a major impact. It shows that further model developments are needed for in-depth descriptions of azimuthal anisotropy in small-sized systems, particularly for the theoretical parameters that control the sub-nucleonic fluctuations.

There are also detailed studies of collectivity of small systems on the LHC, such as in Figure 3.17. The figure shows a comparison of elliptic, triangular and quadrangular flow in small and large collision systems with respect to multiplicity N_{ch} . As expected, large systems demonstrate dependence on the multiplicity for large and intermediate multiplicities and they appear independent in low multiplicities. On the other hand, small systems show no or only small change throughout the whole multiplicity range. However, no matter the system size, the flow coefficient ordering remains the same.

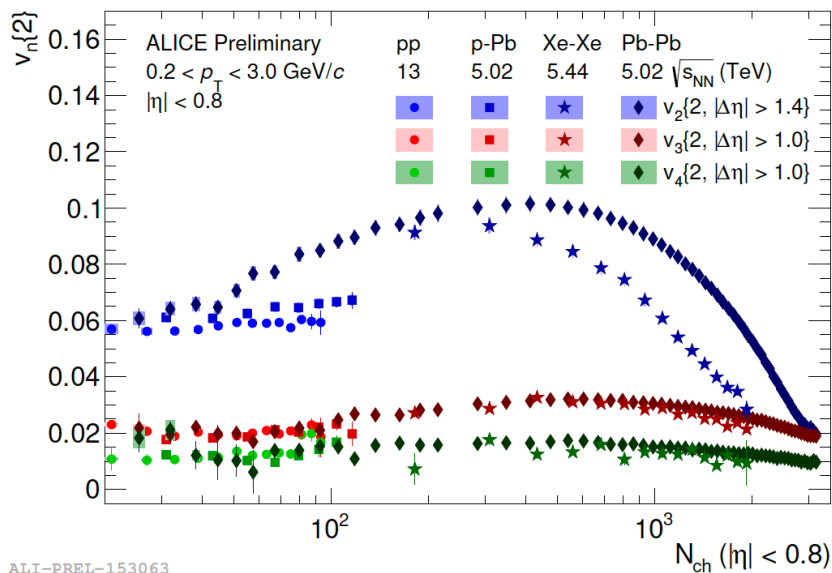


Figure 3.17: Multiplicity dependence of v_2 , v_3 and v_4 measured using the two-particle cumulant method with a $|\eta|$ gap in small and large collision systems [58].

Moreover, measurements in small systems are more prone to contamination from non-flow effects. Their understanding and analysis methods for suppressing their effect are important for drawing correct physics conclusions. These will be discussed in the following text.

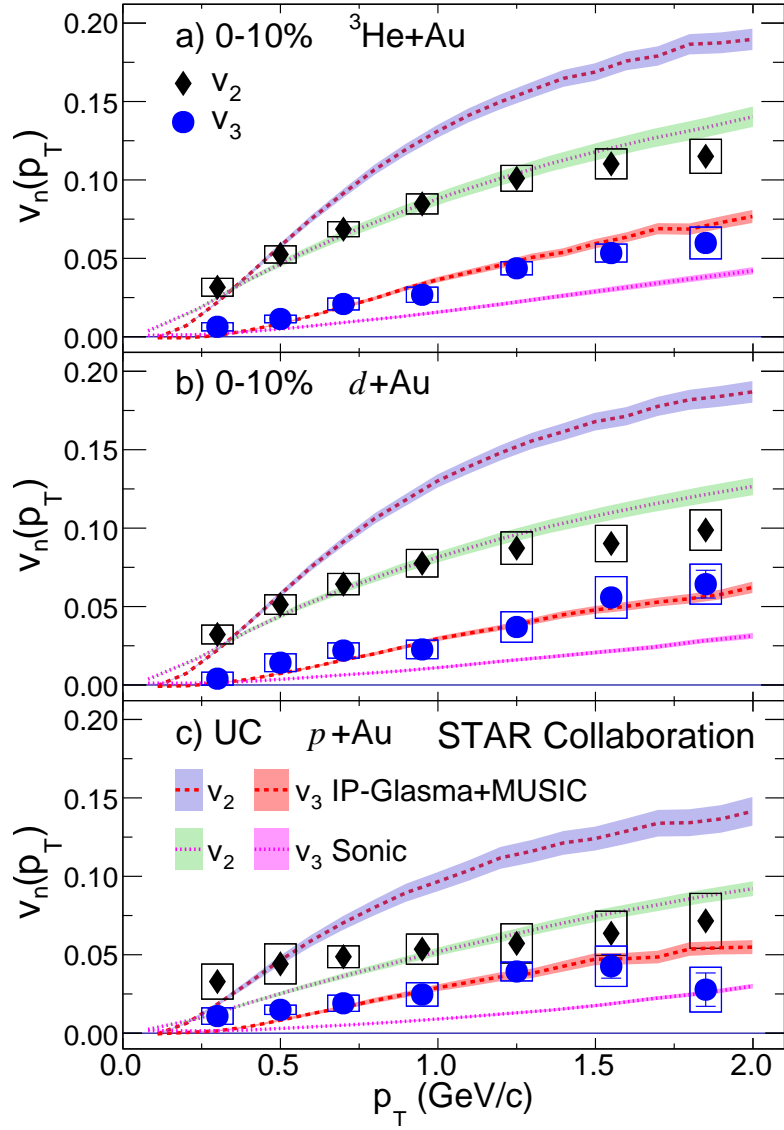


Figure 3.18: Flow coefficient measurements in smaller systems with hydrodynamic predictions [46].

3.2.4 Non-flow Effects

Non-flow effects are correlations which increase the magnitude of the observed anisotropy in the particle production, but do not originate from collective. These correlations are caused by effects like jets, resonance decays or the fact that particles are not correlated to the common symmetry plane. These non-flow effects affect every measurement and have to be accounted for. In Figure 3.19 is shown an example from measurement done by PHENIX collaboration [59]. The figure shows flow results obtained from two particle correlations. In one case ($v_2\{2\}$) there is no restriction on proximity of the two particles used for the calculation while in the second case ($v_2\{2, |\Delta\eta| > 2\}$) it is required that there is a gap in between them of at least 2 in pseudorapidity. It clearly demonstrates that there is a large difference of up to 40% for large centralities caused by the non-flow effects. The methods of dealing with non-flow effects, such as pseudorapidity gap are useful, especially for peripheral collisions or for small systems where the non-flow is not as suppressed as in the central collisions of large nuclei.

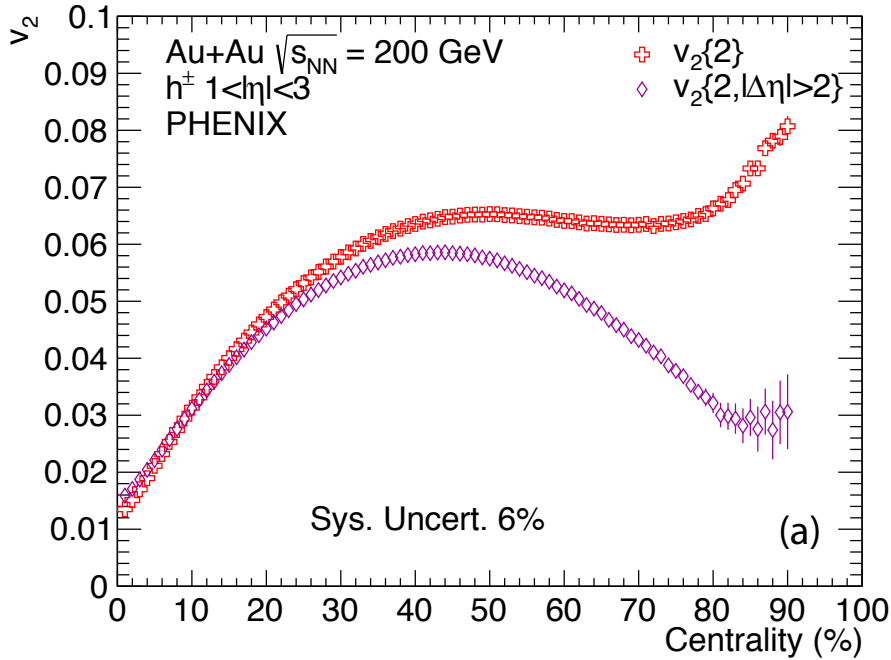


Figure 3.19: The difference in the elliptic flow with non-flow effects (red) and without non-flow effects (magenta) [59].

3.2.5 Experimental Methods

Event plane method

This method is useful for measurements at high energies. To estimate the v_n coefficients, by definition, one would need to measure the reaction plane, but this plane cannot be directly measured. However it is possible to determine the event plane angle Ψ_n for each harmonic coefficient of the flow distribution. This is called the *event-plane method*. It uses the so called event flow vector Q_n which is a vector in

the transverse plane defined as follows [34]:

$$\begin{aligned} Q_{n,x} &= \sum_i w_i \cos(n\phi_i) = \mathbf{Q}_n \cos(n\Psi_n), \\ Q_{n,y} &= \sum_i w_i \sin(n\phi_i) = \mathbf{Q}_n \sin(n\Psi_n), \end{aligned} \quad (3.2)$$

where the sum goes over all particles. ϕ_i and w_i are the laboratory azimuthal angle and weight of the i -th particle. The weight is chosen to approximate $v_n(p_T, y)$ and optimize the resolution of the reaction plane and is different for odd and even harmonics. The reflection symmetry of symmetric collisions causes the difference. The particles in the backward hemisphere of the CMS should be the same as in the forward hemisphere for the azimuthal angles shifted by π [60], thus for odd harmonics, we get $w_i(-y) = -w_i(y)$. The weight is often chosen as the transverse momentum of the particles, as the v_n grows linearly with p_T . The event plane angle is calculated as [60]

$$\Psi_n = \left(\tan^{-1} \frac{\sum_i w_i \sin(n\phi_i)}{\sum_i w_i \cos(n\phi_i)} \right) / n = \tan^{-1} \left(\frac{Q_{n,y}}{Q_{n,x}} \right) / n. \quad (3.3)$$

The measured angle is sensitive to the finite multiplicity (finite number of detected particles) and this needs to be accounted for by event plane resolution. This resolution is given for each harmonic by [34]

$$\mathcal{R}_n = \langle \cos[n(\Psi_n - \Psi_{\text{RP}})] \rangle, \quad (3.4)$$

averaging over a large event sample. The flow coefficients are defined by the observed flow coefficient divided by the resolution. Because the correction is always less than one (due to cosine in the definition), it will increase the final coefficient. Even though the determination of the resolution for the full event may seem more straightforward, it is often not preferred. It is convenient to divide the event into sub-events, that are naturally correlated as they are both correlated with the reaction plane, with the same number of particles. The division is done randomly, by pseudorapidity, by charge, or by an arbitrary combination of these. To calculate the resolution, one uses the resolution parameter χ defined as a flow coefficient multiplied by \sqrt{N} , where N is the number of particles [34]. The reaction plane resolution is then defined as

$$\mathcal{R}_k(\chi) = \sqrt{\pi}/2 \chi \exp(-\chi^2/2) (I_{(k-1)/2}(\chi^2/2) + I_{(k+1)/2}(\chi^2/2)), \quad (3.5)$$

where I is the modified Bessel function. The dependence of \mathcal{R}_k on χ is shown in Figure 3.20.

To determine the resolution of subevents A and B one can use their correlation and take simply the square root of that [34]:

$$\mathcal{R}_{n,\text{sub}} = \sqrt{\langle \cos[n(\Psi_n^A - \Psi_n^B)] \rangle} \quad (3.6)$$

The resolution of the full event can be obtained from the resolution parameters of the subevents by $\mathcal{R}_{\text{full}} = \mathcal{R}(\sqrt{2}\chi_{\text{sub}})$ [34].

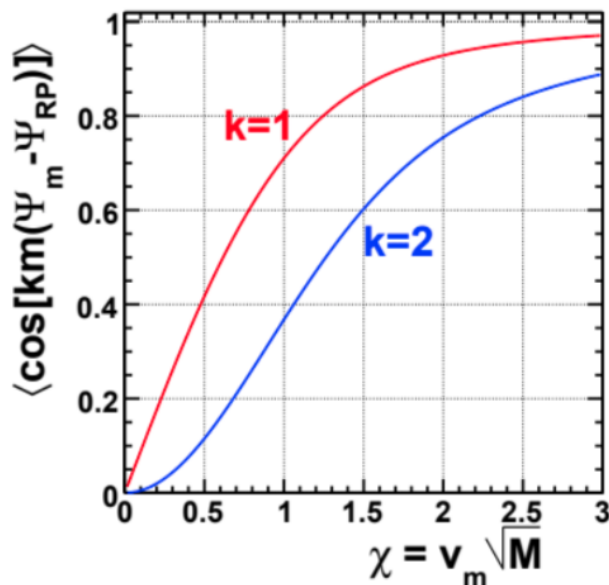


Figure 3.20: The event plane resolution as a function of χ . The harmonic number of the correlation n is an integer k times the harmonic number m of the event plane [34].

It is also important to note that the resolution drops when the event plane is determined from the same harmonic as v_n . Another correction is crucial due to the imperfection of the detector. Unfortunately, the particles are not detected with azimuthally isotropic efficiency due to either limited acceptance of the detector or/and detector non-uniformity of detector response. There are several methods used to remove this effect, such as recentering, phi weighting or shifting. The recentering method utilizes the Q-vectors of each event that are subtracted from the averaged Q-vector. This method is not useful for higher harmonics. The phi weighting method, which is very common, uses the particle distribution to determine the acceptance, this method uses the inverse of the azimuthal distribution of the particles for all events as weights in the calculation of the event planes. The advantage of this method is a zero average Q-vector and the possibility to account for areas of dead parts in the detector. [60].

Two and many-particle correlations

The many-particle correlation method's essence is the comparison of the two-particle azimuthal distribution to that expected from the anisotropic flow [34]:

$$\frac{dN^{pairs}}{d\Delta\phi} \propto (1 + \sum_{n=1}^{\infty} 2v_n^2 \cos(n\Delta\phi)) \quad (3.7)$$

where all pairs of particles in a given momentum region are correlated, no event plane is used.

The two-particle cumulant method differs from the many-particle approach only in the fact that instead of the fit to the two-particle distributions, it calculates the coefficient directly as [34]

$$v_n\{2\}^2 = \langle \cos[n(\phi_1 - \phi_2)] \rangle = \langle u_{n,1} u_{n,2}^* \rangle \quad (3.8)$$

for all pairs of particles, where u_n is the particles' unit flow vector. The difference in the differential flow obtained from the two-particle cumulant method and the event plane method lies in using the length of the flow vector as weight, the resulting statistical errors are slightly smaller in the cumulant method. The estimates of flow coefficients have a sizable advantage of reducing non-flow correlations (see Figure 3.19), which are mostly created by few-particle correlations. Higher order cumulants are multi-particle correlations where the contributions of lower order multiplets have been subtracted, however, the statistical errors for this method are larger than with the event plane method. Another disadvantage is that v_n^4 can sometimes be negative, depending on the nature of flow fluctuations [34]. Amongst the advantages of the multi-particle cumulant technique is a possibility of a consistent treatment of acceptance effects and the inclusion of mixed harmonics. An important example of the latter is the three-particle correlation, which was successfully used at RHIC to suppress non-flow in the study of v_1 [61] and v_4 [62].

η -subevent method

Another way of reducing non-flow contributions from non-flow effects is the η -subevent method. This is achieved by splitting the pseudorapidity acceptance of the detector into two or more regions separated by some space (η -gap). This method is similar to the event plane method, except for the fact that the event flow vector is defined for each particle based on particles measured in the opposite hemisphere in pseudorapidity [63].

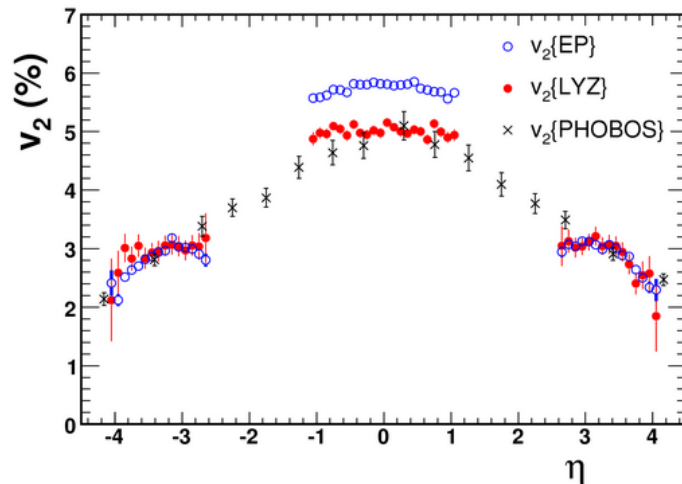


Figure 3.21: Pseudorapidity dependence of elliptic flow for $\sqrt{s_{NN}} = 200$ GeV Au+Au from the event plane method (STAR), the LYZ method (STAR), and using an η gap (PHOBOS) [63].

q-distributions, Lee-Yang Zeros, Bessel and Fourier Transforms

As mentioned above, the Q-vector measurements are useful for high-energy studies, where the multiplicity M plays a great role and affects the magnitude of the Q-

vector. This dependence is not favorable and can be removed by defining the reduced flow vector q_n defined as [34]

$$q_n = Q_n/\sqrt{M}. \quad (3.9)$$

This method is called the q-distributions method and, as opposed to the Q-vector method, it focuses on the length distribution of the q-vector. As expected, the length distribution is influenced by the multiplicity that shifts it by $v_n^2 M$ and it is widened by fluctuations and non-flow correlations.

To subtract the non-flow effects, the Fourier and Bessel transforms [64] or the Lee-Young Zeros methods [63] can be used. The Fourier and Bessel transforms are useful to demonstrate the separation of non-flow effects using the collectivity of flow. It is only applicable in the limit of $\sqrt{M} \gg 1$. Furthermore, in this limit, the distribution of the flow vector is expected to be Gaussian (due to the Central Limit Theorem). This means the fitting distributions are not sensitive to non-flow correlations [34]. The Lee-Yang Zeros method is more versatile and is able to subtract non-flow effects to all orders [63]. It creates a generating function using the Q-vector that is calculated with designated weights to eliminate autocorrelations and non-flow effects. Afterwards, it tries to determine the first minimum. Unfortunately, this method requires much more computer time and a good signal-to-noise ratio.

Chapter 4

CBM Experiment at FAIR

This chapter focuses on the Facility for Antiproton and Ion Research and in particular, one of its experiments, the CBM experiment.

4.1 The Facility for Antiproton and Ion Research

Currently, the Facility for Antiproton and Ion Research (FAIR) is under construction at Darmstadt, Germany. Upon its completion, FAIR will be one of the world's most advanced accelerator facilities, having the unique ability to provide accelerated beams of any chemical elements, as well as antiprotons, at unprecedented rate and intensity.

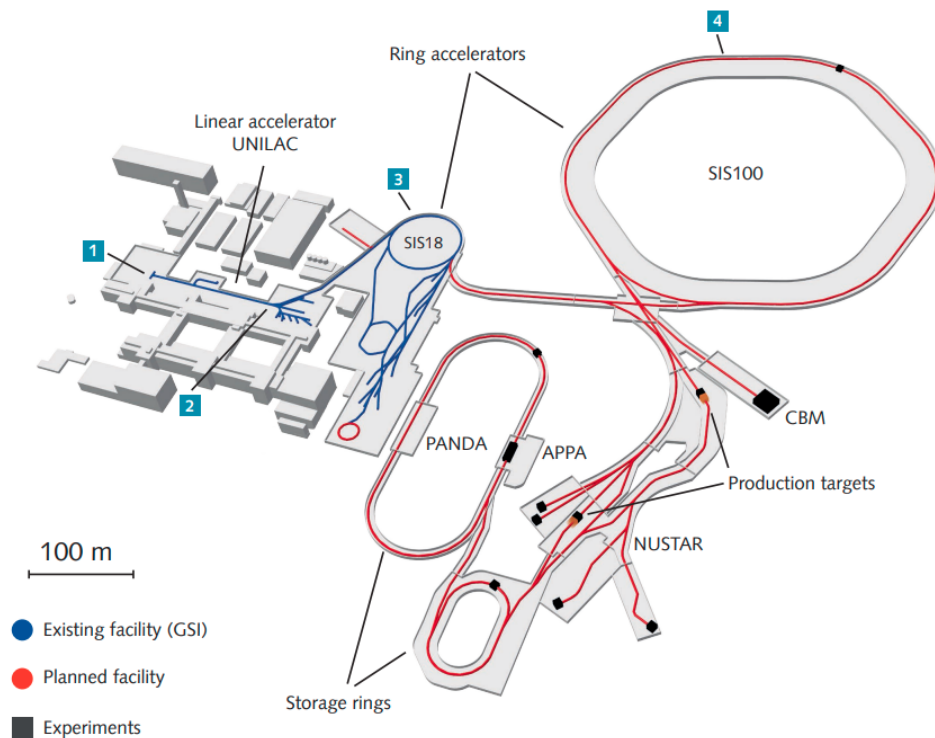


Figure 4.1: The Facility for Antiproton and Ion Research [65].

The layout of FAIR is shown in Figure 4.1. Its most crucial component is the SIS100 ring accelerator with a circumference of 1,100 meters. The SIS100 is connected to a system of additional storage rings and experimental stations with the existing facility of the GSI Helmholtzzentrum für Schwerionenforschung serving as the injector for the FAIR facility. The accelerating process occurs as follows [65]:

1. At 0 s, atoms are torn from the material using a high-voltage discharge. Moreover, they are stripped from some of their electrons, making them ions. These ions are then steered by an electric field towards the UNILAC linear accelerator.
2. At 0.00001 s, the ions are accelerated in the UNILAC. After traversing an array of copper cylinders, they can reach up to 47,000 km/s.
3. At 0.7 s, the ions have flown through the SIS18, the 216-meter long circular accelerator, several hundred thousand times, at which point they reach about 270,000 km/s or 90 % of the speed of light.
4. At 6.7 s, the larger dimensions and stronger superconducting magnets of the SIS100 allow the ions to be accelerated even further up to 285,000 km/s, or 95 % of the speed of light. After reaching this speed and traveling through over one million kilometers of accelerator beamlines, the ions are steered towards the designated experimental stations or stored in the storage rings.

There are four experimental projects to be operated at the FAIR facility, namely CBM, NUSTAR, APPA and PANDA.

The NUSTAR Experiment

The NUSTAR (Nuclear Structure, Astrophysics and Reactions) collaboration [66] is devoted to studying exotic nuclei which are typically produced in stars and stellar explosions. At FAIR, these exotic nuclei will be created in a fixed target experiment, enabling their further research thanks to the Super-FRS or the Superconducting Fragment Separator. The Super-FRS uses several-ton superconducting magnets to sort the exotic nuclei according to their mass and charge. This will allow scientists to study the exact nuclei they want to study. The separated nuclei will be kept at constant speed in storage rings, allowing high precision in measurements of such properties as the lifetime, shape or internal structure of the exotic nuclei. These properties are key to understanding the creation of elements inside stars.

The PANDA Experiment

The PANDA (Antiproton Annihilation at Darmstadt) experiment [67] will focus on studying the products of proton-antiproton collisions. When a particle makes contact with its antiparticle, a process called annihilation results in a massive release of energy from which various other particles are created. These products might also include some theorized combinations of quarks and gluons, such as tetraquarks (particles consisting of two quarks and two antiquarks) or glueballs (particles consisting

solely of gluons). The aim of PANDA is to study these particles in order to improve our understanding of the strong interaction.

4.2 The APPA Experiment

The APPA (Atomic Physics, Plasma and Applications) [68] is a collective name for several projects with similar experimental setups and methods. Their research will range from the effect of ion beams on living tissue and solid materials, applications of plasma physics in engineering to further exploration of existing physical phenomena such as Quantum Electrodynamics or the Special Theory of Relativity.

4.3 The CBM Experiment

The CBM (Compressed Baryonic Matter) experiment will focus on the exploration of dense nuclear matter and its equation of state. In contrast with other collider facilities such as CERN or RHIC, which collide nuclei at extremely high energies and nearly zero baryon densities, CBM will be focused on intermediate temperatures and high baryon densities in order to study different regions of the phase diagram of nuclear matter and search for the critical point, and consequently, the first order phase transition. All of the specifications of CBM and its subsystems stated hereinafter are taken from [69, 70, 71, 72, 73, 74, 75, 76].

For this reason, the detector's geometry has been optimized; unlike experiments at RHIC and CERN, the CBM detector investigations will be of the fixed-target type rather than the collider type. One of CBM's distinctive qualities will be its high-rate data acquisition system (DAQ) that can capture up to 10^7 interactions per second. Because of this trait, CBM will be sensitive to extremely uncommon heavy-ion collision probes (e.g. multistrange hyperons).

Continuous readout poses another difficult problem since, unlike earlier experiments, there is no trigger system to initiate readout, and the data will be continuously read out, preprocessed online, and then saved for offline analysis. The CBM detectors are made to handle events at 10 MHz, which corresponds to 10^9 ions per second of beam intensity and a target 1% total cross section (only 1% of beam particles interact in the target). Assuming a 40 kB event size (corresponding to an Au+Au collision) and an archiving rate of 1 GB/s, the maximum frequency that can be allowed by data acquisition is 25 kHz. Therefore, a data-reducing algorithm that can reduce the volume of the data stream by more than 400 times is required. This is achieved by rapid online event reconstruction using CPU and GPU farms. On the basis of parallel track-finding algorithms that implement, for instance, the Kalman Filter Method, track reconstruction is done. Tracking will be employed in events with open charm particles (such as D mesons) to detect secondary vertexes, and this data will subsequently be used as an online trigger. The Green IT Cube computing center was constructed with the intention of processing and storing data.

In Figure 4.2, the CBM experiment detector layout is shown. There are in fact two different experimental setups planned for CBM, one including the RICH detector for electron measurements and one with the MUCH detector for muon measurements.

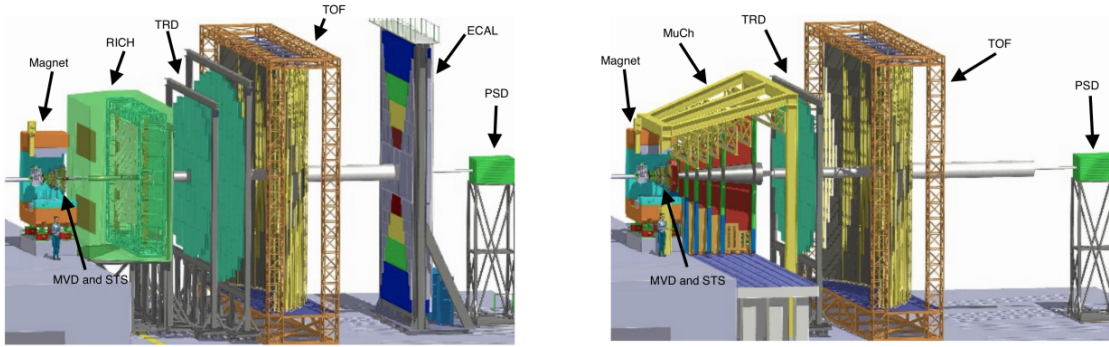


Figure 4.2: The CBM detector layout with (left) the particle identification detector RICH, and (right) the muon identification detector MUCH [70].

The following subsections focus on describing the properties of each one of the CBM’s detector subsystems.

Micro-Vertex Detector

The main goal of the micro-vertex detector (MVD) [71] is to detect dileptons and determine whether or not they originate from the primary vertex. Another objective is to reconstruct short-lived particles, such as D mesons, using decay topologies. Because the D meson’s lifespan is very short, MVD must be precise in order to identify secondary vertexes. High radiation tolerance and a small material budget are also required in order to minimize rescatterings. Monolithic Active Pixel Sensors (MAPS) with pixel sizes of around 18 - 20 μm can be used to attain these conditions. These MAPS are positioned in four layers 5, 10, 15 and 20 cm downstream of the target. The pixel resolution ranges from 3.5 to 6 μm , while the secondary vertex resolution (on the beam axis) is 50 to 100 μm . Depending on the stations’ size, the detector’s overall thickness is between 300 and 500 μm silicon equivalent for sensors and support structures. The expected time resolution is less than 30 ns.

Silicon Tracking System

The silicon tracking system (STS) [72] is designed to determine the momentum of particles and provide track reconstruction. The STS comprises of up to 8 tracking layers of silicon detectors which are located downstream of the target at 30 - 100 cm inside the magnetic dipole field. Momentum resolution is required to be at least $\Delta p/p = 1\%$. The STS tracking concept is based on silicon microstrip detectors mounted on thin mechanical supports in the shape of ladders. The sensors will be read out at the stations’ periphery, where cooling lines and other infrastructure may be installed, using multi-line micro-cables with fast electronics. The double-sided micro-strip sensors will feature a stereo angle of 0/7.5 degrees, a strip pitch of 60 μm , strip lengths ranging from 20 to 60 mm, and a silicon thickness of 300 μm . The micro-cables will be constructed from numerous 10 μm thick polyimide-aluminium layers stacked together.

Ring Imaging Cherenkov Radiation

The task of the RICH detector [73] is electron identification and suppression of pions with momentum below 8-10 GeV/c. A gaseous RICH detector with focusing mirror components and a photodetector will be used to accomplish this. The radiator gas will be CO₂, which has a pion threshold for Cherenkov radiation of 4.65 GeV/c. The detector will be positioned 1.6 meters downstream of the target, behind the dipole magnet. It will include two arrays of mirrors and photodetector planes, a 1.7 m long gas radiator, with an overall length of around 2 m. Two horizontal arrays of spherical glass mirrors, each measuring 4 by 1.5 meters apiece, are placed on the mirror plane. The 72 mirror tiles feature an Al+MgF₂ reflecting coating, a 3 m radius of curvature, and a 6 mm thickness. Two 20.6 m² photodetector planes positioned behind the CBM dipole magnet and protected by the magnet yokes will have rings projected upon them. In-beam testing with a RICH prototype of actual length shows that 22 photons are on average recorded per electron ring. Due to the substantial material budget in front of the RICH detector, central Au+Au collisions at 25 AGeV beam energy indicate the order of 100 rings. However, models predict that a pion suppression of the order of 500 will be accomplished because of the high granularity (about 55000 channels) and high amount of photons per ring.

Muon Chamber System

Finding low-momentum muons in an environment with high particle density is a challenge for experimental muon measurements in heavy-ion collisions at FAIR energy. The idea behind CBM is to track the particles using a hadron absorber device and identify muons based on their momentum. To implement this idea, the hadron absorber is divided into many layers, and triplets of tracking detector planes are inserted into the spaces between the layers of the absorber. The muon chamber system (MUCH) [74] is positioned downstream of the Silicon Tracking System (STS) which determines the particle momentum. The MUCH system must be as small as possible in order to minimize meson decays into muons. The MUCH's design comprises six layers of hadron absorbers (iron plates with thicknesses of 20, 20, 20, 30, 35, and 100 cm), as well as 15 – 18 gaseous tracking chambers arranged in triplets behind each iron slab.

Transition Radiation Detector

The TRD subsystem [75] consists of three stations each having three detector layers for particle tracking and for the identification of electrons and positrons with momentum $p > 1.5$ GeV/c ($\gamma > 1000$). The detector stations are situated at 5, 7.2, and 9.5 m downstream of the target, with a total active detector area of approximately 600 m². Particle rates in the order of 100 kHz/cm² are anticipated for 10 MHz minimum bias Au+Au collisions at 25 AGeV at low forward angles and a distance of 5 m from the target. Particle densities of roughly 0.05/cm² are expected in a central collision. The minimal size of a single cell should then be roughly 1 cm² in order to keep occupancy below 5%. The rectangular pads used for the TRD detector readout will provide a resolution of 300–500 mm across and 3–30 mm along the pad. A 90-degree rotation of the transition radiation layer occurs in every other layer.

Time of Flight Detector

The TOF detector's [76] objective is to identify hadrons by velocity measurements. It consists of an array of resistive plate chambers (RPC) which, in principle, are gas chambers with two planar surfaces at high voltage. The TOF detector covers an active area of approximately 120 m^2 and is located about 6 m downstream of the target. A time resolution of around 80 ps is needed. The innermost component of the detector must operate at rates as high as 20 kHz/cm^2 for 10 MHz minimum bias Au+Au collisions. Low-resistivity glass-based prototype RPCs have been put through testing with a time resolution of roughly 40 ps at 20 kHz/cm^2 . For central Au+Au collisions at 25 AGeV, the pad size for minor deflection angles is around 5 cm^2 , which corresponds to an occupancy of under 5%.

Projectile Spectator Detector

The task of the PSD [70], a compensating lead-scintillator calorimeter-type detector [70], is to measure the energy distribution of the projectile nuclei fragments (spectators) as well as forward-going particles produced close to the beam rapidity. The specifics of the PSD are further described in detail in the following section.

4.4 Projectile Spectator Detector

With the exceptional accuracy made possible by the high luminosity beams of FAIR, the CBM experiment intends to carry out a systematic assessment of production yields, phase-space distributions, correlations, and fluctuation observables for numerous particle species created in nuclear collisions. The primary goal of the PSD is to obtain an experimental measurement of the centrality and orientation of the symmetry plane of heavy ion collisions. For many physics processes, a precise event-by-event estimation of these fundamental observables is essential. A crucial observable that reveals details about the fireball's composition and reaction dynamics is the collective flow of particles created by a collision, which is defined with respect to the reaction plane that is spanned by the collision's impact parameter and the beam direction. The orientation of the impact parameter is reflected by the spectators, which are flying out in the impact parameter's direction. Therefore, measuring spectator location and energy at a specific distance downstream of the target is the most straightforward way to determine the reaction plane. The PSD must thus have an adequate energy resolution as well as a modular structure with sufficient azimuthal segmentation in order to reliably determine the position of the spectators. The PSD's main design criteria include forward rapidity coverage, appropriate energy resolution to allow for precise collision centrality estimation, in addition to granularity in the plane transverse to the beam directions, which is required for the reconstruction of the collision symmetry plane. These requirements can be satisfied by a compensating hadron calorimeter. The calorimeter's energy resolution is enhanced by the compensation condition, which equalized the calorimeter's reaction to the electromagnetic and hadronic components. This removes one of the major sources of energy fluctuations and hence improves precision. Amongst other advantages of compensating calorimeters are linearity and Gaussian shape signal of

the detector response. It was shown that the compensating condition depends on the relative absorber/active thickness ratio. Compensating condition is fulfilled for Pb/Scintillator sampling ratio equal to 4.

4.4.1 PSD Structure and Geometry

The PSD's suggested design covers a sizable transverse region around the beam point position, allowing the majority of projectile spectator fragments to discharge the majority of their energy in the PSD. The fragments' deflection by the CBM dipole magnet's magnetic field is taken into account by the PSD's elongated transverse geometry in the horizontal direction. The PSD is made up of 44 separate modules, each with a transverse size of $20 \times 20 \text{ cm}^2$ (see Figure 4.3). Each module

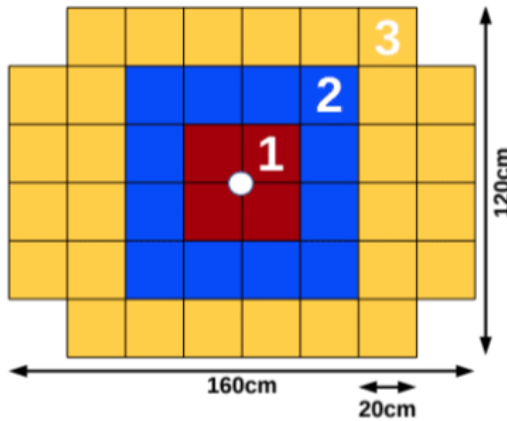


Figure 4.3: The structure of the PSD and its segmentation into three concentric sections. [70].

consists of 60 lead-scintillator sandwiches, each made up of lead and scintillator tiles that are 16 mm thick and 4 mm thick respectively. The total interaction length is about $6 \lambda_i$. A single photon detector reads out every six successive layers of the scintillator using the WLS fibers. The planned design of the PSD module and the light readout is shown in Figure 4.4. The longitudinal segmentation of the PSD modules is provided by the 10 sections with the individual light readout. Instead of PMTs, Micro-Pixel Avalanche Photodiodes (MAPDs) read out the light from the WLS fibers. The module's uniform light collection is achieved by the longitudinal segmentation. A possibility to enhance the energy resolution based on observations of the longitudinal hadron shower profile with the off-line compensating method is also allowed by the segmentation of the calorimeter. These photodiodes have exceptional properties, such as good photon detection efficiency, gain, low cost, compactness and simplicity of operation. The radiation exposure has minimal impact on the PSD calorimeter. Due to the modular construction and longitudinal segmentation, the transverse and longitudinal uniformity of the PSD light collection is not compromised.

The geometry of the CBM subsystems used for the PSD performance study is depicted in Figure 4.5. Each individual module must be positioned at the beam axis

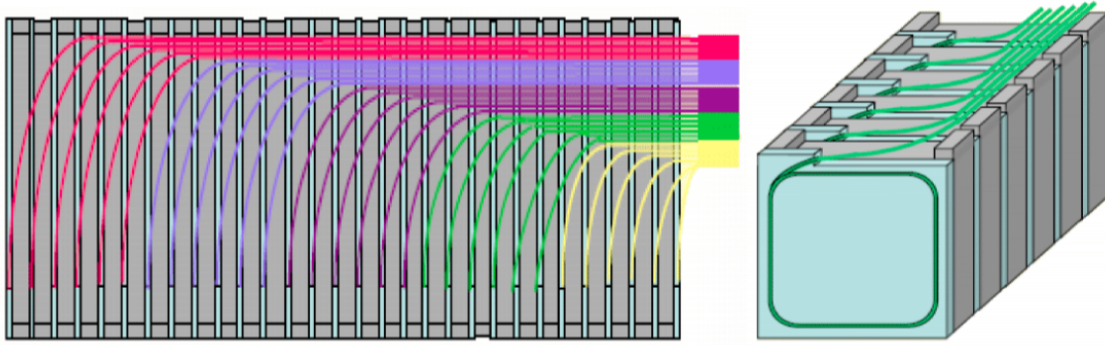


Figure 4.4: Design of the PSD module and light readout from scintillator tiles in PSD module. Left-front view, right- top view (only half-length of the module is shown). Fibers from each consecutive 6 tiles are collected together and read out by a single MAPD [70].

for the PSD calibration using beam particles (protons and muons). The calorimeter must thus be moved with millimeter-level precision in the transverse directions using a movable platform. It is pleasant to note that such a platform has been already successfully delivered to GSI by Faculty of Mechanical Engineering of the Czech Technical University in Prague. When moving the detector, the calibration procedure calls for disconnecting the vacuum pipe from the beam pipe within the calorimeter. The dipole magnet's field, which runs along the vertical axis in the laboratory frame and has a full magnetic field integral of around 1 Tm, deflects the ion beam horizontally. For each collision energy, magnetic field strength, and detector distance to the target, the PSD is moved by x_{shift} so that the beam always passes the PSD via its beam hole. According to the graphic, the PSD modules are divided into three classes (subevents) for the performance studies. The subevents enable centrality and reaction plane determination using the PSD as a stand-alone detector. The three segments are referred to as PSD1, PSD2, PSD3 (illustrated in 4.3 in red, blue and yellow respectively), and PSD-full when all modules are employed.

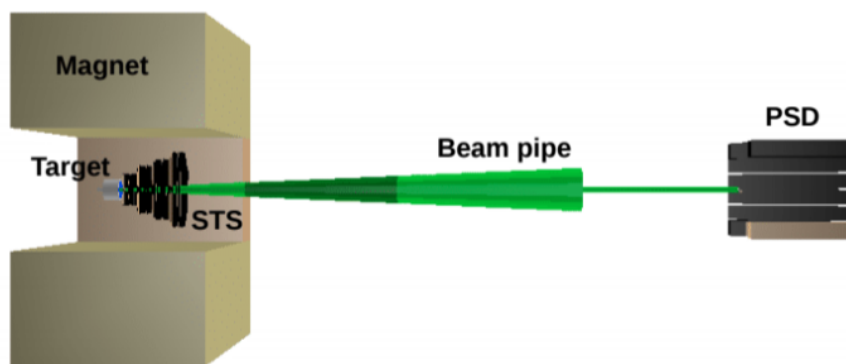


Figure 4.5: CBM detector geometry used for the PSD performance study [70].

4.4.2 Centrality Determination

The PSD has an impact parameter resolution that, depending on the collision energy, is equivalent to the CBM silicon tracking system's (STS). Thus, in the CBM

experiment the PSD offers an independent method of centrality determination from spectator multiplicity. The PSD provides for centrality determination in small centrality classes with a width of at least 5% and contributes to improving the overall centrality determination in the centrality range of 0 - 40% when used in combination with the STS. The PSD uses an independent way of centrality determination using the multiplicity of the spectators. The independent procedure is useful for studies of event-by-event fluctuations at midrapidity. In the case of small energy deposition in the PSD, the events are marked as the most central events. In comparison, a large number of spectators depositing a large amount of energy in the PSD correspond to peripheral events. The PSD has a hole in its structure which causes a loss of fragments of about 40% most peripheral events. This causes a decorrelation between the energy measured by the PSD and geometrical quantities. To account for these events, a cut $M_{\text{trk}}/M_{\text{trk}}^{\text{max}} > 0.6 - 0.8E_{\text{PSD}}/E_{\text{PSD}}^{\text{max}}$ was implemented [77]. Results for the correlation before and after this cut are shown in Figure 4.6 with visible improvement after the cut. In addition, the PSD can be used for centrality determination as a standalone detector and with the STS detector, the PSD improves the centrality determination in the 0-40% centrality range with the centrality classes with a width of at least 5%.

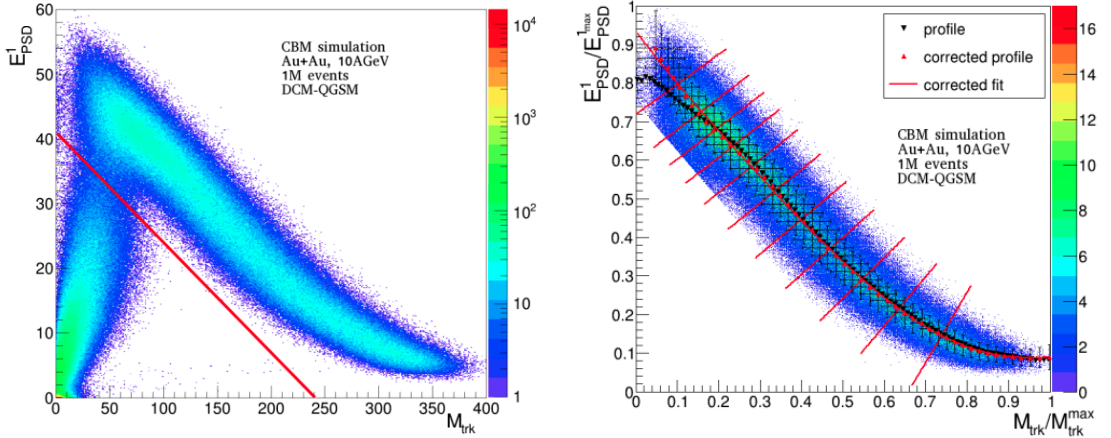


Figure 4.6: Left: The correlation between the energy deposited in the central PSD modules (E_{PSD}^1) and the track multiplicity M_{trk} . Right: The correlation between the energy deposited in the central modules of the PSD (PSD1) and track multiplicity with a cut $M_{\text{trk}}/M_{\text{trk}}^{\text{max}} > 0.6 - 0.8E_{\text{PSD}}/E_{\text{PSD}}^{\text{max}}$ [77].

4.4.3 Reaction Plane Reconstruction

The direction of the impact parameter is unknown experimentally, much like the impact parameter's magnitude. The azimuthal asymmetry of particle production in the transverse plane to the beam direction is frequently used to assess the orientation of the reaction plane. Spectators are deflected during the collision because of the momentum transfer between participants and spectators. The spectator deflection direction is related to the direction of the impact parameter (or reaction plane) for non-central collisions because the initial energy density's asymmetry in the transverse plane is aligned in that direction. An estimation of the orientation of the reaction plane may be made using the plane that is spanned by the directions

of the beam and spectator deflection (spectator plane). Experimental access to the spectator deflection is possible. By applying the transverse segmentation and energy deposition in each of the PSD modules, it may be computed in CBM event-by-event. The PSD is a specialized CBM detector that offers data on spectator deflection in the response plane in that regard. The event plane angle $\Psi_{1,EP}$ is the estimated azimuthal angle of the spectator plane. The difference between the event plane and the response plane orientation arises from the finite number of fragments and the fluctuation of the particle multiplicity from one collision to another at fixed impact parameter orientation. The event plane resolution (a Gaussian width of the $\Psi_{RP} - \Psi_{1,EP}$ distribution) is typically used to quantify this difference.

The event plane angle $\Psi_{1,EP}$ is determined by generating a flow Q-vector, defined in Equation (3.2), from the energy deposited in a particular PSD module or from reconstituted particles in the STS. Here, the energy deposited in a given module i is taken as the weight w_i . Also, the laboratory azimuthal angle ϕ_i can be either the azimuthal angle of the i -th particle reconstructed by the STS or the azimuthal angle of the center in the transverse plane of the i -th PSD module. The event plane angle $\Psi_{1,EP}$ can then be obtained by using Equation (3.3). The PSD Q-vector has off-centered values (mostly in the x direction) due to the dipole magnetic field's distortion of the azimuthal distribution of the particles. The PSD energy distribution's azimuthal imbalance is corrected by applying a Q-vector recentering approach:

$$Q'_{x,y} = \frac{Q_{x,y} - \langle Q_{x,y} \rangle}{\sigma_{Q_{x,y}}}, \quad (4.1)$$

where $\sigma_{Q_{x,y}}$ and $\langle Q_{x,y} \rangle$ are the Gaussian width and the event averaged mean of the $Q_{x,y}$ distribution respectively. The $\langle Q_x \rangle$ dependence on the total energy for a given subevent is shown in Figure 4.7. After applying the recentering process (open symbols), $\langle Q_x \rangle$ (solid symbols) loses its high energy dependence.

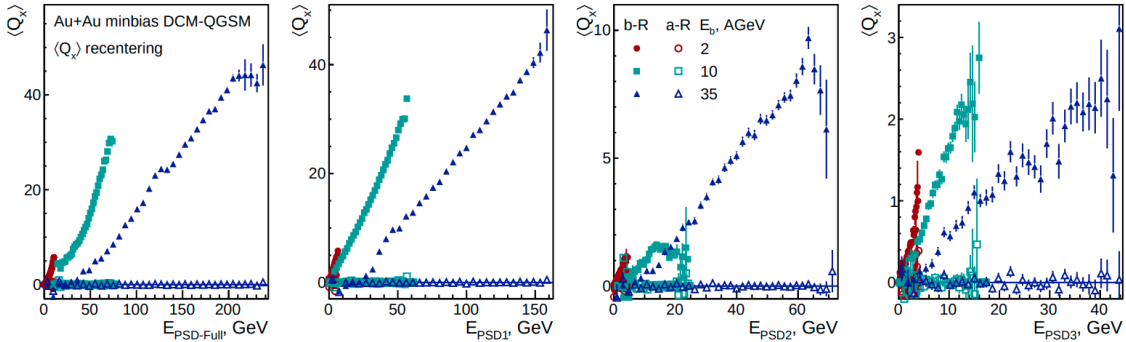


Figure 4.7: Event averaged x component of the Q-vector, $\langle Q_x \rangle$, for different PSD subevents versus the energy of the corresponding PSD subevents before (solid symbols) and after (open symbols) the Q-vector recentering procedure is applied. The panels (from left to right) show results using (a) full PSD information, (b) PSD1, (c) PSD2, and (d) PSD3 subevents. Different colors show results for $E_b = 2, 10,$ and 35 AGeV [70].

For semi-central (20 - 50%) Au+Au collisions at beam energy $E_b = 2, 4, 6, 10, 15, 25,$ and 35 AGeV, the PSD event plane resolution, $\sigma(\Psi_{1,EP} - \Psi_{RP})$, as a function of distance of the PSD from the target in the range between 8 m and 15 m is shown in Figure 4.8 (left). With the exception of the lowest E_b of 2 AGeV, for which the

resolution is 40 - 60 degrees, the PSD event plane resolution ranges between 30 and 40 degrees depending on the proximity to the target and the impact energy. According to the results in Figure 4.8 (left), the ideal PSD placement for SIS100

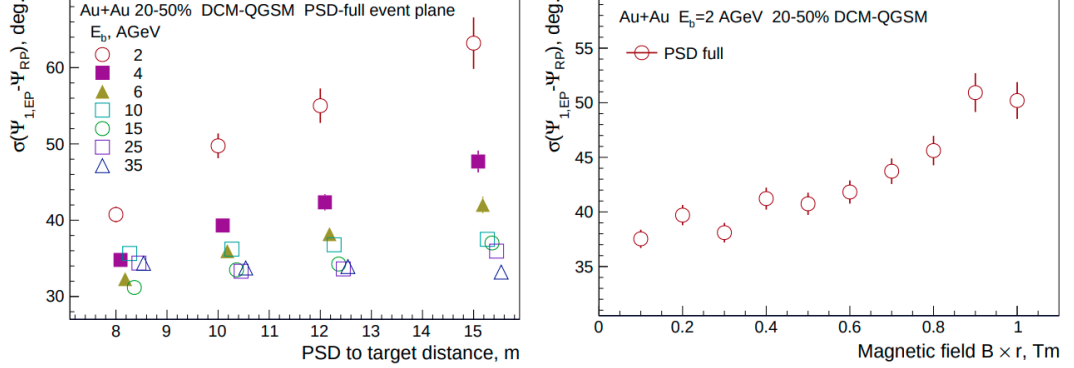


Figure 4.8: First order reaction plane resolution, $\sigma(\Psi_{1,EP} - \Psi_{RP})$, for semi-central (20 - 50%) Au+Au collisions. Left: Results for $E_b = 2, 4, 6, 10, 15, 25,$ and 35 AGeV as a function of the PSD distance from the target in the range between 8 and 15 m. Right: Effect of the magnetic field on the event plane resolution at the $E_b = 2$ AGeV. The PSD is located 8 m from the target [70].

energies ($E_b = 210$ AGeV) is 8 m from the target. The influence of the magnetic field on the event plane resolution at the lowest beam energy $E_b = 2$ AGeV, where distortion is anticipated to be the largest, is shown in Figure 4.8 (right). After using the recentering method, simulations reveal that the resolution has not significantly altered.

For directed flow v_1 , Figure 4.9 shows the PSD performance as a function of collision centrality for (left) the event plane resolution $\sigma(\Psi_{1,EP} - \Psi_{RP})$ and (right) the resolution correction factor, $R_{1,EP} = \langle \cos(\Psi_{1,EP} - \Psi_{RP}) \rangle$. The STS multiplicity is used to estimate the centrality. For mid-central collisions, the event plane resolution is as excellent as 25 - 40 degrees. The weakening of v_1 and the decrease in the fragment multiplicity in the PSD acceptance have a combined effect on the resolution deterioration observed for central and peripheral collisions.

As for the elliptic flow, the proton v_2 in Au+Au collisions at $E_b = 10$ AGeV for $b = 6-8$ fm can be seen in Figure 4.10 using an UrQMD event generator simulation. Calculations based on Monte-Carlo truth information and the findings determined in the data-driven analysis employing PSD subevents for the event plane determination are in good agreement. The limited event plane resolution of the PSD is the cause of the fluctuation in statistical error bars. For a specific sample of Au+Au collisions, the data in Figure 17 may be utilized to project the statistical error bars for a variety of rarely generated particles.

Figure 4.11 shows predictions for relative statistical errors of v_2 for Ω^- (proton and Λ) for a sample of 10^{11} (10^{10}) minimal bias Au+Au collisions at $E_b = 10$ AGeV which is similar to approximately two months of CBM experiment operation at 1 MHz (100 kHz) interaction rate. These findings show that, after a few months of CBM experiment operation at 1 MHz (100 kHz) interaction rate, v_2 of Ω^- (Λ and proton) particles can be detected with a precision of roughly 20 - 40% (0.3 - 1%) in the transverse momentum region between 0.5 - 2 GeV/c.

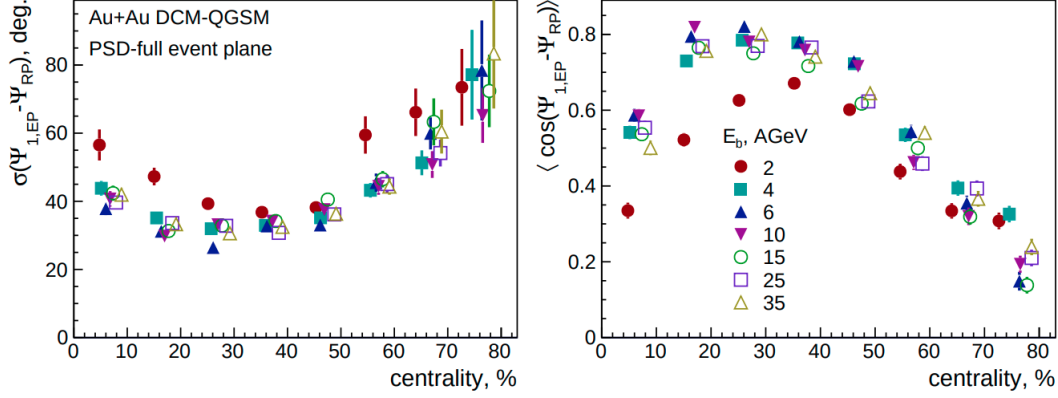


Figure 4.9: First order reaction plane resolution (left), $\sigma(\Psi_{1,EP} - \Psi_{RP})$, and (right) resolution correction factor, $R_{1,EP} = \langle \cos(\Psi_{1,EP} - \Psi_{RP}) \rangle$, plotted as a function of the centrality estimated with the STS detector for Au+Au collisions at $E_b=2, 4, 6, 10, 15, 25,$ and 35 AGeV [70].

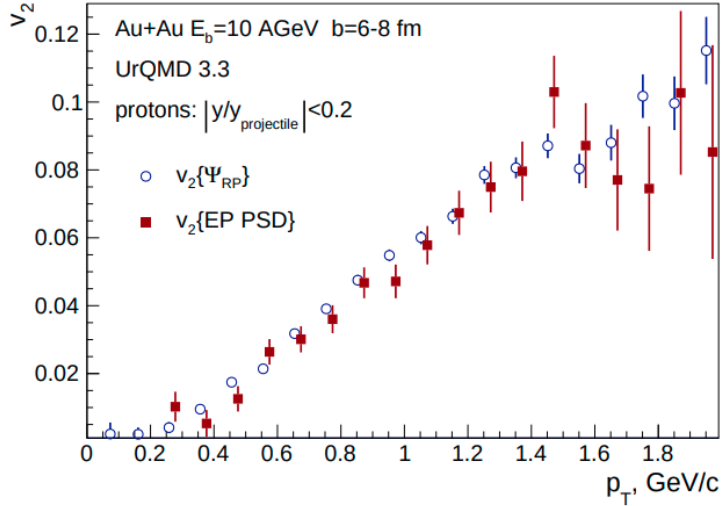


Figure 4.10: Proton v_2 versus p_T reconstructed with the PSD event plane for one million Au+Au collisions generated with the UrQMD model [70].

4.5 Effects of PSD Beamhole

It was found out from simulations that in order to avoid a hard radiation load on the readout electronics in the center of the detector, a larger beam hole must be present. Due to this, a small fraction of forward-moving particle fragments will not be registered by the PSD. This phenomenon is most noticeable for large fragments ($A \geq 4$) and high energies ($E_b = 35$ AGeV) because their rigidity is near to that of the beam ions. Several different geometries of a hole around the beam pipe were considered, out of which a diamond shape of the hole showed to have the most desirable effects. The diamond shape is shown in Figure 4.12.

The resolution of the PSD with the diamond-shaped beam hole is shown in Figure 4.13. The left panel shows the event plane resolution determined by the 3-subevent method. The results for the three PSD modules are depicted. The results show a significant difference between reconstructed and actual values of the resolution

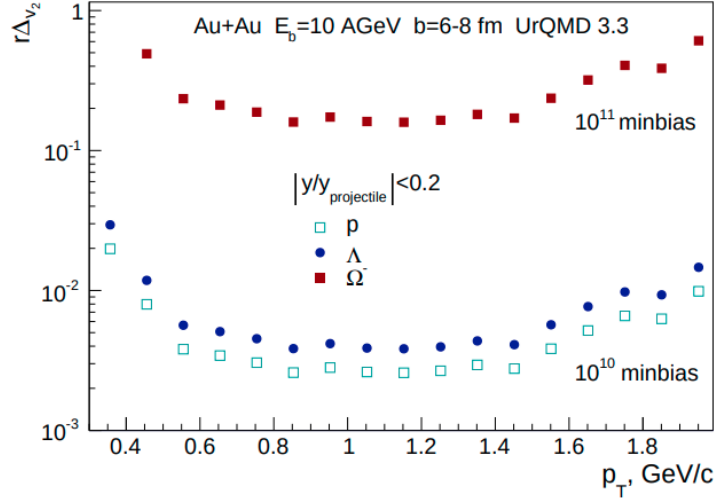


Figure 4.11: Relative statistical errors for v_2 of Ω^- (Λ and proton) in mid-central Au+Au collisions ($b = 6 - 8$ fm) projected for 10^{11} (10^{10}) minimum bias Au+Au collisions [70].

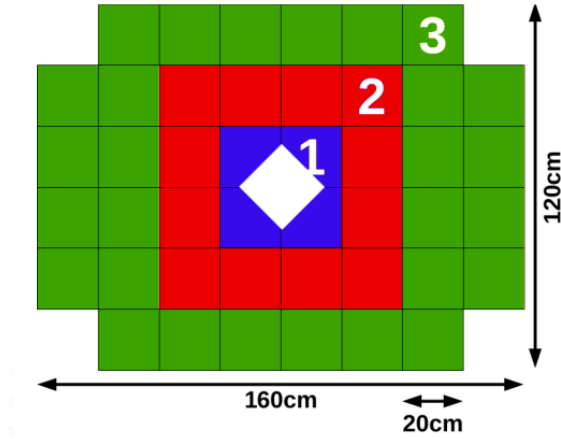


Figure 4.12: The layout of the PSD modules in the plane transverse to the beam direction with the diamond-shaped hole [78].

due to the correlation between the submodules that is caused by their sharing of the same hadronic shower. This effect can be accounted for by a mixed-harmonic method (shown on the right panel) using the positively charged tracks from MVD + STS. This correction yields significant improvement in the obtained resolution values. Most importantly one can see the effect of degradation of the resolution when the central hole is introduced when comparing to Figure 4.9. This is very important for future detector considerations as discussed in next chapters.

4.6 Current situation

As of 2022, due to the Russian aggression in Ukraine and the subsequent cancellation of all collaborations with Russian research institutions, the PSD, along with numerous other technologies, is no longer available for FAIR. However, the findings stated in this chapter can be utilized for the design and construction of a new detector

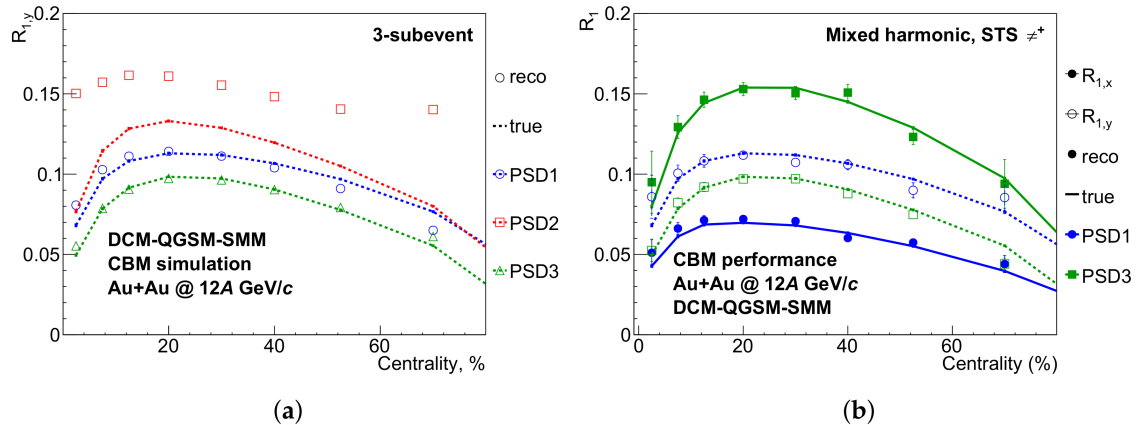


Figure 4.13: Resolution correction factors for PSD with larger central beam hole for subevents calculated with (a) 3-subevent and (b) mixed-harmonic methods. The lines show the true values obtained using the reaction plane angle from the event generator [78].

which will take the PSD's place.

4.7 New Forward Detector for CBM

Similarly to PSD, the goal of the new forward detector is to have a fast data readout and good radiation hardness due to its position close to the beam pipe. It is desirable to use as much knowledge gained from PSD studies as possible. Current propositions consider a scintillator hodoscope (similar to the Forward Wall in HADES) i.e. a layered detector designed to track the paths of charged particles. Some of the proposed specifications of this detector include an increased granularity closer to the beam or using Silicon Photomultipliers (SiPMs) instead of the more expensive MAPMTs for readout. In addition to knowledge from PSD, the technology from the STAR Event Plane Detector (EPD) will be used. EPD allows carrying out both centrality determination and event plane determination reducing systematic uncertainties due to autocorrelations for midrapidity analysis. The measurement of event plane resolution of the EPD at STAR was done for 3, 27 and 54.4 GeV (see Figure 4.14). The resolution is calculated in a similar fashion as in Figure 4.9 showing that at low energies the resolution parameter R_{11} has similar values as for the PSD and at higher energies, we see that the resolution has improved for all centrality classes. Additionally, the resulting event plane measurement is not considerably impacted by the magnetic field of 0.5 T that bends the detected charged particles. Therefore, the EPD only requires recording one hit point for each particle. It should be emphasized, though, that the effective η coverage of the EPD differs noticeably for fixed-target experiments than for collider experiments.

The mechanical design of the new detector has not yet been determined but one of the proposed compositions uses individual replaceable tiles so that the parts damaged by the beam particles (especially close to the beam) can be replaced. The granularity will be determined accordingly based on the simulations but the most likely scenario involves variable tiles size with smaller tiles close to the beam due to the larger particle density. The design around the beam also heavily depends on

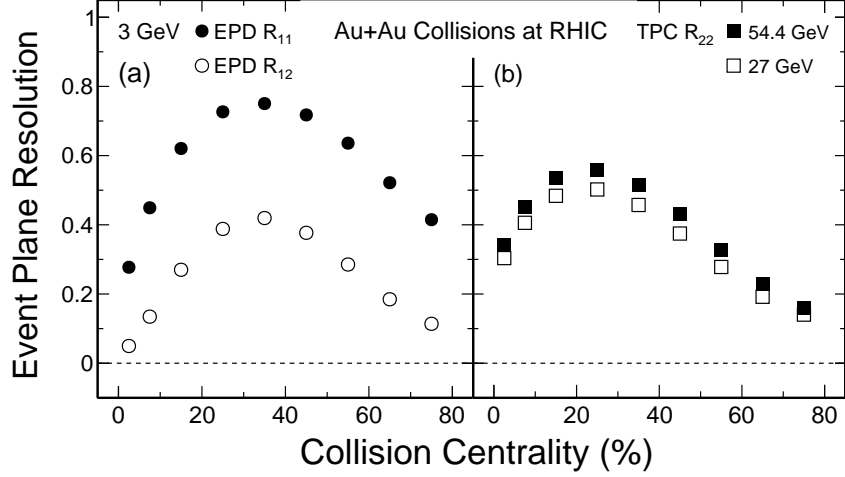


Figure 4.14: Event plane resolution as a function of collision centrality from Au+Au collisions at $\sqrt{s_{NN}} = 3$ (a), 27 and 54.4 GeV (b). In the case of the 3 GeV collisions, Ψ_1 is used to determine the event plane resolutions for the first and second harmonic coefficients shown as R_{11} and R_{12} in the left panel. In the 27 and 54.4 GeV collisions, Ψ_2 is used to evaluate the second-order event plane resolution, see right panel [79].

the ongoing simulations as they will help to understand how close to the beam the tiles can get. The support structure will be reused from PSD as it was constructed to hold the massive detector and therefore should be sufficient.

To determine the physics performance of the new Forward Wall, similarly to PSD, simulations need to be done. These simulations will be done using the HADES geometry. There are several models that can be used such as Geant4 + DCM-QGSM or the Q_n -vector framework [80]. The first simulations have been already performed for the first model, however, the results seemed to be better for PSD. To compare to the PSD performance, there is a plan to use the Q_n -vector framework.

Chapter 5

CBM Beam Pipe Simulations

Within the CBM experiment the Czech Technical University and Nuclear Physics Institute are responsible for design and delivery beam pipe and its positioning mechanism. The beam pipe for the CBM experiment is being designed using simulations with the transport codes FLUKA and GEANT3. One of the design criteria is to minimize secondary particle generation from the interaction of the beam with the beam pipe to a level that is acceptable for the detectors. The multiple scattering in the target dominates the high-intensity beam profile (up to 10^9 Au ions/s). The field of the CBM dipole magnet also deflects the beam. The first part of the beam pipe located inside the STS is divided into two parts: the first is a cylindrical segment with a diameter of 4 cm and a length of about 32 cm; the second is a conical segment with an opening angle of ± 2.8 degrees up to a flange that is about 120 cm downstream of the target. After the flange, a conical beam pipe extends through RICH/MUCH and TRD, and at 370 cm downstream of the target, a bellow is located which allows the succeeding beam pipe to be rotated horizontally by an angle of up to 2 degrees. This angle is adequate to track the beam's deflection for various energy and magnetic fields. The bellow is followed by a 14.25 meter-long pipe that leads the beam particles through the PSD to the beam dump [81].

Figure 5.1 shows the deflection of a gold beam caused by the CBM dipole's magnetic field for beam kinetic energies ranging from 2 to 8 AGeV and a full magnetic field integral of 1 Tm. The iron core of the beam dump is still impacted by the beam with energies of more than 6 AGeV, but not at lower energies. For low Au beam energy, this condition calls for reducing the magnetic field. Even smaller magnetic fields are needed for low-energy beams that have a bigger Z/A ratio than Au, particularly protons. The calculations demonstrate that the PSD location must be modified to account for the beam energy [81] and this also means that the beam pipe must be tilted accordingly. The tilting mechanism design for the downstream beam pipe comprises a metal bellow, carbon fiber composite plates around the bellow for length fixing purposes, and the deflection is achieved by a stepper motor [82]. This whole mechanism together with beam pipe was designed at the Faculty of Mechanical Engineering at the Czech Technical University in Prague.

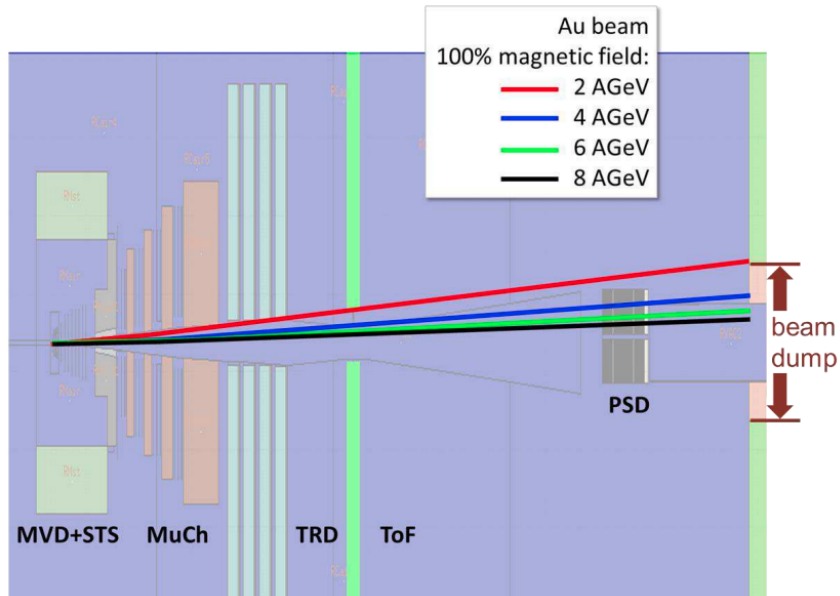


Figure 5.1: Deflection of Au beams with kinetic energies between 2 and 8 AGeV by the magnetic field with an integral of 1 Tm [81].

5.1 Bellow Modeling

As stated above, the tilting mechanism is a crucial component of the CBM beam pipe. This section focuses on the process of transforming the geometries of the tilting mechanism model from an existing design to the GEANT simulation model and the automation of this process for a continuous range of tilting angles. The first step was creating a 3D model of the beam pipe which was done by a team from the Faculty of Mechanical Engineering at the Czech Technical University in Prague. This was done using the mechanical modeling software Autodesk Inventor. Figures 5.2 and 5.3 show the beam pipe model and the tilting assembly with the bellow created in Autodesk Inventor respectively.

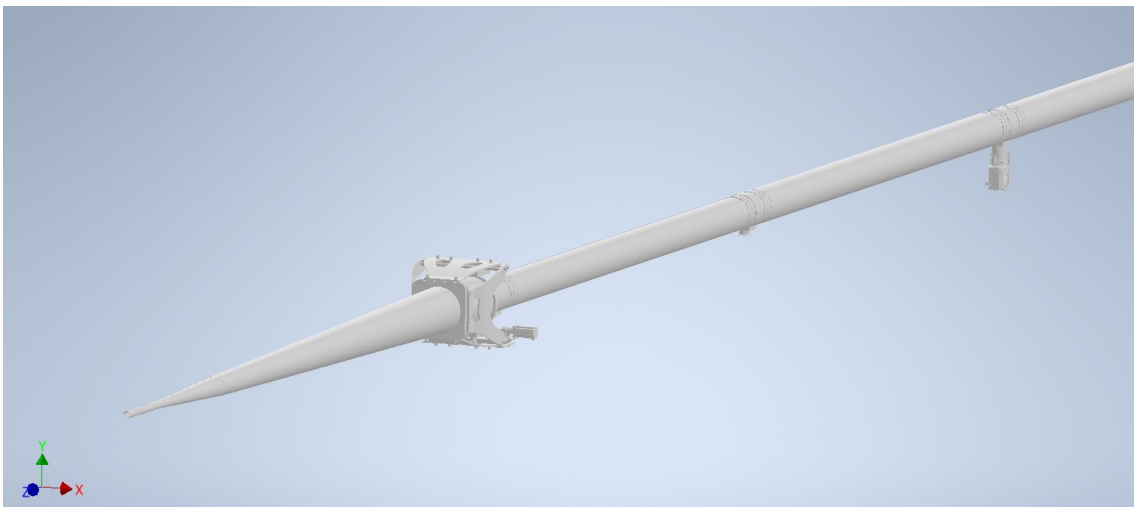


Figure 5.2: CBM beam pipe model made with Autodesk Inventor.

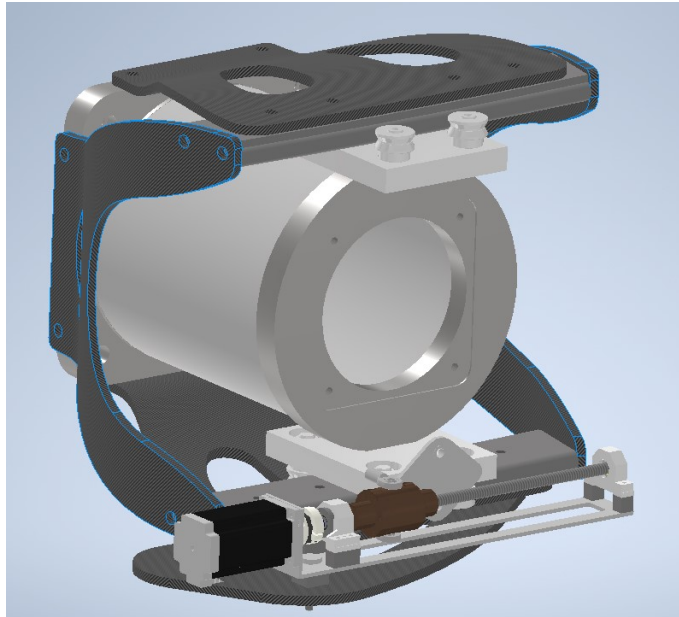


Figure 5.3: Tilting joint assembly model made with Autodesk Inventor.

To allow the movement of the bellow, it was divided into five segments and its parameters were all constrained so that they all adjust to a selected parameter called the driving dimension. This parameter was chosen to be an angle that represents the tilting of a segment at one of the ends of the bellow. Figure 5.4 (left) shows a top view of the bellow with some of the parameters such as the coordinates of the center of each segment, the tilt of each segment or the length of the middle segment. The middle segment is the only one with variable length. In Figure 5.4 (right), a 2D sketch of the bellow is available, in which the segmentation into five segments is shown. Figure 5.8 illustrates the top view of the bellow for different values of the driving angle: 0, 0.7 and 1.5 degrees respectively.

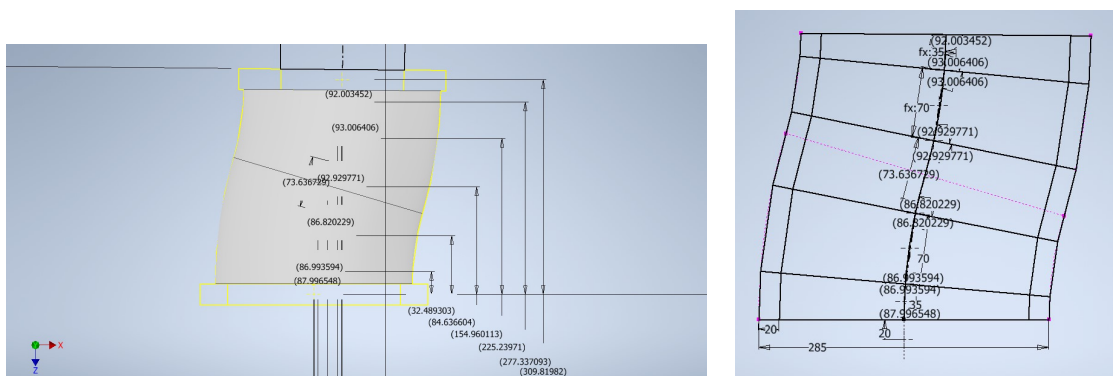


Figure 5.4: Left: Top view of the bellow with model parameters. Right: A 2D sketch of the bellow with the segmentation into five sections.

The next step was finding a continuous range of values for each of the driven parameters as a function of the driving angle in the range of 0 - 1.5 degrees. To achieve this, the parameters were fitted with a fifth-degree polynomial. One of the fit functions for the parameters, specifically, the length of the middle segment (parameter named d145), is shown in Figure 5.5.

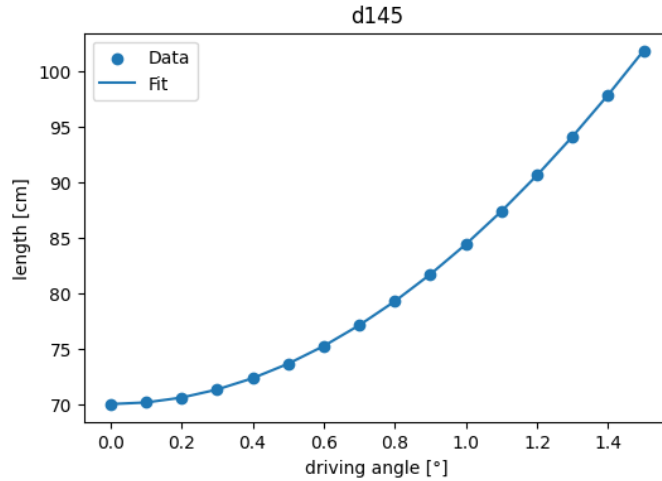


Figure 5.5: The middle segment's length values for different driving angles fitted with a fifth-degree polynomial.

The parameter fit functions were then implemented in a ROOT macro which creates the beam pipe model used in the simulations. This beam pipe model, along with a detailed view of the tilting assembly, is depicted in Figures 5.6 and 5.7. In this model, the fit functions allow continuous tilting of the bellow by changing only the driving angle in the range of 0 - 1.5 degrees. Figure 5.9 shows the ROOT bellow model for 0, 0.7 and 1.5 degrees respectively.

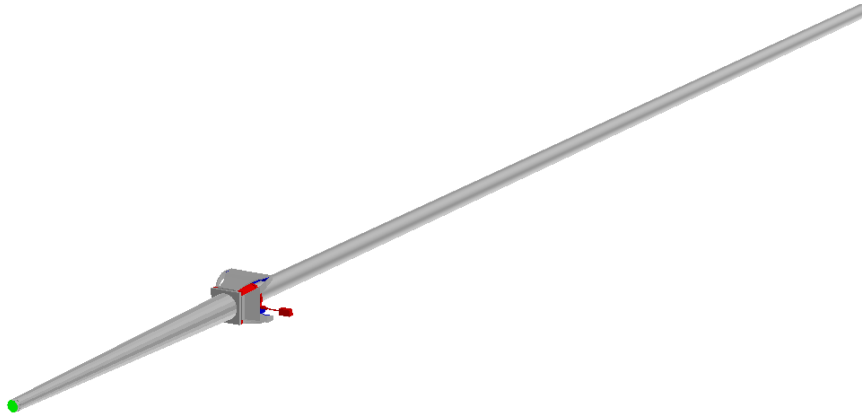


Figure 5.6: The CBM beam pipe model made with ROOT.

In order to determine the effect of the adjustable bellow presence and movement on the PSD performance, a model describing the specific beam pipe has been successfully implemented in the GEANT simulator framework. The simulations have been run with a realistic mass budget. After the collision takes place, further interactions with the beam pipe may occur resulting in the production of secondary particles, thus a realistic mass budget is of crucial importance to studying the performance of PSD. Results from these studies are shown in Figure 5.10. In comparison with the plot on the left, a clear decrease in the number and density of particles in the right

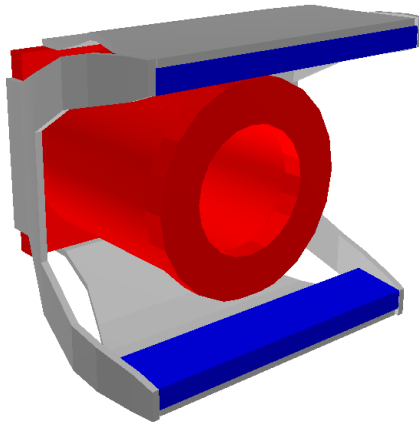


Figure 5.7: Tilting joint assembly model made with ROOT.

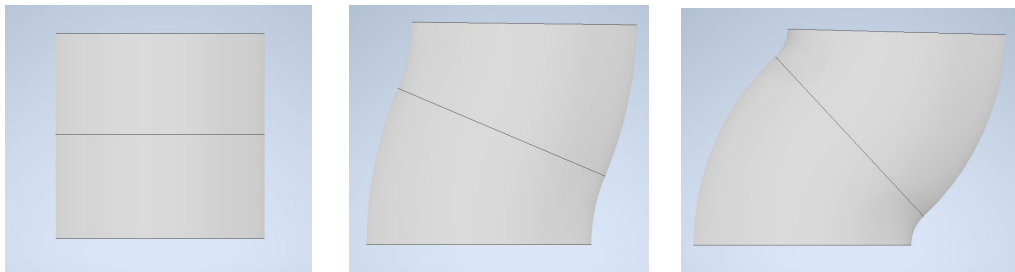


Figure 5.8: Top view of the bellow for 0 degrees (left), 0.7 degrees (center), and 1.5 degrees (right).

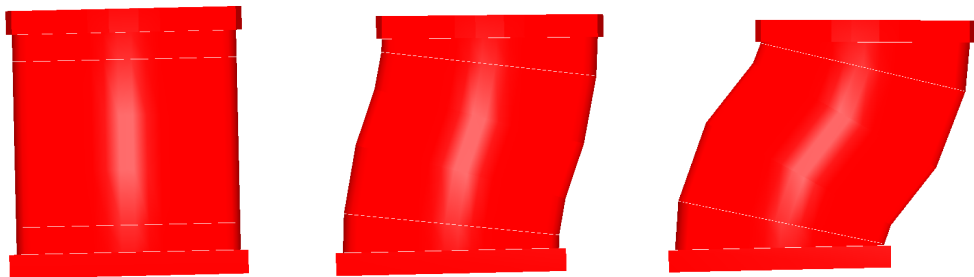


Figure 5.9: Top view of the ROOT bellow model for 0 degrees (left), 0.7 degrees (center), and 1.5 degrees (right).

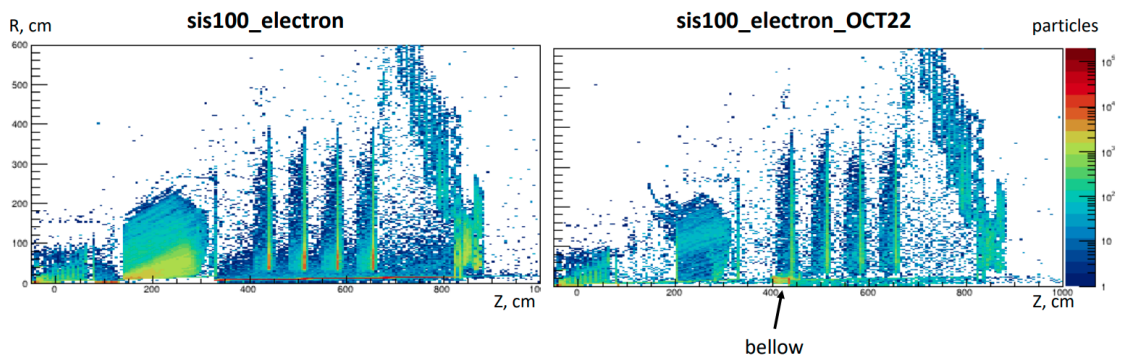


Figure 5.10: The secondary particle generation simulations.

plot is seen demonstrating the importance and effectiveness of the adjustable bellow on background sources affecting the PSD measurement.

Summary

In this thesis, I have learnt and summarized basics of physics of high-energy heavy ion collisions. Study of collective behavior of the system created in such collisions is of great interest since it provides information about important properties, such as equation of state or viscosity, of strongly interacting matter under extreme conditions. The collectivity of created system can be studied by measuring distribution of emitted particles and its azimuthal anisotropy. I have shortly introduced the radial flow and I focused on the anisotropic flow, which is crucial for understanding the evolution of the collision system in non-central collisions.

Furthermore, I described the experiments on the FAIR collider, where I focused on the CBM experiment and the PSD detector together with an outlook on future development. The crucial detector for my work is the Projectile Spectator Detector (PSD) designed to improve the studies of collectivity in nuclear collisions. The simulated PSD performance shows promising results in centrality determination and reaction plane reconstruction for the high-intensity collisions that are to be measured by the CBM. In addition, I introduced a new proposed detector to replace the PSD which will not be delivered because of terminated cooperation with Russian institutions. Work on the performance studies of this new detector will be part of my future work at CBM.

Lastly, I described the specific geometry of the CBM beampipe. This beampipe is unique due to its tilting mechanism that is needed due to the high-intensity beam and deflection of the beam by a CBM dipole magnet. I presented the modeling of the beampipe in GEANT together with the tilting joint assembly and my work on implementing the bellow movement in the simulations. The correct bellow model is crucial for CBM measurements and correct simulations with an appropriate mass budget. This is especially important for the new proposed forward detector. Simulation and analysis of the effects of mass budget of the beampipe and bellow will be another part of my future work.

Bibliography

- [1] “Standard model”. In: *Wikipedia (online)* (Dec. 2022). Accessed: 2022-12-13. URL: https://en.wikipedia.org/wiki/Standard_Model.
- [2] M. Tanabashi et al. “Review of Particle Physics”. In: *Phys. Rev. D* 98 (3 Aug. 2018), p. 030001. DOI: 10.1103/PhysRevD.98.030001. URL: <https://link.aps.org/doi/10.1103/PhysRevD.98.030001>.
- [3] P. M. Watkins. “Discovery of the W and Z boson”. In: *Contemp. Phys.* 27 (1986), pp. 291–324. DOI: 10.1080/00107518608211015.
- [4] Georges Aad et al. “Observation of a new particle in the search for the Standard Model Higgs boson with the ATLAS detector at the LHC”. In: *Phys. Lett. B* 716 (2012), pp. 1–29. DOI: 10.1016/j.physletb.2012.08.020. arXiv: 1207.7214 [hep-ex].
- [5] Robert Craig Group. “Measurement of the Inclusive Jet Cross Section using the Midpoint Algorithm in Run II at CDF”. PhD thesis. Florida U., 2006. DOI: 10.2172/897224.
- [6] Hee Chung, Jungil Lee, and Daekyoung Kang. “Cornell Potential Parameters for S-Wave Heavy Quarkonia”. In: *Journal of The Korean Physical Society* 52 (Mar. 2008). DOI: 10.3938/jkps.52.1151.
- [7] Edward V. Shuryak. “Quantum chromodynamics and the theory of superdense matter”. In: *Physics Reports* 61.2 (1980), pp. 71–158. ISSN: 0370-1573. DOI: 10.1016/0370-1573(80)90105-2.
- [8] Philippe Gros. “Identifying Charged Hadrons on the Relativistic Rise Using the ALICE TPC at LHC”. PhD thesis. Lund U., 2011. URL: <http://cds.cern.ch/record/1362724/files/CERN-THESIS-2011-036.pdf>.
- [9] Carlo Ewerz, Olaf Kaczmarek, and Andreas Samberg. “Free Energy of a Heavy Quark-Antiquark Pair in a Thermal Medium from AdS/CFT”. In: *Journal of High Energy Physics* 2018 (May 2016). DOI: 10.1007/JHEP03(2018)088.
- [10] Tapan K. Nayak. “Quark-Gluon Plasma: Present and Future”. In: *52nd DAE-BRNS Symposium on Nuclear Physics*. Apr. 2008. arXiv: 0804.1368 [nucl-ex].
- [11] Tapan K. Nayak. “Probing the QCD phase structure using event-by-event fluctuations”. In: *J. Phys. Conf. Ser.* 1602.1 (2020). Ed. by Rene Bellwied et al., p. 012003. DOI: 10.1088/1742-6596/1602/1/012003. arXiv: 2008.04643 [nucl-ex].
- [12] Jana Fodorová. “Production of J/ψ meson in central U+U collisions at the STAR experiment”. Master’s Thesis. 2016. URL: http://physics.fjfi.cvut.cz/publications/ejcf/dp_ejcf_16_fodorova.pdf.

- [13] R. Snellings. “Collective Expansion at the LHC: selected ALICE anisotropic flow measurements”. In: *Journal of Physics G: Nuclear and Particle Physics* 41 (Aug. 2014). DOI: 10.1088/0954-3899/41/12/124007.
- [14] Michael Kliemant et al. “Global Properties of Nucleus-Nucleus Collisions”. In: *Lect. Notes Phys.* 785 (2010), pp. 23–103. DOI: 10.1007/978-3-642-02286-9_2. arXiv: 0809.2482 [nucl-ex].
- [15] “Evolution of collisions and QGP”. In: *Particles and Friends (online)* (Oct. 2016). Accessed: 2023-01-04. URL: <https://particlesandfriends.wordpress.com/2016/10/14/evolution-of-collisions-and-qgp/>.
- [16] C.Y. Wong. *Introduction to High-energy Heavy-ion Collisions*. Introduction to High-energy Heavy-ion Collisions. World Scientific, 1994. ISBN: 9789810202637.
- [17] Constantinos A. Loizides. “Jet physics in ALICE”. Master’s thesis. Jan. 2005. arXiv: nucl-ex/0501017.
- [18] P. Braun-Munzinger, I. Heppe, and J. Stachel. “Chemical equilibration in Pb + Pb collisions at the SPS”. In: *Phys. Lett. B* 465 (1999), pp. 15–20. DOI: 10.1016/S0370-2693(99)01076-X. arXiv: nucl-th/9903010.
- [19] A. Andronic et al. “Hadron yields in central nucleus-nucleus collisions, the statistical hadronization model and the QCD phase diagram”. In: *Criticality in QCD and the Hadron Resonance Gas*. Jan. 2021. arXiv: 2101.05747 [nucl-th].
- [20] D. Oliinychenko, K. Bugaev, and Alexander Sorin. “Investigation of Hadron Multiplicities and Hadron Yield Ratios in Heavy Ion Collisions”. In: *Ukrainian Journal of Physics* 58 (Mar. 2012). DOI: 10.15407/ujpe58.03.0211.
- [21] Amaresh Jaiswal and Victor Roy. “Relativistic hydrodynamics in heavy-ion collisions: general aspects and recent developments”. In: *Adv. High Energy Phys.* 2016 (2016), p. 9623034. DOI: 10.1155/2016/9623034. arXiv: 1605.08694 [nucl-th].
- [22] Hermann Wolter et al. “Transport model comparison studies of intermediate-energy heavy-ion collisions”. In: *Prog. Part. Nucl. Phys.* 125 (2022), p. 103962. DOI: 10.1016/j.pnpnp.2022.103962. arXiv: 2202.06672 [nucl-th].
- [23] J. Weil et al. “Particle production and equilibrium properties within a new hadron transport approach for heavy-ion collisions”. In: *Phys. Rev. C* 94.5 (2016), p. 054905. DOI: 10.1103/PhysRevC.94.054905. arXiv: 1606.06642 [nucl-th].
- [24] Lukáš Chlad. “Study of transverse flow of kaons in Au+Au collisions at 1.23A GeV”. PhD thesis. 2021. URL: <https://dspace.cuni.cz/handle/20.500.11956/170699>.
- [25] K. Aamodt et al. “Suppression of Charged Particle Production at Large Transverse Momentum in Central Pb-Pb Collisions at $\sqrt{s_{NN}} = 2.76$ TeV”. In: *Phys. Lett. B* 696 (2011), pp. 30–39. DOI: 10.1016/j.physletb.2010.12.020. arXiv: 1012.1004 [nucl-ex].
- [26] Francesco Noferini. “ALICE Highlights”. In: *MDPI Proc.* 13.1 (2019), p. 6. DOI: 10.3390/proceedings2019013006. arXiv: 1906.02460 [hep-ex].

- [27] L. Adamczyk et al. “Dielectron Mass Spectra from Au+Au Collisions at $\sqrt{s_{NN}} = 200$ GeV”. In: *Phys. Rev. Lett.* 113.2 (2014). [Addendum: *Phys.Rev.Lett.* 113, 049903 (2014)], p. 022301. DOI: 10.1103/PhysRevLett.113.022301. arXiv: 1312.7397 [hep-ex].
- [28] Johann Rafelski and R. Hagedorn. “From Hadron Gas to Quark Matter. 2.” In: *Ref.TH.2969-CERN* (Oct. 1980). URL: <https://inspirehep.net/files/539e4a3ffcf09dbc6deca5b1f924f656>.
- [29] Betty Bezverkhny Abelev et al. “Multi-strange baryon production at mid-rapidity in Pb-Pb collisions at $\sqrt{s_{NN}} = 2.76$ TeV”. In: *Phys. Lett. B* 728 (2014). [Erratum: *Phys.Lett.B* 734, 409–410 (2014)], pp. 216–227. DOI: 10.1016/j.physletb.2014.05.052. arXiv: 1307.5543 [nucl-ex].
- [30] Astrid Morreale. “Production of π^0 , K^\pm and η mesons in Pb-Pb and pp collisions at $\sqrt{s_{NN}} = 2.76$ TeV measured with the ALICE detector at the LHC”. In: *J. Phys. Conf. Ser.* 779.1 (2017). Ed. by Huan Zhong Huang et al., p. 012051. DOI: 10.1088/1742-6596/779/1/012051. arXiv: 1609.06106 [hep-ex].
- [31] Ekkard Schnedermann, Josef Sollfrank, and Ulrich W. Heinz. “Thermal phenomenology of hadrons from 200-A/GeV S+S collisions”. In: *Phys. Rev. C* 48 (1993), pp. 2462–2475. DOI: 10.1103/PhysRevC.48.2462. arXiv: nucl-th/9307020.
- [32] Vardan Khachatryan et al. “Multiplicity and rapidity dependence of strange hadron production in pp, pPb, and PbPb collisions at the LHC”. In: *Phys. Lett. B* 768 (2017), pp. 103–129. DOI: 10.1016/j.physletb.2017.01.075. arXiv: 1605.06699 [nucl-ex].
- [33] Peter F. Kolb and Ulrich W. Heinz. “Hydrodynamic description of ultrarelativistic heavy ion collisions”. In: (May 2003). Ed. by Rudolph C. Hwa and Xin-Nian Wang, pp. 634–714. arXiv: nucl-th/0305084.
- [34] Sergei A. Voloshin, Arthur M. Poskanzer, and Raimond Snellings. *Collective phenomena in non-central nuclear collisions*. 2008. DOI: 10.48550/ARXIV.0809.2949. URL: <https://arxiv.org/abs/0809.2949>.
- [35] Karel Šafařík. “Physics of Ultra-relativistic Nuclear Collisions”. In: *FNSPE lectures* (2022).
- [36] Jean-Yves Ollitrault. “Anisotropy as a signature of transverse collective flow”. In: *Phys. Rev. D* 46 (1 July 1992), pp. 229–245. DOI: 10.1103/PhysRevD.46.229.
- [37] A. M. Poskanzer et al. “Directed and elliptic flow in 158-GeV/nucleon Pb + Pb collisions”. In: *Nucl. Phys. A* 638 (1998). Ed. by T. Hatsuda et al., pp. 463–466. DOI: 10.1016/S0375-9474(98)00379-0.
- [38] P.F Kolb et al. “Elliptic flow at SPS and RHIC: from kinetic transport to hydrodynamics”. In: *Physics Letters B* 500.3 (2001), pp. 232–240. ISSN: 0370-2693. DOI: 10.1016/S0370-2693(01)00079-X.
- [39] K Aamodt et al. “Elliptic flow of charged particles in Pb-Pb collisions at 2.76 TeV”. In: *Phys. Rev. Lett.* 105 (2010), p. 252302. DOI: 10.1103/PhysRevLett.105.252302. arXiv: 1011.3914 [nucl-ex].

- [40] C. Adler et al. “Elliptic flow from two and four particle correlations in Au+Au collisions at $\sqrt{s_{NN}} = 130$ GeV”. In: *Phys. Rev. C* 66 (2002), p. 034904. DOI: 10.1103/PhysRevC.66.034904. arXiv: nucl-ex/0206001.
- [41] Grazyna Odyniec. “RHIC Beam Energy Scan Program: Phase I and II”. In: *PoS CPOD2013* (2013), p. 043. DOI: 10.22323/1.185.0043.
- [42] M. S. Abdallah et al. “Disappearance of partonic collectivity in $\sqrt{s_{NN}}=3$ GeV Au+Au collisions at RHIC”. In: *Phys. Lett. B* 827 (2022), p. 137003. DOI: 10.1016/j.physletb.2022.137003. arXiv: 2108.00908 [nucl-ex].
- [43] Fabrizio Grosa. “Study of R_{AA} and v_2 of non-strange D mesons and D-jet production in Pb-Pb collisions with ALICE”. In: (2019). DOI: 10.48550/ARXIV.1909.06562. URL: <https://arxiv.org/abs/1909.06562>.
- [44] Jaroslav Adam et al. “Anisotropic flow of charged particles in Pb-Pb collisions at $\sqrt{s_{NN}} = 5.02$ TeV”. In: *Phys. Rev. Lett.* 116.13 (2016), p. 132302. DOI: 10.1103/PhysRevLett.116.132302. arXiv: 1602.01119 [nucl-ex].
- [45] Serguei Chatrchyan et al. “Studies of Azimuthal Dihadron Correlations in Ultra-Central PbPb Collisions at $\sqrt{s_{NN}} = 2.76$ TeV”. In: *JHEP* 02 (2014), p. 088. DOI: 10.1007/JHEP02(2014)088. arXiv: 1312.1845 [nucl-ex].
- [46] Paul M. Chesler. “How big are the smallest drops of quark-gluon plasma?” In: *JHEP* 03 (2016), p. 146. DOI: 10.1007/JHEP03(2016)146. arXiv: 1601.01583 [hep-th].
- [47] A. Adare et al. “Quadrupole Anisotropy in Dihadron Azimuthal Correlations in Central d +Au Collisions at $\sqrt{s_{NN}}=200$ GeV”. In: *Phys. Rev. Lett.* 111 (21 Nov. 2013), p. 212301. DOI: 10.1103/PhysRevLett.111.212301. URL: <https://link.aps.org/doi/10.1103/PhysRevLett.111.212301>.
- [48] C. Aidala et al. “Measurements of Multiparticle Correlations in $d + Au$ Collisions at 200, 62.4, 39, and 19.6 GeV and $p + Au$ Collisions at 200 GeV and Implications for Collective Behavior”. In: *Phys. Rev. Lett.* 120.6 (2018), p. 062302. DOI: 10.1103/PhysRevLett.120.062302. arXiv: 1707.06108 [nucl-ex].
- [49] Jaroslav Adam et al. “Azimuthal Harmonics in Small and Large Collision Systems at RHIC Top Energies”. In: *Phys. Rev. Lett.* 122.17 (2019), p. 172301. DOI: 10.1103/PhysRevLett.122.172301. arXiv: 1901.08155 [nucl-ex].
- [50] A. Adare et al. “Measurements of mass-dependent azimuthal anisotropy in central p +Au, d +Au, and ^3He +Au collisions at $\sqrt{s_{NN}} = 200$ GeV”. In: *Phys. Rev. C* 97 (2018), p. 064904. DOI: 10.1103/PhysRevC.97.064904. arXiv: 1710.09736 [nucl-ex].
- [51] C. Aidala et al. “Creation of quark–gluon plasma droplets with three distinct geometries”. In: *Nature Phys.* 15.3 (2019), pp. 214–220. DOI: 10.1038/s41567-018-0360-0. arXiv: 1805.02973 [nucl-ex].
- [52] Serguei Chatrchyan et al. “Multiplicity and Transverse Momentum Dependence of Two- and Four-Particle Correlations in pPb and PbPb Collisions”. In: *Phys. Lett. B* 724 (2013), pp. 213–240. DOI: 10.1016/j.physletb.2013.06.028. arXiv: 1305.0609 [nucl-ex].

- [53] Betty Bezverkhny Abelev et al. “Long-range angular correlations of π , K and p in p-Pb collisions at $\sqrt{s_{NN}} = 5.02$ TeV”. In: *Phys. Lett. B* 726 (2013), pp. 164–177. DOI: 10.1016/j.physletb.2013.08.024. arXiv: 1307.3237 [nucl-ex].
- [54] Vardan Khachatryan et al. “Long-range two-particle correlations of strange hadrons with charged particles in pPb and PbPb collisions at LHC energies”. In: *Phys. Lett. B* 742 (2015), pp. 200–224. DOI: 10.1016/j.physletb.2015.01.034. arXiv: 1409.3392 [nucl-ex].
- [55] Morad Aaboud et al. “Measurement of long-range multiparticle azimuthal correlations with the subevent cumulant method in pp and $p + Pb$ collisions with the ATLAS detector at the CERN Large Hadron Collider”. In: *Phys. Rev. C* 97.2 (2018), p. 024904. DOI: 10.1103/PhysRevC.97.024904. arXiv: 1708.03559 [hep-ex].
- [56] Shreyasi Acharya et al. “Investigations of Anisotropic Flow Using Multiparticle Azimuthal Correlations in pp, p-Pb, Xe-Xe, and Pb-Pb Collisions at the LHC”. In: *Phys. Rev. Lett.* 123.14 (2019), p. 142301. DOI: 10.1103/PhysRevLett.123.142301. arXiv: 1903.01790 [nucl-ex].
- [57] Albert M Sirunyan et al. “Multiparticle correlation studies in pPb collisions at $\sqrt{s_{NN}} = 8.16$ TeV”. In: *Phys. Rev. C* 101.1 (2020), p. 014912. DOI: 10.1103/PhysRevC.101.014912. arXiv: 1904.11519 [hep-ex].
- [58] Katarína Gajdošová Křížková. “Collectivity in small and large collision systems at the LHC with ALICE”. In: *J. Phys. Conf. Ser.* 1271.1 (2019), p. 012002. DOI: 10.1088/1742-6596/1271/1/012002.
- [59] A. Adare et al. “Multiparticle azimuthal correlations for extracting event-by-event elliptic and triangular flow in Au + Au collisions at $\sqrt{s_{NN}} = 200$ GeV”. In: *Phys. Rev. C* 99 (2 Feb. 2019), p. 024903. DOI: 10.1103/PhysRevC.99.024903.
- [60] Arthur M. Poskanzer and S. A. Voloshin. “Methods for analyzing anisotropic flow in relativistic nuclear collisions”. In: *Phys. Rev. C* 58 (1998), pp. 1671–1678. DOI: 10.1103/PhysRevC.58.1671. arXiv: nucl-ex/9805001.
- [61] N. Borghini, P. M. Dinh, and J. Y. Ollitrault. “Analysis of directed flow from elliptic flow”. In: *Phys. Rev. C* 66 (2002), p. 014905. DOI: 10.1103/PhysRevC.66.014905. arXiv: nucl-th/0204017.
- [62] J. Adams et al. “Azimuthal anisotropy at RHIC: The First and fourth harmonics”. In: *Phys. Rev. Lett.* 92 (2004). [Erratum: Phys.Rev.Lett. 127, 069901 (2021)], p. 062301. DOI: 10.1103/PhysRevLett.127.069901. arXiv: nucl-ex/0310029.
- [63] B. I. Abelev et al. “Centrality dependence of charged hadron and strange hadron elliptic flow from $\sqrt{s_{NN}} = 200$ GeV Au + Au collisions”. In: *Phys. Rev. C* 77 (2008), p. 054901. DOI: 10.1103/PhysRevC.77.054901. arXiv: 0801.3466 [nucl-ex].
- [64] Sergei A. Voloshin. “Toward the energy and the system size dependence of elliptic flow: Working on flow fluctuations”. In: (June 2006). arXiv: nucl-th/0606022.

- [65] FAIR. *FAIR - The Universe In The Laboratory*. Brochure. Accessed: 2022-11-16. July 2020. URL: https://www.gsi.de/fileadmin/oeffentlichkeitsarbeit/Broschueren/e-FAIR_Broschuere_20200702_web.pdf.
- [66] Nasser Kalantar-Nayestanaki and Alison Bruce. “NUSTAR: Nuclear Structure Astrophysics and Reactions at FAIR”. In: *Nuclear Physics News* 28.3 (2018), pp. 5–11. DOI: 10.1080/10619127.2018.1495476.
- [67] A. Belias. “FAIR status and the PANDA experiment”. In: *Journal of Instrumentation* 15.10 (Oct. 2020), p. C10001. DOI: 10.1088/1748-0221/15/10/C10001.
- [68] Th. Stöhlker et al. “APPA at FAIR: From fundamental to applied research”. In: *Nuclear Instruments and Methods in Physics Research Section B: Beam Interactions with Materials and Atoms* 365 (2015). Swift Heavy Ions in Matter, 18 – 21 May, 2015, Darmstadt, Germany, pp. 680–685. ISSN: 0168-583X. DOI: <https://doi.org/10.1016/j.nimb.2015.07.077>.
- [69] T. Ablyazimov et al. “Challenges in QCD matter physics –The scientific programme of the Compressed Baryonic Matter experiment at FAIR”. In: *Eur. Phys. J. A* 53.3 (2017), p. 60. DOI: 10.1140/epja/i2017-12248-y. arXiv: 1607.01487 [nucl-ex].
- [70] Fedor Guber and Ilya Selyuzhenkov, eds. *Technical Design Report for the CBM Projectile Spectator Detector (PSD)*. Darmstadt: GSI, 2015, 75 S. URL: <https://repository.gsi.de/record/109059>.
- [71] J. Stroth and M. Deveau. *Technical Design Report for the CBM: Micro Vertex Detector (MVD)*. Tech. rep. 1. 2022, 157 p. URL: <https://repository.gsi.de/record/246516>.
- [72] Johann Heuser et al., eds. [*GSI Report 2013-4*] *Technical Design Report for the CBM Silicon Tracking System (STS)*. Darmstadt: GSI, 2013, 167 p. URL: <https://repository.gsi.de/record/54798>.
- [73] *Technical Design Report for the CBM Ring Imaging Cherenkov Detector*. Tech. rep. 2013, 215 p. URL: <https://repository.gsi.de/record/65526>.
- [74] Subhasis Chattopadhyay et al., eds. *Technical Design Report for the CBM : Muon Chambers (MuCh)*. Darmstadt: GSI, 2015, 190 S. URL: <https://repository.gsi.de/record/161297>.
- [75] *The Transition Radiation Detector of the CBM Experiment at FAIR : Technical Design Report for the CBM Transition Radiation Detector (TRD)*. Tech. rep. FAIR Technical Design Report. Darmstadt, 2018, 165 p. DOI: 10.15120/GSI-2018-01091. URL: <https://repository.gsi.de/record/217478>.
- [76] Norbert Herrmann, ed. *Technical Design Report for the CBM Time-of-Flight System (TOF)*. Darmstadt: GSI, 2014, 182 S. URL: <https://repository.gsi.de/record/109024>.
- [77] Klochkov and I Selyuzhenkov. “Centrality determination in heavy-ion collisions with the CBM experiment”. In: *Journal of Physics: Conference Series* 798 (Jan. 2017), p. 012059. DOI: 10.1088/1742-6596/798/1/012059.
- [78] Oleg Golosov, Ilya Selyuzhenkov, and Evgeny Kashirin. “Data-Driven Methods for Spectator Symmetry Plane Estimation in CBM Experiment at FAIR”. In: *Particles* 4.3 (2021), pp. 354–360. DOI: 10.3390/particles4030030.

- [79] M. S. Abdallah et al. “Disappearance of partonic collectivity in sNN=3GeV Au+Au collisions at RHIC”. In: *Phys. Lett. B* 827 (2022), p. 137003. DOI: 10.1016/j.physletb.2022.137003. arXiv: 2108.00908 [nucl-ex].
- [80] Ilya Selyuzhenkov and Sergei Voloshin. “Effects of non-uniform acceptance in anisotropic flow measurement”. In: *Phys. Rev. C* 77 (2008), p. 034904. DOI: 10.1103/PhysRevC.77.034904. arXiv: 0707.4672 [nucl-th].
- [81] *CBM Progress Report 2018*. Tech. rep. CBM Progress Report 2018. Darmstadt, 2019, 220 p. DOI: 10.15120/GSI-2019-01018. URL: <https://repository.gsi.de/record/220128>.
- [82] Peter Senger and Volker Friese. *CBM Progress Report 2021*. Tech. rep. 2022. Darmstadt, 2022, 239 p. DOI: 10.15120/GSI-2022-00599. URL: <https://repository.gsi.de/record/246663>.